Contributions of Lattice Anharmonicity to Optoelectronic Properties of Lead Halide Perovskites

Prakriti Pradhan Joshi

Submitted in partial fulfillment of the
requirements for the degree of
Doctor of Philosophy
under the Executive Committee
of the Graduate School of Arts and Sciences

COLUMBIA UNIVERSITY

2019

ABSTRACT

Contributions of Lattice Anharmonicity to Optoelectronic Properties of Lead Halide Perovskites

Prakriti Pradhan Joshi

Lead halide perovskites (LHPs) have forcefully emerged as a promising materials class for next-generation solar cells. The high efficiencies of LHP-based photovoltaics are underpinned by their outstanding optoelectronic properties, including long carrier lifetimes, long carrier diffusion lengths, high radiative efficiencies, and long-lived hot carriers. In conventional semiconductors, high efficiencies are achieved by stringent control over defect densities; higher purity diminishes the number of carrier scattering events and yields better optoelectronic properties. Given the high defect densities of LHPs, these observed behaviors indicate that LHPs are defect-tolerant and disobey this paradigm via dynamic screening of charge carriers.

In order to expand the library of defect-tolerant semiconductors, we must elucidate the carrier-lattice interactions that lead to dynamic screening. LHP lattices are highly anharmonic and dynamically disordered, which must play a role in this screening mechanism. This anharmonicity demands a departure from the conventional Fröhlich interaction, which considers the harmonic coupling of a carrier to one phonon, to a picture that incorporates anharmonic phonon-phonon couplings. The objective of this thesis is to investigate the ultrafast anharmonic lattice response associated with dynamic screening of charge carriers. We probe the formation of large polarons in $CH_3NH_3PbBr_3$ and $CsPbBr_3$ using time-resolved

optical Kerr effect spectroscopy. We further investigate the coupling of phonon modes in a model system, $CsPbBr_3$, in the presence of charge carriers using ultrafast coherent phonon spectroscopy.

Contents

List of Figures iv

Acknowledgments xvi

1 Motivation 1

1.1 Overview 1

1.2 Thesis Structure 2

2 Material Properties of Lead Halide Perovskites 6

Abstract 6

2.1 Lattice and Electronic Structure 7

2.2 Dynamic Disorder of A-Site Cations 9

2.3 Disorder-Induced Polar Nano Domains in the Lead Halide Lattice 12

2.4 Frequency-Dependent Dielectric Screening 16

2.5 Large Polarons in Lead Halide Perovskites 19

2.6 Lead Halide Sublattice Contributions to the Large Polaron 24

2.7 Ferroelectric Large Polaron Hypothesis 25

3 Optical Methods 28

Abstract 28

3.1 Regenerative Amplifier System 29

3.2 Non-Collinear Optical Parametric Amplification (NOPA) 30

3.3 Time-Resolved Optical Kerr Effect Spectroscopy and Optical Heterodyne Detection 32

3.4 Shot-to-Shot Balanced Detection 34

3.5 Fourier Transform Coherent Phonon Spectroscopy 36

4 Large Polaron Formation 39

Abstract 39

4.1 Introduction 40

4.2 Materials and Methods 41

4.3 Results and Discussion 41

4.4 Conclusions 56

4.5 Appendix: Supplementary Materials 57

4.5.1 Synthesis and structural characterizations of LHP macro-crystals 57

4.5.2 Time-resolved optical Kerr effect measurements 58

4.5.3 Time resolved reflectance measurements 59

4.5.4 Theoretical calculations 60

4.5.5 Kramers-Kronig Analysis 62

4.5.6 Estimation of Fröhlich couplings and mobilties 63

4.5.7 Supplementary Figures 65

4.5.8 Supplementary Tables 76

5 Coherent Phonon Transfer and Softening 77

Abstract 77

5.1 Introduction 78

5.2 Results and Discussion 80

5.3 Conclusions 87

5.4 Appendix: Supplementary Materials 88

5.4.1 Experimental Setup 88

5.4.2 Time-Frequency analysis 89

5.4.3 Coupled Oscillator Model 89

5.4.4 Figures and Extended Data 93

6 Ferroelectric Charge Localization 98

Abstract 98

6.1 Introduction 99

6.2 Results and Discussion 101

6.3 Conclusions 109

6.4 Appendix: Supplementary Materials 110

6.4.1 Model Potential 110

6.4.2 Displacive excitation of coherent phonons in model potential 112

6.4.3 Extended data figures 115

7 Concluding Remarks 122

References 124

Appendix: Single Crystal Synthesis and Characterization 144

List of Figures

Figure 2.1 Cubic Lead Halide Perovskite (LHP) structure. The A-site cations (magenta) are interspersed between a sublattice of PbX_6^{4-} corner-shared octahedrals. Pb^{2+} is shown in dark blue, X^- is shown in orange, and the octahedral is shaded in light blue.....7

Figure 2.2 Structural phases and electronic band structure of MAPbI3. Crystal structures of A orthorhombic phase, **B** tetragonal phase, and **C c**ubic phase MAPbI3. The 100 and 001 orientations are shown in the upper and lower panels, respectively. Reproduced with permission from ref. [37]. Copyright 2015 by the American Physical Society. **D** The electronic band structure of MAPbI3 as calculated by SOC-GW reveals a direct band gap at the Γ point. Reproduced with permission from ref. [41]. Copyright 2014 Springer Nature. 8

Figure 2.3 Fluctuations of MA+ orientation as a function of temperature. A The a and b axes of orthorhombic-phase $MAPbI_3$. **B** The azimuthal angle ϕ is defined as the angle of rotation in the a-b plane. **C** The polar angle θ is defined as the angle of the C-N bond with respect to the c-axis. **D** The distribution of angular orientations of the C-N bond as a function of temperature. Reprinted with permission from Ref. [64]. Copyright 2015 American Chemical Society.. 10

Figure 2.4 Low-frequency Raman spectra of MAPbBr3 (A) and CsPbBr3 (B). The orthorhombic, tetragonal, and cubic phases are indicated by blue, green, and red, respectively. In the orthorhombic phase, the phonon modes are sharp and well-resolved. At higher-temperature phases, the structure becomes more diffuse and a clear central peak emerges, suggesting dynamic disorder from the lead bromide sublattice. Reprinted with permission from ref. [66]. Copyright 2017 by the American Physical Society..... 12

Figure 2.5 Anharmonic double-well potential and corresponding phonon modes. A An anharmonic double-well potential (green) of $MAPbI_3$ representing the reorientations of I^- (purple) around its equilibrium position on the Pb^{2+}-Pb^{2+} axis (gray). The offset is described by the electric dipole P and the change in wavevector, **q**, which is the quantity $\mathbf{k_f} - \mathbf{k_i}$. Reprinted with permission from Katan et al: Springer Nature Materials, ref. [93], copyright 2018. **B** Polar phonon mode at the Γ point in cubic and orthorhombic $CsPbI_3$ induced by the antiparallel displacements of Cs^+ and I^-. This mode also has an anharmonic double well potential. Reprinted with permission from ref. [91]. Copyright 2017 American Chemical Society..... 14

Figure 2.6 Frequency-dependent dielectric functions. A The real part of ε, $Re(\varepsilon)$ and **B** the imaginary part of ε, $Im(\varepsilon)$ for $MAPbI_3$ (red), GaAs (green), and H_2O (blue). Adapted with permission, ref. [104], published by The Royal Society of Chemistry; ref. [105], Copyright 2017 Wiley; ref. [106], Copyright 1975 Univ. of Missouri – Kansas City; ref. [107], Copyright 1998 Academic Press. 16

Figure 2.7 Dielectric Function of $SrBi_2Ta_2O_9$ (SBT). $Re(\varepsilon)$ and $Im(\varepsilon)$ are shown in red and blue respectively. Adapted from ref. [111], with the permission of AIP publishing. 19

Figure 2.8 Spatial localization of the conduction band and valence band edges of $MAPbI_3$. Reprinted with permission from ref. [115], published by the Royal Society of Chemistry. 21

Figure 2.9 Time-resolved two photon photoemission (TR-2PPE) of polycrystalline $MAPbI_3$ thin films. Charge carriers are excited and then photoionized with variable time delay. The charge carriers relax in ~300 fs to two distinct populations, E^o and E^*, which are band-edge carriers and hot carriers, respectively. E^* has a lifetime of ~100 ps. Reprinted with permission from ref. [21]. Copyright 2016 American Chemical Society. 23

Figure 2.10 Fröhlich Large Polaron versus Ferroelectric Large Polaron. A, C, E, Harmonic potential, polarization response to electric field, and dipole moment in a Fröhlich large polaron. **B, D, F,** Anharmonic double well potential, polarization response to electric field, and dipole moment in ferroelectric large polaron. Reprinted with permission from ref. [77], Copyright 2019 Wiley; ref. [34], Copyright 2018 Springer Nature[34]. 27

Figure 3.1 Schematic of a visible-range non-collinear optical parametric amplifier (NOPA). A white light seed is generated by focusing an 800 nm fundamental into an Al_2O_3 window. A 400 nm pump pulse is generated by doubling the fundamental with BBO. The pump and seed pulses are temporally and spatially overlapped on an appropriately cut BBO crystal that is oriented to satisfy the phase-matching conditions. The output is then directed into a prism compressor, yielding sub-30 fs pulses. 31

Figure 3.2 TR-OKE schematic. A linearly polarized pump pulse (green) induces a transient birefringence in the LHP sample. The transient birefringence is probed with a linearly pump probe pulse (red) with time delay Δt. The probe is cross-polarized after the sample, and the cross-polarization is slightly detuned

to generate a local oscillator that coherently mixes with the Kerr signal. The resulting heterodyne is detected by a home-built spectrometer..... 32

Figure 3.3 Shot-to-shot balanced detection. The sample is excited with a linearly polarized visible pump pulse (green) and probed with a linearly polarized near-IR probe pulse (red). The transmitted probe is passed through a waveplate and a Wollaston prism, which splits the probe into two components of perpendicular polarizations. A half- or quarter- waveplate tunes the linear polarization or ellipticity of the probe pulse prior to the Wollaston prism, allowing the probe polarization components to be "balanced" on Si-based photodiodes (PD1 and PD2). The difference between these two signals (I_1-I_2) is digitized and acquired at 10 kHz..... 34

Figure 3.4 Pump-Probe Transient of CS_2 from Balanced Detection. 35

Figure 3.5 Fourier-transform coherent phonon spectra (FT-CPS) from $CsPbBr_3$ The experimental setup: the two coherent, co-propagating pump pulses created by pulse shaping and the time-delayed probe pulse measures the transient birefringence. 36

Figure 4.1 TR-OKE transients from a $CH_3NH_3PbBr_3$ crystal. A OKE transients from $CH_3NH_3PbBr_3$ as a function of pump energy (1.85 – 2.30 eV). As it moves from non-resonant to pre-resonant condition, contribution from low-frequency motions coupled to electronic excitation are enhanced. As it reaches to the carrier-injection regime, additional sub-ps dynamics manifests itself. **B** Fourier component of each OKE transient. The inset is the crystalline structure of $CH_3NH_3PbBr_3$. Black ticks at the top show calculated frequencies of normal modes and sticks represent projections of the displacement vector on the normal modes upon large polaron formation (see **Figure 4.8**). From ref. [49]. Reprinted with permission from AAAS. 42

Figure 4.2 TR-OKE transients from a $CsPbBr_3$ crystal. A OKE transients from $CsPbBr_3$ as a function of pump energy (1.83 – 2.43 eV). At the pre-resonant regime, low frequency modes that is coupled to band-edge excitation is enhanced. At the carrier-injection regime, additional sub-ps dynamics manifests itself as well as long-lived polarization does. **B** Fourier spectra of selected transients in non-resonant regime (1.83, 2.00 eV), pre-resonant regime (2.21, 2.25 eV), and carrier injection regime (2.43 eV). The inset is the crystalline structure of $CsPbBr_3$. Black ticks at the top show calculated frequencies of normal modes and sticks represent projections of the displacement vector on the normal modes upon large polaron formation (see **Figure 4.9**). From ref. [49]. Reprinted with permission from AAAS. 45

Figure 4.3 Comparison of transient reflectance and TR-OKE with above-gap excitation. A Pseudo-color ($\Delta\alpha$)) representation of transient absorbance spectra of a $CH_3NH_3PbBr_3$ single crystal retrieved from transient reflectance ($\Delta R/R$) pumped by 2.92 eV, 100 μW. **B** The dynamics of screening extracted from transient reflectance probed at 2.31 eV for $CH_3NH_3PbBr_3$ (blue) and at 2.38 eV for $CsPbBr_3$ (red) as a function of pump–probe delay. The lines are mono-exponential fits convoluted with a gaussian function which describes cross-correlation between pump and probe pulse (FWHM 100 fs). **C** The structural dynamics triggered by photo-carrier injection as a function of pump-probe delay observed by TR-OKE with across gap excitation. $CH_3NH_3PbBr_3$ (blue) and at 2.38 eV for $CsPbBr_3$ (red) as a function of pump–probe delay. The lines are double-exponential fits convoluted with a gaussian function which describes cross-correlation between pump and probe pulse (FWHM 70 fs). From ref. [49]. Reprinted with permission from AAAS. 47

Figure 4.4 Hybrid DFT calculations. A The relaxed structures of $CH_3NH_3PbBr_3$ with positive and negative charge injection. Changes in Pb-Br-Pb bending and Pb-Br length are shown. **B-E** Potential energy surfaces for relaxation of the (**B, C**) $CH_3NH_3PbBr_3$ and (**D, E**) CsPbBr3 unit cell (four formula units) upon positive (**B, D**; red curve) and negative (**C, E**; blue curve) charge injection. The neutral state energy (black) along the distortion coordinate is also shown. From ref. [49]. Reprinted with permission from AAAS. 50

Figure 4.5. Estimation of polaron size from first principles. A Distribution of Pb-Br distances (Å, top panel) of the positive polaron state for a pseudo-cubic 2x2x8 $CsPbBr_3$ model made by 32 formula units. **B** The distribution of the excess positive charge (red isosurface) following the pattern of Pb-Br distances. The figure has been centered at the maximum of hole localization. From ref. [49]. Reprinted with permission from AAAS. 53

Figure 4.6 The spectra of pump pulses in the TR-OKE measurement for **A** $CH_3NH_3PbBr_3$ and **B** $CsPbBr_3$. Extinction coefficient (red broken line) from Ref. 181 and calculated penetration depth (black broken line) as a function of photon energy (a). Spectra of pump pulses (solid colored lines) and $\Delta R/R$ at the delay time at 5 ps (solid black line) are also shown (**A,B**). Red shaded areas show effective regions where photons are absorbed to create carriers estimated from the position of exciton absorption peak and its width extracted from the $\Delta R/R$ spectra and the penetration depth. From ref. [49]. Reprinted with permission from AAAS. 65

Figure 4.7 TR-OKE schematic and pump-polarization dependence of $CH_3NH_3PbBr_3$. A A schematic diagram of TR-OKE measurement. **B** Polar plots of TR-OKE signals for a $CH_3NH_3PbBr_3$ crystal as a function of the polarization of a pump pulse. (Red line) measured with $E\text{probe} \parallel [110]$ (Blue

line) $E_{probe} \parallel [100]$. (**C,D**) TR-OKE transients as a function of the polarization of a pump pulse **C** measured with $E_{probe} \parallel [110]$, **D** $E_{probe} \parallel [100]$. The black spectrum in **B** shows TR-OKE response from $CH_3NH_3PbBr_3$ with the pump polarization along the [100] crystal direction ($h\nu_1$ =2.0 ± 0.05 eV). The absolute signal intensity varies as a function of f and peaks at f = 45° (polar plot in the insert), confirming that the single comes from light-induced transient anisotropy with heterodyne detection. While the prompt rise of OKE signal can be attributed to the ultrafast electronic response represented by the laser pump-probe cross correlation (dashed curve), the signal remains for over 1 ps from nuclear contributions. The broad picosecond OKE response in **B** is distinctively different from those of typical solids, but is characteristic of OKE responses from liquids of anisotropic molecules. There are no oscillatory features in the TR-OKE response from $CH_3NH_3PbBr_3$, indicating that we are detecting predominantly over-damped phonon modes due to strong anharmonicity and dynamic disorder. Interestingly, the TR-OKE signal is suppressed by one order of magnitude when the pump electric field is changed from the [100] direction to the [110] direction. Note that the weak residual signal from polarization along the [110] direction does not show the dependence on f as expected from heterodyne detection of OKE signal (gray dots and curve in the polar plot); it likely comes from scattering of probe light from imperfections of the crystalline sample. From ref. [49]. Reprinted with permission from AAAS. 66

Figure 4.8 (Top panel) Calculated IR spectrum and the coefficients of the displacement vector associated with a positive charge injection in $CH_3NH_3PbBr_3$ projected to the normal modes. A-D show the four strongest-coupled modes to the displacement. (Lower panels) Specific atomic motions for selected normal modes. Strongly coupled modes (**A-D**) contain Pb-Br-Pb bending motion. Note that all the frequencies show higher frequency shifts compared to $CsPbBr_3$ due to the lighter cation mass. In addition, higher frequencies over 300 cm^{-1} which are assigned to pure CH_3NH_3 (MA) cation motions can be found, but their couplings to the displacement are almost negligible. These trends clearly show $PbBr_3$ framework largely contributes to large polaron formation even in the presence of MA cations, which is consistent with the observation of strong couplings on slow inorganic motions. From ref. [49]. Reprinted with permission from AAAS. 67

Figure 4.9 (Top panel) Calculated IR spectrum and the coefficients of the displacement vector associated with a positve charge injection in $CsPbBr_3$ projected to the normal modes. **A-D** show the four strongest-coupled modes to the displacement. (Lower panels) Specific atomic motions for selected normal modes. All strongly coupled 4 modes (**A-D**) clearly show Pb-Br-Pb bending. In contrast, modes at higher frequencies (>100 cm^{-1}) are less coupled. From ref. [49]. Reprinted with permission from AAAS. 68

Figure 4.10. **A,B** $\Delta R/R$ for $CH_3NH_3PbBr_3$ single crystal pump at 2.92 eV. **C** Comparison of the dynamics of transient reflectance and $\Delta\alpha$ in $CH_3NH_3PbBr_3$. The dynamics of retrieved $\Delta\alpha$ corresponds well with that of $\Delta R/R$. **D** Calculated $\Delta\alpha$ as a function of pump-probe delay in $CH_3NH_3PbBr_3$. Kramers-Kronig analysis clearly shows the change is rather red-shift than changing in the bleaching of the excitonic absorption at 2.35 eV. **E,F** $\Delta R/R$ for CsPbBr3 single crystal pump at 2.75 eV. **G** The dynamics of transient reflectance in CsPbBr3. **H** Time constants of sub-ps dynamics as a function of pump energy, showing the time constant is nearly independent of excitation energy. From ref. [49]. Reprinted with permission from AAAS. 69

Figure 4.11 Hybrid DFT calculations of the relaxed structures of $CH_3NH_3PbI_3$ with positive and negative charge injection. A Potential energy surfaces for relaxation upon positive (**A**; red curve) and negative (**B**; blue curve) charge injection. The neutral state energy (black) along the distortion coordinate is also shown. From ref. [49]. Reprinted with permission from AAAS. 70

Figure 4.12 Hybrid DFT calculations. Stabilization energy of $CH_3NH_3PbBr_3$ **A** and $CsPbBr_3$ **B** with positive added charge in the full system (left panels) and excluding the A-cations (right panels). Changes in Pb-Br-Pb bending and Pb-Br length for the full systems are also shown. The geometries of the systems without A-cations were kept fixed to those optimized by PBE0 for the full system. From ref. [49]. Reprinted with permission from AAAS. 71

Figure 4.13 Potential energy surface for the neutral (blue) and positive (red) charged 2x2x8 cubic $CsPbBr_3$ supercells as a function of the contraction of Pb-Br bond lengths (Å) and correspondingly of the lattice parameter along the long cell dimension. Notice that while the positively charge supercell shows a 0.10 eV stabilization, the neutral system does not show any stabilization, indicating the preferential stabilization of the positive charge along the explored Pb-Br coordinate. From ref. [49]. Reprinted with permission from AAAS. 72

Figure 4.14 Pseudo-cubic 2x2x8 $CsPbBr_3$ model with elongated (shortened) Pb-Br bonds in the left (right) halves of the supercell, superimposed to the excess negative (blue) and positive (red) charge densities from separate calculations on the entire supercell adding in turn a negative and positive charge. From ref. [49]. Reprinted with permission from AAAS. 73

Figure 4.15 Exploring the localization of the positive charge as a function of the octahedral tilting in the left 2x2x8 $CsPbBr_3$ supercell side. Notice the preferential localization of the positive charge in the untilted, right side of the Figure. Along with reducing the tilting angle from 180° to 165°, a lengthening

of the Pb-Br bonds of ~0.06 Å is computed. From ref. [49]. Reprinted with permission from AAAS. 74

Figure 4.16 Calculated dielectric functions of $CsPbBr_3$ (solid lines) and $MAPbBr_3$ (dashed lines) in far infrared region. Real part (red), imaginary part (blue) of dielectric function and imaginary part of the inverse dielectric function (black). The dominant LO phonon frequencies are at 194 and 136 cm^{-1} for $CsPbBr_3$ and $MAPbBr_3$, respectively. From ref. [49]. Reprinted with permission from AAAS. 75

Table 4.1 The list of input parameters for the polaron calculations. Optical and static dielectric constants (ε_∞ and ε_0, respectively), angular frequencies of a characteristic LO phonon mode ($\boldsymbol{\omega}$), and effective masses of bare electron bands (m). From ref. [49]. Reprinted with permission from AAAS. 76

Table 4.2 The list of calculated parameters for the polarons. Fröhlich coupling constants ($\boldsymbol{\alpha}$), phonon occupation factors ($\boldsymbol{\beta}$), parameters at the lowest energy polaron in the Feynman-Osaka model (v and w), Feynman polaron radii ($\boldsymbol{\rho}$) and mobilities ($\boldsymbol{\mu}$). From ref. [49]. Reprinted with permission from AAAS. 76

Figure 5.1 CsPbBr3 at 295 K. A CP trace with $h\nu_1$ = 2.25 and $h\nu_2$= 1.55 eV for pump-probe delay (Δt) up to 7 ps. The dashed curve is a single exponential fit, which represents an incoherent background. **B** FT of the CP trace in **A** with the background subtracted. **C** The background subtracted CP trace (black, intensity x5 for Δt > 1 ps) in comparison to two sine waves (blue, 2.5 THz; red, 1.6 THz). The vertical dashes mark the peaks of the sine waves. **D** Pseudo color (FT amplitude) representation from a moving-window FT analysis of the CP trace in **A**. The grey dots mark the peak position in the 2.6-1.6 THz range. 80

Figure 5.2 TR-OKE of $CsPbBr_3$ at 295 K with $h\nu_1$ = 2.05 eV and $h\nu_2$ = 1.55 eV. **A** CP trace (black) for pump-probe delay (Δt) up to 4 ps. The trace for Δt > 0.7 ps is multiplied by 5x and reproduced as the grey trace. **B** Pseudo color (FT amplitude) representation from a moving-window FFT analysis of the CP trace in **A**. The blue dashed line shows the center frequency at 3.9 THz. 82

Figure 5.3 Model simulation of coherent phonon-to-phonon transfer and comparison to experiment. A Schematic illustration of parametric decay; **B** Excitation laser power dependence of the coherent phonon amplitudes. Blue-circles: the 5.3 THz mode; red circles: the 2.6-1.6 THz modes. The lines are linear fits. **C** Simulation results from equations (5.2.2) and (5.2.3) of the time-evolution of the 5.3 THz (blue) to 2.65 THz (red) modes. **D** A comparison of

simulated coherent phonon oscillations (black) with experimental result from **Figure 5.1** (red). 85

Table 5.1 Parameters used in the evaluation of equations (5.4.4) and (5.4.5). 92

Figure 5.4 Comparison of linear and circular birefringence A, **B** The raw data taken with pump excitation of 550 nm, 0.15 mW. **C**, **D** The raw data taken with pump excitation of 605 nm, 0.35 mW. The trace taken with the quarter waveplate (QWP), shown in dark blue and red, shows the pump-induced change in probe ellipticity. The trace taken with the half waveplate (HWP), shown in light blue and purple, shows the pump-induced change in linear polarization of the probe. In these experiments, the coherent features are visible in traces from both the HWP and QWP. As expected in coherent phonon spectroscopy, the linear and circular birefringence are modulated in the same way by the coherent phonon. The electronic Kerr effect leads to a different response in only the incoherent part of the signal. 93

Figure 5.5 Time-frequency analysis for different pump excitation wavelengths. A OKE transients previously reported by Miyata and coworkers for pump excitation wavelengths of 660 nm (1.88 eV), 620 nm (2.00 eV), 580 nm (2.14 eV), 560 nm (2.21 eV), and 550 nm (2.25 eV)[49]. These data sets are from different $CsPbBr_3$ samples and are taken with a different experimental setup, in which the anisotropic polarization change is detected by the pump-induced change in intensity of a cross-polarized 800 nm probe. The respective short-time Fourier transform analyses are shown in **B** – **F**. This analysis is described Section 5.4.2. We see that the coherent coupling and softening of phonons arises only as the pump excitation energy approaches the bandgap energy, confirming that this extreme anharmonic behavior is only observed in the presence of photoexcited charge carriers..... 94

Figure 5.6 Fluence-dependent CPS traces with 550 nm pump excitation. A The raw data taken with pump fluences of 191, 127, 64, 32, and 13 $\mu J/cm^2$. The incoherent contribution is shown with gray-broken traces (single-exponential decay). **B** The coherent contribution to the CPS trace, taken by subtracting the incoherent part in **A** from the respective raw trace. The gray shaded regions indicate areas in which the high-frequency and low-frequency phonon contributions are separated. The red markers indicate the maximum in the gray shaded regions, the blue markers indicate the minimum in the same regions. The phonon amplitude used in **Figure 5.3** is calculated by taking the difference between the respective maxima and minima (peak to peak) for each phonon frequency for each trace. **C** The Fourier transform (FT) of the raw data shown in **A**. The blue and red markers indicate the maximum FT amplitude of the respective gray shaded regions. D The maxima of the phonon peaks in C plotted against pump power. As shown, both the higher frequency and lower

frequency phonons scale linearly with fluence. This agrees very well with the linear fits shown in **Figure 5.3.** 95

Figure 5.7 Dephasing times for coherent phonons. Here, we fit a Lorentzian to the phonon peaks in the Fourier Transform (FT) intensity. The dephasing time is given by $\pi * FWHM - 1$ where the full-width half maximum (FWHM) of the Lorentzian fit is in THz. **A** The CP signal when the pump wavelength is 605 nm. Here, we take the FT of the coherent oscillations, which are shown by the red trace. The inset shows the intensity of the FT of this region. Fitting a Lorentzian to the peak at 4 THz yields a FWHM of 0.45 THz and a dephasing time of 0.72 ps. **B** The CPS transient when the pump wavelength is 550 nm. We show the square of the FFT of the entire transient. Fitting a Lorentzian to the peak at 5.3 THz yields a FWHM of 1 THz and a dephasing time of 0.32 ps. 96

Figure 5.8 Comparison of Coherent Phonon Spectroscopy and Fourier-Transform Coherent Phonon Spectroscopy (FT-CPS). A The pump-energy resolved Fourier transform of FT-CPS on $CsPbBr_3$ (**Figure 6.2**). As the pump excitation energy decreases from the bandgap (E_g) , 2.30 eV, to 150 meV below the bandgap, the initial phonon hardens with decreasing excitation energy from 3.5 THz to 7.0 THz. The dotted line indicates that at an excitation energy of 2.25 eV the corresponding phonon frequency is 5.2 THz. **B, C** The static Fourier transform and the one-dimensional CP trace of $CsPbBr_3$ excited at 2.25 eV. The initial high-frequency phonon in c corresponds to the broad peak centered at 5.3 THz in **B**. Note that **A** and **B** share a frequency axis, and the close match between the dotted line (5.2 THz) and the solid line (5.3 THz) emphasizes the agreement between FT-CPS and 1D CPS. 97

Figure 6.1 Fourier-transform coherent phonon spectra (FT-CPS) from $CsPbBr_3$. A Pseudo-color (transient birefringence) 2D plot of FT-CP spectra from a CsPbBr3 single crystal at 295 K. The excitation energy (Eex) comes from Fourier-transform along the time delay (t) between the two coherent pulses. The positions of the estimated bandgap (Eg) and selected Eex values for horizontal cuts (panel **B**) in the 2D spectra are shown as dashed lines. In addition to the horizonal cuts (blue to green), shown in **B** are single pulse excitation (1D) spectrum (gray) and E_{ex}-integrated 2D spectrum (red). 101

Figure 6.2 Correlation between excitation energy and coherent phonon frequency. The 2D pseudo-color plot obtained from the Fourier transform (FFT) with respect to Δt from the FT-CP spectra in **Figure 6.1B**. The color scale is the FFT amplitude. 104

Figure 6.3 Model shows the correlation between the binding energy of ferroelectric potential and phonon frequency. A Generic Landau potentials for the ferroelectric double well in the ground state (U) and excited state (U^*). In the latter, the different extents of distortion (black→ green → blue) correspond to linearly increasing electric fields (E_e) from the charge pair separated at ferroelectric domain boundaries, as illustrated in **B**. **C** A comparison of model simulation result (green dashed curve) with four experimental data sets (black markers) from FT-CPS of three different $CsPbBr_3$ crystals. The phonon frequency is normalized to that at zero binding energy, i.e., free carriers with across E_g excitation. **D** Simulated coherent phonon oscillations for the five U^* curves in **A**, vertically offset for clearer visibility. 106

Figure 6.4 FT-CP spectra from $CH_3NH_3PbBr_3$. A Pseudo-color (transient birefringence) 2D plot of FT-CP spectra from a $CH_3NH_3PbBr_3$ single crystal at 295 K. The positions of the estimated bandgap (E_g) and selected E_{ex} values for horizontal cuts (panel **B**) in the 2D spectra are shown as dashed lines. In addition to the horizonal cuts (blue to green), shown in **B** are 1D spectrum (gray) and E_{ex}-integrated 2D spectrum (red). 109

Figure 6.5 Time-time domain raw data and Fourier transform. A, Raw data of the FT-CPS shown in the main paper. Here the pump-pump steps size was 5 fs. **B**, Zoom-in of the first 500 fs where the main coherent features are found. The electronic coherence time clearly approaches 500 fs. **C**,**D**, Fourier transform with respect to the pump-pump delay for **A** and **B**, respectively. **D**, The Fourier transform of the first 500 fs of the pump-pump delay already contains the main FT-CPS features of **C**. 115

Figure 6.6 Extended line cuts for specific excitation energies. A, B, Time-frequency domain FT-CPS and the corresponding line cuts for fixed excitation energies as in **Figure 5.1A, B**, respectively. The time domain traces in B are vertically offset for clarity. The excitation energy-integrated FT-CPS (red line) agrees well with the single pulse excitation (grey line). **C**, Corresponding Fourier transforms of the line cuts in **B**. Already in these few line cuts a significant frequency shift is prominent for excitation energies ranging from 2.15 eV to 2.29 eV. The dominant high-frequency feature likely sits on top of smaller, less resolved low-frequency components, which is consistent with previously published OKE. The increased broad low frequency background for low E_{ex} originates from the displacive offset. 116

Figure 6.7 FT-CPS in a $CsPbBr_3$ samples with longer phonon coherence time. We investigated in total 3 different $CsPbBr_3$ samples, which vary in crystal quality and thickness. **A**, This sample shows the same characteristic features as **Figure 5.1A** despite the longer phonon coherence time and less pronounced oscillations at lower excitation energy (< 2.2 eV). **B** Pump photon energy

spectrum. The high energy cutoff of the FT-CPS signal at 2.30 eV in **A**, is due to a drastic decrease in penetration depth and therefore decreased effective probing volume. As there are still significant photon energy components below 2.2 eV, the decline of the signal in this region is likely related to a vanishing density of highly localized electron-hole states C, The absolute frequency distribution and frequency shift is consistent with **Figure 6.2** and with the global fit of our model (see **Figure 6.9** and **Figure 6.11**). 117

Figure 6.8 Line cuts for FT-CPS signal in Figure 6.7. **A** FT-CPS signal as shown in **Figure 6.7A**. **B** Line cuts for fixed excitation energy corresponding to the dashed lines in a. Here the longer phonon coherence time unveils low frequency beating. Interestingly, the low frequency beating nodes exhibit an opposite dependence on the excitation energy E_{ex}: For higher E_{ex} the beat frequency becomes higher. This beating might be related to coupled other modes. Also, here the integrated FT-CPS signal perfectly matches the single pulse excitation signal (1D OKE) and moreover explains the complicated nature and fast dephasing of the 1D signal. **C** Fourier transform of corresponding line cuts in **B**. Despite the more structured main frequency peak, the frequency shift agrees with **Figure 6.6**. 118

Figure 6.9 Comparison linear polarization change and change in ellipticity. A, 2D FFT of FT-CPS signal detected by a balanced detection with half-wave plate (HWP) corresponding to a transient change in linear probe polarization (same as **Figure 6.7C**). **B**, Same experimental conditions as in **A**, but detecting the transient change in probe ellipticity with a quarter-wave plate (QWP). As known from most coherent phonon studies, the phonon amplitude modulates both ellipticity and linear polarization in similar way. Only the magnitude of the QWP and HWP signal is different. 119

Figure 6.10 Model details for simulations in Figure 6.3. A, Lattice potentials $U(Q,0)$ (black line) and excited state potentials $U^*(Q,E_e)$ (colored lines) for linearly increasing local charge separation field E_e. To simulate a displacive excitation, the lattice coordinate Q of the unperturbed potential minimum (blue cross) is used as starting point $Q_0 = Q(t=0)$ (red crosses) for solving the equation of motion. **B**, Solutions of the equation of motion of the potentials in **A**. The phonon amplitudes $Q(t)$ are vertically offset for clearer visibility. A selection of the traces in **A**, and **B**, are shown in **Figure 6.3A** and **B**, respectively. **C**, A Fourier transform of the data in **B**, unveils the increasing frequency shift (normalized to the initial frequency of the unperturbed potential) with increasing E_e resulting from the high anharmonicity of the unperturbed potential. **D**, Phonon center frequency shift and potential minimum shift as a function of E_e. An increase of the local field E_e by one order of magnitude leads to a doubling of the phonon frequency. Plotting the potential minimum shift against the phonon frequency gives the theory curve

for **Figure 6.3C** (by fitting the barrier height of the unperturbed potential as a scaling factor to U_d = 15 meV)..... 120

Figure 6.11 Global model fit. The anharmonicity of the potential $U(Q, 0)$ with a linear increasing local field E_e in $U^*(Q, E_e)$ (both in arbitrary units) is globally fit to four experimental data sets of the phonon frequency shift as a function of the binding energy. The unperturbed double well barrier height U_d is used as a free scaling parameter. A good match to all experimental data sets is found for U_d = 15 meV. **A**, Modeled potential energy in meV after global fit and scaling to experimental data. **B**, **C**, The same model parameters agree well with the data sets shown in the main paper (**Figure 6.2**) and extended data (**Figure 6.7C**), respectively. The black line in **B** and **C** is the identical model curve. 121

Figure A.1 Optical Images and Diffraction of $CsPbBr_3$ and $MAPbBr_3$. A, **C** Optical image and SCXRD of $CsPbBr_3$ and, **B**, **D**, of $MAPbBr_3$..... 145

Table A.1. Lattice constants for cubic $MAPbBr_3$ (space group *P*m3m) and orthorhombic $CsPbBr_3$ (space group Pbnm). 146

Acknowledgments

First and foremost, I am deeply grateful to my advisor, Professor Xiaoyang Zhu. As a scientist he is astute and creative, and as a mentor he is dedicated, patient, and encouraging. The XYZ research group strikes a delicate balance of intellectual combativeness and personal warmth; it is a testament to the example that Xiaoyang sets for us. I cannot articulate enough how crucial his support has been, especially in the most difficult moments of my PhD. It is a privilege to become a scientist in this research group.

I owe a lot of gratitude to my thesis committee. Professor Louis Brus and Professor Xavier Roy have comprised my advisory committee since my first year. Over the course of my PhD, Louis has offered sharp insight in scientific discussions and valuable professional advice. Many of his quiet comments have guided my own scientific understanding and interests. I am thankful for Xav's exceptional generosity and support, especially as I take my next professional steps. In addition, his rigorous approach to science has helped refine my own critical thinking abilities in this field.

During her sabbatical here, Professor Efrat Lifshitz offered many incisive comments on a very broad range of topics. I learned a great deal from her, and I am grateful for her participation in my committee. Finally, Professor Laura Kaufman has graciously shared her own experiences with me as I move beyond graduate school, and her candor has bolstered my confidence. Furthermore, as the Director of Graduate Studies, she is a diligent advocate for a transparent, equal, and inclusive department. It means so much to me to see these values emphatically reaffirmed at

the department level. I am very grateful for her voice in the Columbia Chemistry community.

In addition to my committee, I am grateful for the contributions of my theory collaborators without whom critical insights would not be possible: Professor Filippo De Angelis, Dr. Daniele Meggiolaro, Dr. Edoardo Mosconi, and Dr. Dominik Juraschek. In addition, I am thankful for the excellent scientific discussions with Louis, Professor Simon Billinge, and Professor Nicola Spaldin that have helped shape this work.

On a more personal level, I have been very fortunate to be surrounded by excellent scientists in the XYZ group. Individually and collectively they are kind, intelligent, hard working, and hilariously irreverent. Dr. Sebastian Maehrlein is a walking, talking nonlinear phononics encyclopedia. More importantly, he is a wonderful teacher, collaborator, colleague, and friend. I have learned so much from our many in-depth discussions, scientific and otherwise, and I am very sorry to leave them behind. Dr. Fang Liu has spent years helping me nurture, dismantle, and resurrect an impossibly fickle amplifier system. Besides being a miracle-worker, Fang is an incredible baker and is slowly fattening up the entire group. Dr. Feifan Wang is cheery (and exceptionally tolerant) and has patiently accepted my stringent sample requests and returned beautiful single crystal perovskites. I owe many, many exciting results to Feifan's effort. I am very grateful for the mentorship of Professor Kiyoshi Miyata, whose signature philosophy is, "Let's just try it." Kiyoshi taught me so much and very critically helped build my confidence as an experimentalist. I should also note that Miyata-senpai is the undisputed king of karaoke. Dr. Daniel Niesner gave

me my first introduction to ultrafast lasers, ultrahigh vacuum, and perovskites, and I am thankful for his continued help and friendship.

The group makes my days brighter, and I will miss the great times we've had over group lunch, beers, karaoke, and laser tag. Thank you to: Dr. Mark Ziffer, Dr. Yusong Bai, Dr. Doyk Hwang, Dr. Yanan Dai, Dr. Timothy Atallah, Dr. Kris Williams, Dr. Tyler Evans, Dr. Xinjue Zhong, Dr. Kihong Lee, (soon-to-be) Dr. Jue Wang, Drew Schlaus, Felisa Conrad-Burton, Michael Scott Spencer, Kameron Hansen, Yufeng Wang, and Skyler Jones. Not least, Koba and Fufy buoy a significant fraction of group morale. For their tireless work, they deserve lots of praise, pets, treats, and tennis balls.

I owe so much to my friends in this department. They are sources of inspiration and support, and they have supplied many of my best memories of graduate school. I am excited to see where they all go, but I will miss their presence. I cannot imagine the past five years without the support, humor, and intellect of Dr. Alyssa Manz and Dr. Kihong Lee. I am so lucky to have them. I am thankful to Dr. Melissa Ball for her support and her seemingly unending drive. She is an inspiring peer, and I cannot wait to see where she goes next. I also want to thank Dr. James Shee and Karen Kwon, who never fail to bring lightness and laughter into my day.

My beloved Chicago family has been there from both near and afar. I am so grateful for their empathy, wit, and willingness to learn about Ti:sapphire lasers. Defne Ozaltun, Stephen Li, Yen-Li Thompson, Aleks Penev, Mary Kate Cunningham, Michael Helzer, and Jackie Todd have made New York City home for me. Despite the distance, Kate Marsden, Anjuli Uhlig, Iliya Gutin, and John Gallagher are always willing to lend an ear and share their wisdom.

I am so thankful to my cousin, Tripti, and her family. Their doors are always open to me, and their love and company have kept me afloat on many hard days. In addition, I am grateful to Luc Demortier, who is essentially an uncle to me and has been an unparalleled guide to Manhattan and a constant source of encouragement and entertainment.

Finally, I owe everything to my parents, who have carefully nurtured my curiosity and encouraged me in every way. Every aspiration of mine is lifted by their confidence, and every success is inspired by their resolve. I could not be here without their love.

For my parents

1 Motivation

1.1 Overview

As global fossil fuel dependence becomes an increasing environmental and existential threat, the need for carbon emission-free energy sources has become alarmingly clear[1]. Such an infrastructural overhaul requires the widespread availability of cheap, efficient, and emissions-free renewable energy sources. This demand necessitates rapid innovation in alternative energy sectors, particularly solar power, which historically has been prohibitively expensive[2]. In the past decade, lead halide perovskites (LHPs) have been established as a unique and promising material class for next-generation photovoltaics[3]. Since their initial incorporation into solar cells in 2009, the efficiency of LHP-based solar cells has soared from 3.8%[4] to 23.7% in 2019[5]. The efficiency of LHP-based single junction devices is now competitive with the maximum reported of efficiencies of single-crystalline gallium arsenide (GaAs) and silicon-based (Si) analogs (27.8% and 26.1%)[5].

LHPs are an especially appealing alternative because their production process is cheap and solutions-based, which sharply contrasts with the expensive and toxic production of Si, the most prevalent semiconductor in solar cells[6]. In addition, the efficiency of LHP polycrystalline thin films is competitive with Si despite their high defect density. The paradigm governing conventional semiconductors is that higher purity yields higher efficiency. For example, Si-based solar cells require five nines (5N, 99.999%) to ten nines (10N) purity, whereas electronics-grade Si requires eleven nines (11N) purity[6]. In comparison, the defect density of LHP polycrystalline thin films is ~10^{16} cm^{-3}, which is several orders of magnitude higher than that of

crystalline Si[7–11]. This discrepancy underscores the fundamental allure of LHPs, which is the potential to abandon this purity-efficiency paradigm.

Underlying the anomalous efficiency of LHPs are a number of outstanding optoelectronic properties: long carrier lifetimes[12,13], long carrier diffusion lengths[14–17], high radiative efficiencies[18,19], long-lived hot carriers[20–24], and trap-free hot carrier relaxation[18]. In aggregate, these properties reflect strong defect tolerance and dynamic screening of charge carriers. LHPs also demonstrate band-like transport and modest mobilities[25–27], suggesting that charge carriers are dynamically screened by large polarons[28]. In this picture, the lattice couples to charge carriers and inhibits Coulomb-mediated scattering with defects, other carriers, and LO phonons[28–33].

Understanding the structural dynamics of charge carrier screening is critical for strategic design of other defect-tolerant semiconductor materials. Although it provides a general picture of carrier screening, the conventional Fröhlich polaron picture is insufficient to describe the observed behavior of LHPs. The Fröhlich interaction relies on the harmonic coupling of a carrier to one phonon, and therefore cannot accommodate the pronounced anharmonic phonon-phonon couplings and dynamic disorder of the LHP lattice. The premise of this thesis is to investigate these anharmonic phonon dynamics on the ultrafast timescale. In order to do so, we probe coherent phonons in the presence of charge carriers in single-crystalline $CsPbBr_3$ using coherent phonon spectroscopy.

1.2 Thesis Structure

In Chapter 2, I provide an overview of LHPs, namely their electronic and lattice structure, dynamic disorder, and dielectric screening. Importantly, the

anharmonic polar displacements and dielectric screening of LHPs resemble those of other material classes, particularly emphanitic materials such as the lead chalcogenides and known ferroelectric materials such as the titanium oxide perovskites. I briefly introduce the Fröhlich large polaron model in order to generally describe the physical origins of the optoelectronic properties of LHPs. Because the Fröhlich model is predicated on the assumption of harmonic oscillators in the linear carrier-phonon coupling limit, it cannot fully describe the behavior of highly anharmonic LHPS. To rectify this, Miyata and Zhu propose a ferroelectric large polaron, in which the polar nanodomains observed in LHPs add ferroelectric screening character to the large polaron[34]. Finally, I describe previous time-resolved optical Kerr effect measurements that motivated the work presented in this thesis.

Chapter 3 contains an overview of the laser setups and detection systems used in time-resolved optical Kerr effect spectroscopy (TR-OKE) and coherent phonon spectroscopy (CPS). A critical advantage of our implementation of CPS is single-shot balanced detection in place of single-shot optical heterodyne detection (OHD) used in TR-OKE. OHD extracts the pump-induced polarization anisotropy from the intensity of the probe pulse, whereas balanced detection directly probes the polarization rotation of the probe pulse. Balanced detection is also a zero-background detection scheme, meaning that it provides a higher signal-to-noise ratio. We also introduce a two-dimensional technique called Fourier-transform coherent phonon spectroscopy (FT-CPS) in order to spectrally resolve ultrafast lattice responses according to the excitation energy.

In Chapter 4, TR-OKE is used to probe the ultrafast structural dynamics of $MAPbBr_3$ and $CsPbBr_3$. The respective LHPs are excited with a linearly polarized

visible pump pulse, and the transient birefringence is probed with a linearly polarized near-IR probe pulse. The pump photon energy is incrementally increased to investigate the structural response of LHPs in the non-resonant, pre-resonant, and above-resonance excitation regimes (>2.3 eV). When charges are injected, the OKE transient is described by two decay time constants: a sub-picosecond component called τ_1 and a longer lived anisotropy called τ_2. τ_1 is ~0.3 ps and ~0.7 ps for respectively for $MAPbBr_3$ and $CsPbBr_3$. τ_1 is interpreted to be the large polaron formation time. This decay time agrees extremely well with the lifetimes of a transient redshift (0.28 ps and 0.6 ps, respectively) in the bandgap observed in complementary transient reflectance measurements. This redshift is attributed to band renormalization due to many-body Coulomb interactions, and its disappearance is interpreted as the screening of the Coulomb interactions by large polaron formation. As discussed in Section 2.5 the polaron formation time reported for $MAPbBr_3$ is consistent with previous two-photon photoemission (2PPE)[21] and time-resolved multi-THz spectroscopy (TRTS)[35] measurements.

The motivation for Chapters 5 and 6 comes from the case where the LHPs are excited with photon energies below the electronic transition. $MAPbBr_3$ exhibits an over-damped liquid-like anisotropy that lengthens in time as it approaches the electronic transition. In contrast, in the non-resonant regime, $CsPbBr_3$ demonstrates behavior that is more reminiscent of solids: an instantaneous response that with Raman-active vibrations. As $h\nu_1$ increases from 1.83 eV to 2.21 eV, we observe the emergence of rich phonon behavior. In the non-resonant regime, we observe a ~4 THz coherent phonon. When $h\nu_1$ is 2.21 or 2.25 eV, we observe a sub-ps high-

amplitude fast oscillation followed by a longer-lived lower-amplitude slow oscillation. The physical origin of these phonon dynamics was not addressed at the time.

In Chapter 5, we excite $CsPbBr_3$ in the absorption tail, which introduces a dilute carrier population. To better resolve the coherent phonon responses described in Section 4.3, we implement single-shot balanced detection. We find an initial ~5.3 THz phonon that coherently decays to ~2.6 THz phonons at the Γ point. Interestingly, this initial phonon frequency is higher than any mode calculated for the ground state by density functional theory (DFT). We also observe the coherent softening of the ~2.6 phonon mode to ~1.6 THz. The magnitude of this softening is unprecedented. These behaviors are absent when $CsPbBr_3$ is excited far below its bandgap, suggesting that the presence of carriers amplifies phonon anharmonicity.

In Chapter 6, we excite $CsPbBr_3$ in the absorption tail with a broadband pump pulse. We implement FT-CPS in order to finely resolve the pump-wavelength dependence of the coherent phonon response. From 150 to 0 meV below the bandgap, we observe a ~7.0 THz coherent phonon that dramatically softens to ~3.5 THz, which is indicative of strongly anharmonic lattice vibrations coupled to a localized charge. This behavior can be described by a ferroelectric double-well potential adjusted by an applied electric field from a photoexcited electron-hole pair. We suggest that these results provide spectroscopic evidence for ferroelectric charge carrier localization, i.e. a ferroelectric large polaron.

Chapter 7 contains concluding remarks on carrier-coupled phonon dynamics in LHPs. I have suggested several potential experimental directions that I believe would help clarify questions raised by the experiments in Chapters 5 and 6.

2 Material Properties of Lead Halide Perovskites

Abstract

The premise of my experiments has developed from a rich body of literature regarding the LHPs' structural and optoelectronic properties. This chapter is intended to introduce this context and to guide the eventual progression to dynamic charge carrier screening and the ferroelectric large polaron hypothesis. In the first section, I briefly summarize characteristics of LHPs' macroscopic lattices and electronic structures. LHPs are soft, polar materials that exhibit significant dynamic disorder, which adds several layers of complexity to understanding carrier-lattice interactions. The respective contributions of the individual sublattices to dynamic disorder and charge carrier screening has been a controversial topic in the field. This discussion is followed by an overview of dielectric screening in these materials. The disorder and dielectric screening are critical attributes of large polaron screening. I give a brief summary of the Fröhlich polaron model and the evidence for large polaron screening in LHPs. Because the Fröhlich model is predicated on the assumption of harmonic oscillators and because LHPs are demonstrably anharmonic, the Fröhlich polaron model is clearly insufficient to mechanistically describe carrier screening in LHPs. Finally, I describe the recently proposed ferroelectric polaron model, in which polar nanodomains additionally screen the charge carrier.

2.1 Lattice and Electronic Structure

The lead halide perovskite structure is described by the chemical formula $APbX_3$ where A^+ is typically Cs^+, $CH_3NH_3^+$ (methylammonium, abbreviated MA^+), or $CH(NH_2)_2^+$ (formamidinium, abbreviated FA^+), and X^- is a halide, typically Br^- or I^-. The perovskite lattice is composed of two interpenetrating sublattices, such that an A^+ sublattice interspersed among a lattice of corner-shared BX_6^{4-} octahedra and each A^+ cation is surrounded by 12 X^- anions. A cubic-phase unit cell is shown in **Figure 2.1**.

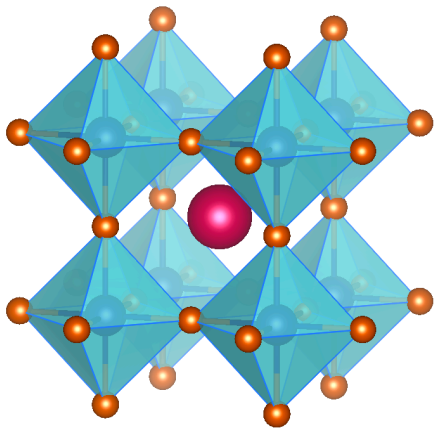

Figure 2.1 Cubic Lead Halide Perovskite (LHP) structure. The A-site cations (magenta) are interspersed between a sublattice of PbX_6^{4-} corner-shared octahedrals. Pb^{2+} is shown in dark blue, X^- is shown in orange, and the octahedral is shaded in light blue

The majority of LHP literature focuses on $MAPbI_3$ and my own experiments use $CsPbBr_3$ and $MAPbBr_3$ as model systems. For this reason, I will primarily discuss the properties of these three species. All three have a low-temperature orthorhombic phase, and with increasing temperature, subsequently enter the tetragonal phase, and then the high-temperature cubic phase[36,37]. Relative to the high-symmetry cubic phase, the orthorhombic phase is characterized by distortion and tilting of the PbX_6^{4-}

octahedra, as shown in **Figure 2.2A**. **Figure 2.2B** and **C** show the average crystal structures of the tetragonal and cubic phases, respectively.

At room temperature (298 K), $CsPbBr_3$ is in the low-symmetry orthorhombic phase, $MAPbBr_3$ is the high-symmetry cubic phase, and $MAPbI_3$ is in the tetragonal phase[36–38]. As detailed in a later section, these phase designations here are a description of macroscopic lattice structure and do not adequately describe local structural fluctuations.

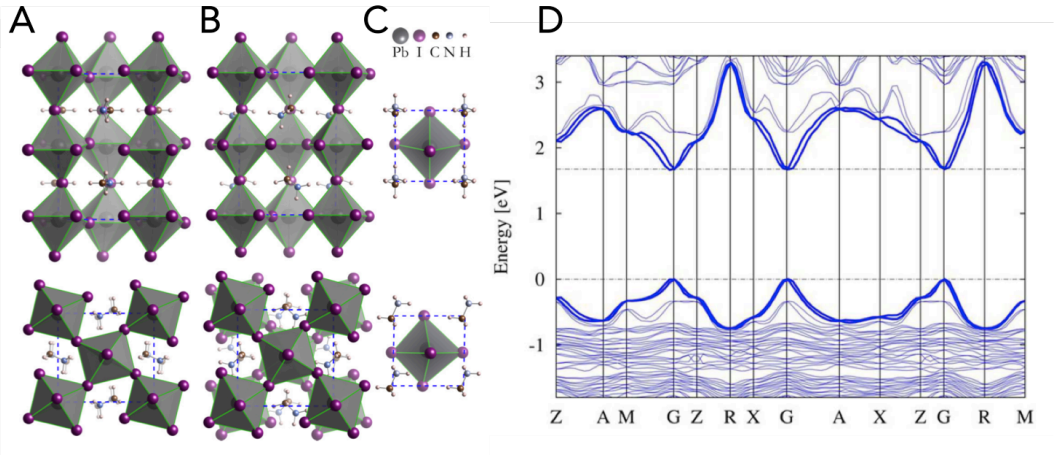

Figure 2.2 Structural phases and electronic band structure of MAPbI3. Crystal structures of A orthorhombic phase, **B** tetragonal phase, and **C c**ubic phase MAPbI3. The ⟨100⟩ and ⟨001⟩ orientations are shown in the upper and lower panels, respectively. Reproduced with permission from ref. [37]. Copyright 2015 by the American Physical Society. **D** The electronic band structure of MAPbI3 as calculated by SOC-GW reveals a direct band gap at the Γ point. Reproduced with permission from ref. [41]. Copyright 2014 Springer Nature.

The electronic structure of LHPs is dominated by the contribution of the PbX_6^{4-} octahedra. In $MAPbI_3$, valence band maximum (VBM) is determined by the mixing of the Pb 6*s* and I 5*p* orbitals and the conduction band minimum (CBM) is determined by the Pb 6*p* and I 5*s* orbitals[39]. Similarly, the VBM and CBM of lead bromide perovskites are determined by the mixing of Pb and Br orbitals[40]. LHPs are characterized by a direct band-gaps at the *Γ* point, as shown in the electronic band

structure as calculated by spin-orbit coupling GW (SOC-GW) in **Figure 2.2D**[41]. The band gap of $MAPbI_3$ at room temperature is 1.6 eV, which makes it highly suitable for photovoltaic devices. Unusually, the band gap increases as temperature increases, which is the opposite trend of most semiconductors, but common in polar lead-based solids[42–47]. $MAPbBr_3$ and $CsPbBr_3$ have band-gaps of 2.28 and 2.35 eV, respectively[48,49], which allow greater flexibility for spectroscopic measurements in the visible wavelength range. The exciton binding energies of lead iodide and lead bromide perovskites are lower than the thermal energy k_BT at room temperature (~26 meV), meaning that there is minimal exciton contribution to the investigated structural dynamics[50–55].

2.2 Dynamic Disorder of A-Site Cations

The question of which sublattice dominantly contributes to dynamic screening in LHPs has been a recent point of controversy. In this section and the next, I provide an overview of dynamic disorder contributions originating from the A^+ and PbX_6^{4-} sublattices.

In hybrid organic-inorganic LHPs such as $MAPbI_3$ or $MAPbBr_3$, the polar A-site cations are dynamically disordered at room temperature[56]. The MA^+ cations are confined to pores in the cuboctahedral cage formed by the lead halide sublattice. The dynamics of the MA^+ cations depends strongly on the temperature and structural phase of the LHP. In the low-temperature orthorhombic phase, ^2H NMR experiments indicate that rotation of the C-N bond itself is frustrated and the dynamic disorder of the MA^+ cation is primarily due to rotation around the C-N

axis[57]. The NH_3 group of MA^+ forms hydrogen bonds with the X^- anions of the inorganic cages, meaning that the orientation of the C-N bond is coupled to the tilting of the PbX_6^{4-} octahedra[58–61].

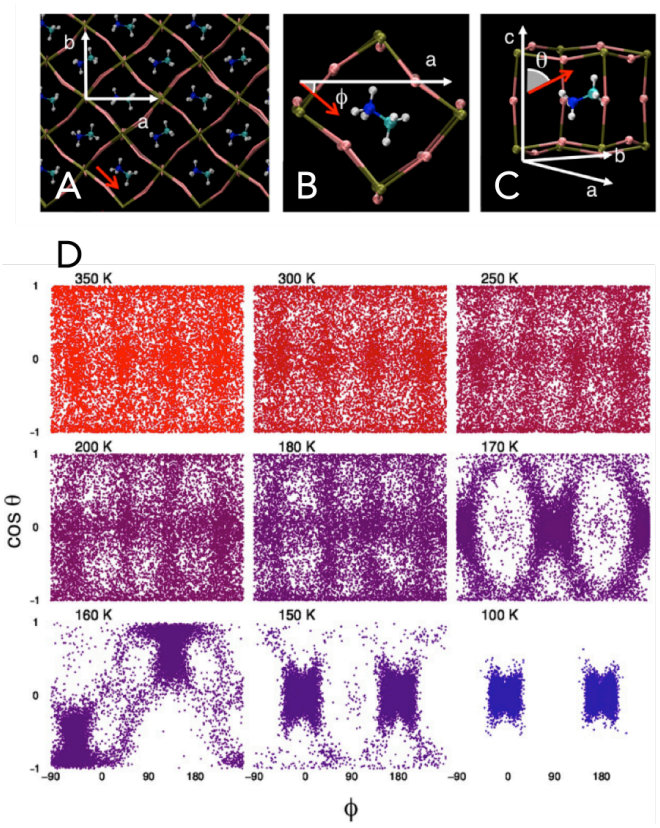

Figure 2.3 Fluctuations of MA+ orientation as a function of temperature. A The a and b axes of orthorhombic-phase $MAPbI_3$. **B** The azimuthal angle ϕ is defined as the angle of rotation in the a-b plane. **C** The polar angle θ is defined as the angle of the C-N bond with respect to the c-axis. **D** The distribution of angular orientations of the C-N bond as a function of temperature. Reprinted with permission from Ref. [64]. Copyright 2015 American Chemical Society.

As the lattice reaches higher phase temperatures, the reorientation of the MA^+ cation gains additional degrees of freedom. In the tetragonal phase, the C-N axis of MA^+ can reorient relative to the crystal. NMR and neutron diffraction measurements report that the C-N bond tumbles inside the lead iodide cage of tetragonal $MAPbI_3$ such that the C-N preferentially orients toward one of the four

faces of the cuboctahedral cage and "jumps" between orientations[37,62]. Two dimensional infrared spectroscopy (2D IR) measurements report that this jump-like motion has a period of ~3 ps, and additionally that MA^+ experiences a librational "wobbling in a cone" motion with a period of ~300 fs[63].

As the LHP temperature increases, the strength of the hydrogen bonding between the MA^+ cation and the X^- anions diminishes, although there is still significant coupling in the high-temperature cubic phase[59,64,65]. This coupling is shown in **Figure 2.3**, as shown by a molecular dynamics simulation by Mattoni et al. **Figure 2.3A** shows the a-b plane of orthorhombic MAPbI3. **Figure 2.3B** shows the azimuthal angle, ϕ, which indicates rotation in the a-b plane. **Figure 2.3C** shows the polar angle, θ, which is defined as the angle against the c crystallographic axis. **Figure 2.3D** describes the distribution of orientations of the C-N bond of MA^+ as a function of temperature across the cubic to tetragonal phase transition at 330 K and the tetragonal to orthogonal phase transition at 180 K[36]. At 100 K, the disorder of the MA^+ is restricted to two antiparallel, planar alignments. As the temperature increases, the thermal fluctuations of MA^+ also increase, resulting in a broader range of fluctuations. In the tetragonal and cubic phases, regions of higher density indicate that the rotation of the MA^+ cation is not entirely free, but is less strongly coupled to the inorganic lattice[64].

A-site cations also experience dynamic disorder from "rattling" translational motion inside the PbX_6^{4-} cage[66–68]. This bears resemblance to the rattling behavior of guest ions in other cage structures, including thermoelectric materials such as clathrates and skutterudite.[68–70]. Yaffe et al report low-frequency Raman measurements that suggest the anharmonicity of $CsPbBr_3$ in the tetragonal and cubic

phases is partially due to the rattling of the Cs^+ cation[66]. Here, the trapped A^+ cation inelastically scatters acoustic phonons, which results in short phonon lifetimes. The observed short phonon lifetimes associated with the A-site cation[60,71] underpin the ultralow thermal conductivity of LHPs[72–76]. The low thermal conductivity establishes LHPs as promising thermoelectrics[69] and partially contributes to observed slow cooling of hot carriers in LHPs[76,77].

2.3 Disorder-Induced Polar Nano Domains in the Lead Halide Lattice

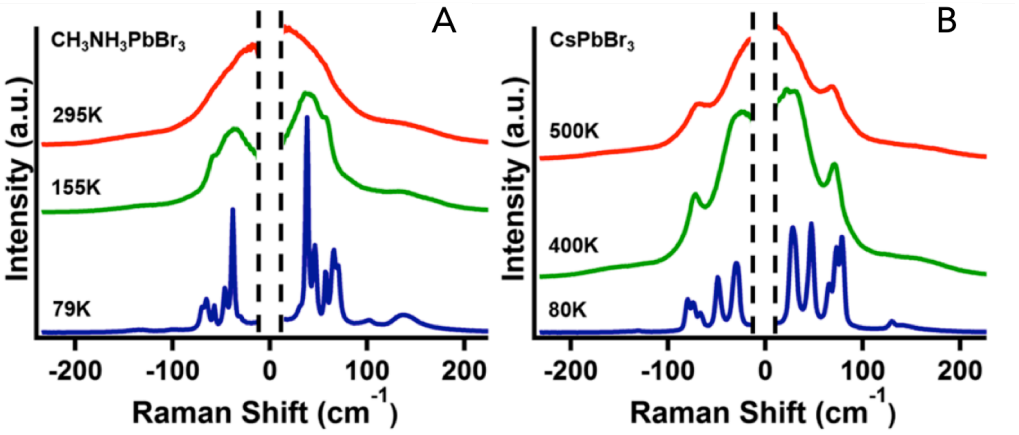

Figure 2.4 Low-frequency Raman spectra of MAPbBr3 (A) and CsPbBr3 (B). The orthorhombic, tetragonal, and cubic phases are indicated by blue, green, and red, respectively. In the orthorhombic phase, the phonon modes are sharp and well-resolved. At higher-temperature phases, the structure becomes more diffuse and a clear central peak emerges, suggesting dynamic disorder from the lead bromide sublattice. Reprinted with permission from ref. [66]. Copyright 2017 by the American Physical Society.

The dynamic disorder of the lead halide lattice is also well-established, and is the dominant contribution to low-frequency phonon modes that couple with charge carriers. Low-frequency Raman measurements of single-crystalline $MAPbBr_3$ and

$CsPbBr_3$ demonstrate that in the low-temperature orthorhombic phase, the phonon modes are well-resolved in both $MAPbBr_3$ and $CsPbBr_3$. At the higher-temperature tetragonal and cubic phases, the phonon modes become more diffuse and a central peak emerges in the Raman spectra of both $MAPbBr_3$ and $CsPbBr_3$, as shown in **Figure 2.4**. This common broad central peak suggests that the high-temperature phases are dynamically disordered and that the local structure of the lead halide sublattice, experiences polar fluctuations that deviate from the overall cubic structure[66,78,79].

X-ray diffraction measurements of single-crystalline $MAPbI_3$ find that phonon modes at the M and R points, which correspond to antisymmetric and coordinated octahedral tilts, are highly anharmonic[80,81]. The observed rotational instabilities of the octahedra allow minimization of the lattice energy via optimized packing; these rotational instabilities are stabilized by the A-site cation[82,83]. These modes are associated with the macroscopic phase transitions[60,62,84], and the evident rotational instability indicates that the lead iodide lattice fluctuations can be described as local transitions between low-symmetry phases. The Pb^{2+} and MA^+ cations are off-centered relative to the ideal cubic structure, meaning that these structural fluctuations are spontaneously polarized low-symmetry regions[85,86]. Pair-distribution function analysis estimates that the size of these coordinated distortions is 1 – 3 nm[80].

These regions of spontaneous polarized distortions are reminiscent of emphanisis in PbS, PbSe, PbTe, and SnTe, which refers to the emergence of dipolar states from non-polar ground states[46,47,87–89]. Emphanisis is associated with the stereochemical activity of the s^2 lone pair of Pb^{2+}, which causes local symmetry

breaking. Emphanitic anharmonicity has been observed in $CsSnBr_3$ and, to a lesser degree, $CsPbBr_3$[85]. The LHP family also shares behavior with known emphanitic materials, namely the increase of the electronic band gap with increasing temperature, which is the opposite trend observed in most semiconductors[42,46,90].

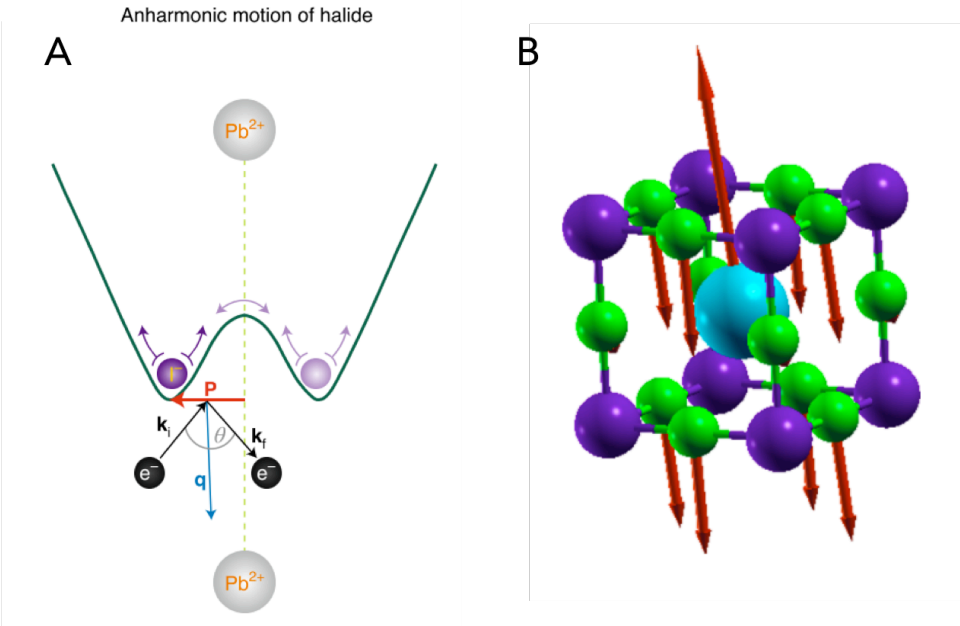

Figure 2.5 Anharmonic double-well potential and corresponding phonon modes. A An anharmonic double-well potential (green) of $MAPbI_3$ representing the reorientations of I^- (purple) around its equilibrium position on the Pb^{2+}-Pb^{2+} axis (gray). The offset is described by the electric dipole P and the change in wavevector, **q**, which is the quantity $\mathbf{k_f - k_i}$. Reprinted with permission from Katan et al: Springer Nature Materials, ref. [93], copyright 2018. **B** Polar phonon mode at the Γ point in cubic and orthorhombic $CsPbI_3$ induced by the antiparallel displacements of Cs^+ and I^-. This mode also has an anharmonic double well potential. Reprinted with permission from ref. [91]. Copyright 2017 American Chemical Society.

Various simulations demonstrate that these M and R point instabilities fit an anharmonic double-well potential, in which the potential minima are the broken-symmetry polarized structures and the saddle-point is the symmetric cubic structure[60,76,83]. An anharmonic double-well potential and the corresponding motion of the lead halide lattice are shown by Katan et al in **Figure 2.5A**[91]. The double-well

shape reflects the contribution of the fourth-order anharmonicity[92]. The double-well potential (green) shows an off-centering of the I^- anion (purple) from its equilibrium position along the Pb^{2+}-Pb^{2+} axis (gray dashed line). The I^- anion finds its energetic minima along an axis perpendicular to that of the Pb^{2+}-Pb^{2+} axis. The offset from the Pb^{2+}-Pb^{2+} axis can be described by the electric dipole **P** and the change in wavevector, **q**, which is $\mathbf{k_f} - \mathbf{k_i}$[91].

Marronnier et al also report a double-well phonon instability at the Γ point of orthorhombic and cubic $CsPbI_3$. This phonon mode emerges from the polar displacement of Cs^+ cations in one direction and I^- anions in the other **Figure 2.5**. Such Brillouin Zone (BZ) center instabilities are reminiscent of anharmonic double-well potentials in established ferroelectric materials, notably the titanium oxide perovskites[92,93]. In $BaTiO_3$ and $PbTiO_3$, the zone-center instabilities associated with ferroelectric behavior are polar displacements of the A-site and B-site cations relative to the O^{2-} anions[92]. We can similarly reinterpret the fluctuating PNDs of LHPs as nanoscale, transient ferroelectric domains.

The dynamic symmetry breaking of LHPs is conducive towards the Rashba-Dresselhaus effect in LHPs, in which the electronic bands are spin-split due to spin orbit coupling and dynamic symmetry breaking[94,95]. Due to the strong spin orbit coupling effects of heavy atoms, the splittings of the CBM and VBM are unequal, effectively separating electrons and holes in momentum space. The dynamic Rashba effect has been suggested as the mechanistic source of the optoelectronic properties of LHPs, including long charge carrier lifetimes, long carrier diffusion lengths, and low electron-hole recombination rates[96–100]. Notably, this mechanism does not account for the observed mobilities in LHPs[25,26,28].

2.4 Frequency-Dependent Dielectric Screening

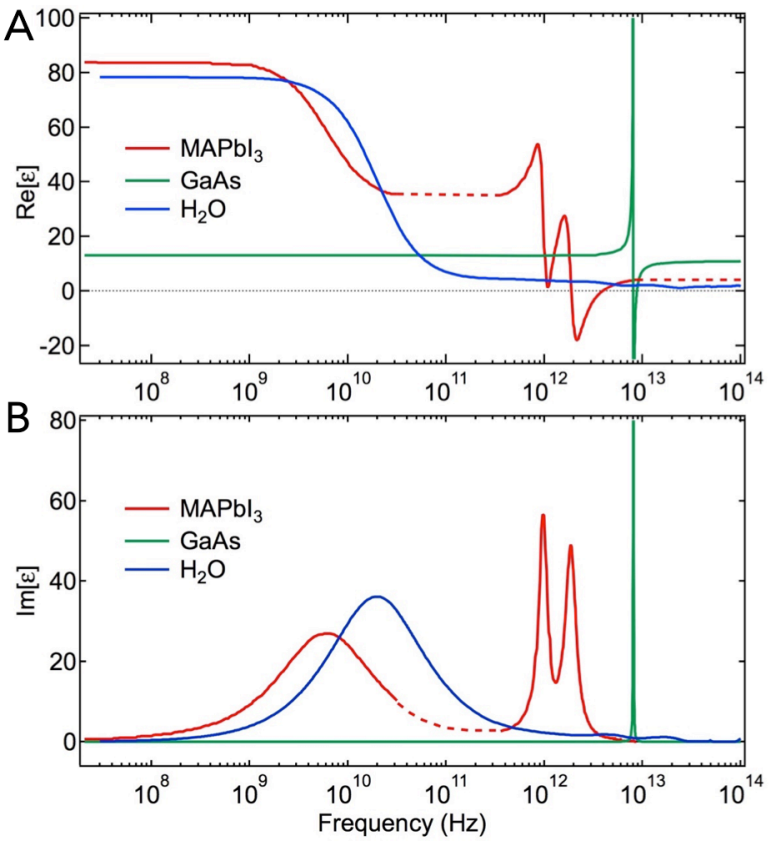

Figure 2.6 Frequency-dependent dielectric functions. A The real part of ε, $Re(\varepsilon)$ and **B** the imaginary part of ε, $Im(\varepsilon)$ for $MAPbI_3$ (red), GaAs (green), and H_2O (blue). Adapted with permission, ref. [104], published by The Royal Society of Chemistry; ref. [105], Copyright 2017 Wiley; ref. [106], Copyright 1975 Univ. of Missouri – Kansas City; ref. [107], Copyright 1998 Academic Press.

The dielectric permittivity describes a material's ability to screen an external electric field or, in other words, its polarization response to an electric field. The frequency-dependent complex dielectric function is given by

$$\varepsilon(\nu) = \varepsilon_1(\nu) + i\varepsilon_2(\nu), \tag{2.4.1}$$

where ε_1 describes the polarization, ε_2 describes the absorption, and ν is the frequency of the applied electric field. ε_1 is also commonly written as $Re(\varepsilon)$, and ε_2

is commonly $Im(\varepsilon)$. The physical phenomena that contribute the dielectric response vary depending on the frequency of the applied electric field[101]. The electronic response occurs at 10^{14} Hz and refers to the displacement of the electron cloud from the nucleus. The ionic response, which is attributed to polar optical phonons, dominates at 10^{11}-10^{13} Hz. The dipolar response occurs in the 10^{5}-10^{9} Hz range and manifests when dipolar molecules rotate according to the applied electric field[101,102].

The real part of the dielectric function, $Re(\varepsilon)$, of $MAPbI_3$ is shown as the red trace in **Figure 2.6A**. When the applied electric field exceeds 10^{13} Hz (10 THz), the high frequency dielectric constant, ε_∞, is approximately 4. $Re(\varepsilon)$ increases by an order of magnitude to ~36 across the broad transverse optical (TO) phonon resonances in the 10^{12} Hz (THz) region. The optical phonon modes in this region are associated with lead halide lattice[103]. I will refer to this value as $\varepsilon_{optic} + \varepsilon_{ionic}$. This onset of dielectric screening in the THz region occurs in other LHPs, notably $MAPbBr_3$ and $CsPbBr_3$, demonstrating that this behavior is not dependent on the A-site cation[34,49,67]. This increase in the dielectric function is followed by a second increase in $Re(\varepsilon)$ of $MAPbI_3$ at 10^{10} Hz (**Figure 2.6A**) and a broad peak in $Im(\varepsilon)$ (**Figure 2.6B**)[104]. This broad feature results from the liquid-like Debye reorientation of MA^+, which is similar to the Debye reorientation of H_2O. The dielectric function of H_2O is shown in blue for comparison[105].

The majority of this discussion will focus on the THz (10^{12} Hz) region, which is the relevant frequency regime for carrier-phonon interactions. The dielectric function of GaAs, which is also a polar semiconductor, is shown in green[106]. Here, we observe a smaller step size in $Re(\varepsilon)$ by ~18% (11 to 13) across a single sharp TO

phonon resonance[107]. In GaAs, $\frac{\Delta\nu_{TO}}{\nu_{TO}}$ is 0.009 where $\Delta\nu_{TO}$ is the full-width at half-maximum of the TO resonance. In comparison, $\frac{\Delta\nu_{TO}}{\nu_{TO}}$ for the two TO resonances in $MAPbI_3$ is 0.2 - 0.3[34].

The corresponding $Im(\varepsilon)$ are shown in **Figure 2.6B**. The LO phonon resonances near 10^{12} Hz in $MAPbI_3$ are similarly broad in comparison to that of GaAs. The width of the LO phonon peaks can be described by a damping factor, Γ. GaAs is a relatively harmonic material, and comparing Γ_{MAPbI_3} and Γ_{GaAs} reflects the aforementioned strong anharmonicity of $MAPbI_3$. In the Lorentz model, which is a simplified lossless harmonic oscillator model, the dielectric function can be related to Γ by

$$\varepsilon = 1 + \frac{Ne^2}{\varepsilon_0 m} \cdot \frac{1}{\omega_1^2 - \omega^2 - i\Gamma\omega} \tag{2.4.2}$$

where N is the lattice atoms per unit volume, e is the elementary charge, m is the mass of the electron, ε_0 is the vacuum permittivity, ω_1 is the shifted resonant frequency of the harmonic oscillator[108].

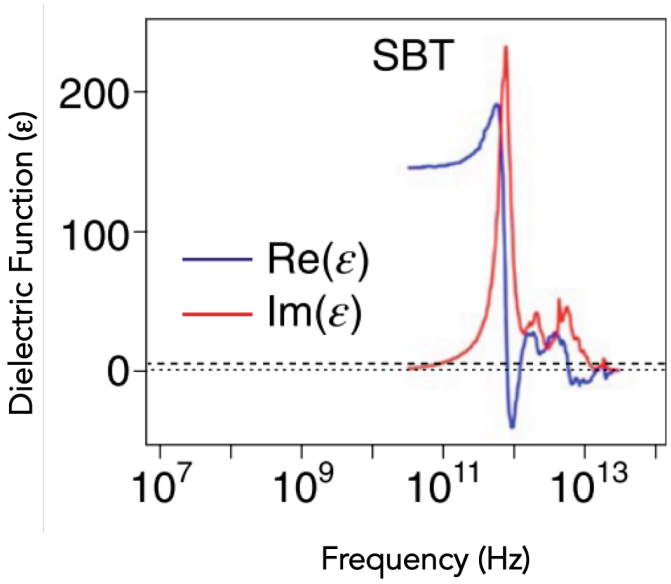

Figure 2.7 Dielectric Function of $SrBi_2Ta_2O_9$ (SBT). $Re(\varepsilon)$ and $Im(\varepsilon)$ are shown in red and blue respectively. Adapted from ref. [111], with the permission of AIP publishing.

The size of the step between ε_∞ and $\varepsilon_{optic} + \varepsilon_{ionic}$ is due to the enhancement of the Born effective charge and spontaneous lattice polarization[85,109,110]. Notably, this step across the TO phonon resonance is reminiscent of that in ferroelectric materials. **Figure 2.7** shows the frequency-dependent dielectric function of $SrBiTa_2O_9$. (SBT)[34,111]. Similarly, we see a large step across the TO phonon resonance and an broad, anharmonic LO phonon resonance[34,111]. This similarity motivates comparisons of PNDs in LHPs to known ferroelectric materials.

2.5 Large Polarons in Lead Halide Perovskites

Polarons are quasiparticles resulting from a charge carrier that polarizes the surrounding lattice and induces the displacement of surrounding atoms or "phonon cloud." This induced displacement from the equilibrium positions changes the

potential well of the charge carrier[29,31]. The most basic polaron model, the Fröhlich model, is predicated on the assumption that the displaced atoms behave as harmonic oscillators[29]. On an intuitive level, this can be described as the solid-state analogue to solvation in liquids. A polaron can be small or large depending on whether the short-range or long-range electron-phonon interaction dominates. This competition determines whether the polaron's coherence length, L_{coh}, extends beyond a single unit cell with length a. The short-range electron-phonon interaction is the deformation potential. The long-range electron-phonon interaction is the Coulomb potential arising from the interaction of the charge carrier and the induced atomic displacements[31]. The long-range potential well determines the long-range electron-phonon interaction and is represented by

$$V_{eq}^{LR}(\boldsymbol{r}) = -\left(\frac{1}{\varepsilon_\infty} - \frac{1}{\varepsilon_s}\right)\frac{e^2}{|\boldsymbol{r}|} \tag{2.5.1}$$

where $\boldsymbol{r}$ is the position of the charge carrier. Inspection of equation (2.5.1) shows that the magnitude of the long-range electron-phonon interaction depends on the term, $\frac{1}{\varepsilon_\infty} - \frac{1}{\varepsilon_s}$, which effectively means the long-range electron-phonon interaction depends on the nuclear contribution to the material's overall polarizability. In covalent semiconductors such as GaAs, where the difference between ε_∞ and ε_0 is small, $V_{eq}^{LR}(\boldsymbol{r})$ is negligible. However, in LHPs and ferroelectric materials, which are highly polarizable, the condition $\varepsilon_s \gg \varepsilon_\infty$ means that the long-range electron-phonon interaction is exceptionally strong[31]. Because of their consistency with the optoelectronic and transport properties of LHPs, I will restrict the remainder of this discussion to large polarons[25,112].

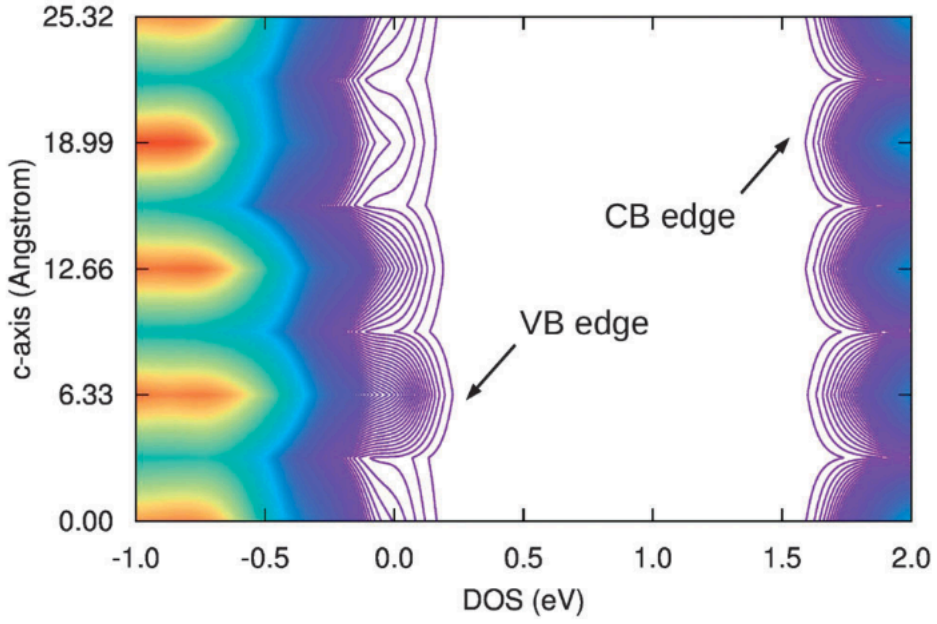

Figure 2.8 Spatial localization of the conduction band and valence band edges of $MAPbI_3$. Reprinted with permission from ref. [115], published by the Royal Society of Chemistry.

The large polaron inhibits Coulomb-mediated interactions between the carrier and charged defects, polar optical phonons, and other charge carriers[31,112]. For carrier densities, ρ below the Mott transition, ρ_{Mott}, which is ~10^{-18} cm^{-3} [113]. Coulomb screening by the large polaron provides a compelling explanation for the unique optoelectronic properties of LHPs. The ensuing charge localization spatially separates the electron and hole charge densities[114,115]. **Figure 2.8** shows the dynamic spatial localization of the VBM and CBM from molecular dynamics simulations. These spatial separations fluctuate on the sub-ps scale[115]. Furthermore, when large polarons approach each other, their respective ionic displacements destructively interfere, providing a repulsive force that demonstrably inhibits carrier recombination[13,33].

In addition to spatial localization, the large polaron also inhibits Coulomb-mediated interactions between the self-trapped charge and charged defects, polar optical phonons, and other charge carriers[28]. Four-wave mixing demonstrates that the Coulomb interaction in LHPs is significantly weaker than in GaAs[116]. The effective mass, and therefore momentum, of the large polaron is relatively large compared to that of an unscreened charge carrier. Scattering with LO phonons, which have relatively small momenta, has minimal effect on the trajectory of the large polaron. Intuitively, this can be described by a bowling ball (large polaron) colliding with ping-pong balls (LO phonons); the trajectory of the bowling ball (large polaron) is minimally disturbed. This momentum mismatch prevents trapping and charge carrier and therefore contributes to the long carrier lifetimes, long carrier diffusion lengths, and efficient radiative recombination[12,15,19,25,117,118].

In addition, the screening of the Coulomb potential facilitates the presence of long-lived hot electrons in LHPs. a conventional intrinsic semiconductor with parabolic bands, hot carriers cool by emitting LO phonons. This carrier-LO phonon scattering process is referred to as Fröhlich scattering[29]. Once the carrier has cooled to within an LO phonon's energy of the CBM, the remaining energy is dissipated by scattering with acoustic phonons[119,120]. Because the large polaron suppresses the Coulomb interaction of the carrier, the aforementioned Fröhlich scattering is also suppressed. Niesner et al observed the ~300 fs relaxation of photoexcited carriers to two populations: a band-edge population at the CBM (E^o) and a hot population (E^*) ~300 meV above the CBM, as shown in **Figure 2.9** [21]. This relaxation time is interpreted as the formation time of the large polaron and is corroborated by time-resolved multi-THz spectroscopy (TRTS), transient reflectance, and time-resolved

optical Kerr effect spectroscopy (TR-OKE) measurements[35,49]. The hot carriers have a lifetime of ~100 ps, which is observed by TR-2PPE, time-resolved photoluminescence (TRPL), and transient absorption (TA) spectroscopy and microscopy[18,20–22]. The rate of E^* depopulation and E^o repopulation are very similar, suggesting that the hot carriers relaxation is not trap-mediated[18,21]. It is important to note that this discussion holds for the condition that the charge density $\rho < \rho_{Mott}$. Slow hot carrier cooling has also been observed at high carrier densities when $\rho > \rho_{Mott}$[23,121]. In this regime, hot carriers exist as plasmas, and cooling is inhibited by a phonon bottleneck, poor thermal conductivity, and Auger recombination[23,24,76,121–123]. The slow cooling of hot polarons in the low charge density limit is treated with more detail in ref. [77].

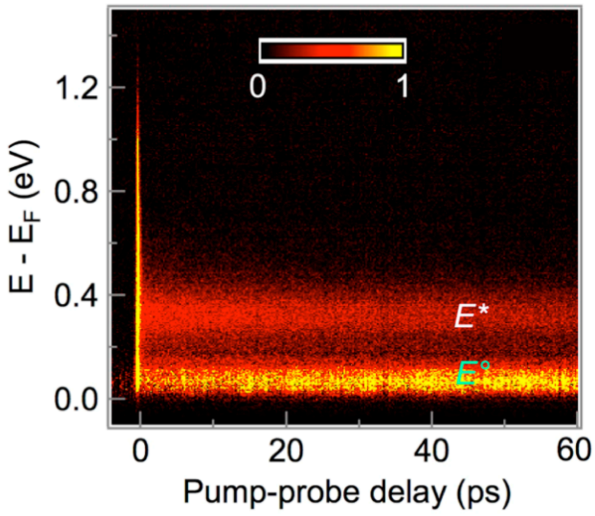

Figure 2.9 Time-resolved two photon photoemission (TR-2PPE) of polycrystalline $MAPbI_3$ thin films. Charge carriers are excited and then photoionized with variable time delay. The charge carriers relax in ~300 fs to two distinct populations, E^o and E^*, which are band-edge carriers and hot carriers, respectively. E^* has a lifetime of ~100 ps. Reprinted with permission from ref. [21]. Copyright 2016 American Chemical Society.

The transport properties observed in LHPs are also consistent with large polaron protection. A small polaron, where $L_{coh} < a$, is distinguished by phonon-assisted "hopping" transport, where the mobility increases with increasing temperature ($\frac{d\mu}{dT} > 0$). In contrast, a large polaron, where $L_{coh} > a$, demonstrates coherent band-like transport, where the mobility decreases with increasing temperature ($\frac{d\mu}{dT} < 0$)[31]. LHPs exhibit band-like transport, where the mobility μ decreases with increasing temperature, *T*. The charge carrier mobilities are relatively modest, typically 20 – 200 $cm^2/V \cdot s$[25,42,124–126], which is significantly lower than mobilities in conventional semiconductors such as Si[127]. The experimentally observed temperature dependence is approximately $\mu \sim T^{-3/2}$, suggesting that carrier-scattering is dominated by acoustic phonons[25,26,42]. Indeed, the appropriate temperature dependence relation is recovered when assuming that large polarons scatter primarily with acoustic phonons[128].

2.6 Lead Halide Sublattice Contributions to the Large Polaron

Although the dynamic disorder of organic A-site cation MA^+ and FA^+ has been suggested to contribute to charge carrier localization and screening[61,104,114,115,129,130], numerous experiments evince that the PbX_6^{4-} phonon modes dominantly couple to the charge carrier. Bretschneider et al find similar rise times in THz photoconductivity measurements of $MAPbI_3$, $FAPbI_3$, and $CsPbI_3$, suggesting that polaron formation in these materials is driven by the response of the photoexcited PbI_6^{4-} sublattice[131]. Similarly, a time-resolved photoluminescence (TRPL) comparison of the bromide analogues, $MAPbBr_3$, $FAPbBr_3$, and $CsPbBr_3$ measurements

demonstrates similar charge carrier trapping and recombination rates[132]. These similar behaviors are due to the similar dynamic disorder contributions of the common PbX_6^{4-} sublattice.

As previously discussed, the low-frequency Raman experiments of Yaffe et al demonstrate that both $MAPbBr_3$ and $CsPbBr_3$ exhibit anharmonic behavior, which indicates that this dynamic disorder comes from the PbX_6^{4-} sublattice[66]. The Stokes shifts in $CsPbBr_3$ and $MAPbBr_3$ are attributed to a solvation-like response by an effective LO mode of the lead halide sublattice at 4.75 THz[133].

Our time-resolved optical Kerr effect spectroscopy (TR-OKE) measurements in Chapter 4[49] and coherent phonon spectroscopy (CPS) measurements described in Chapters 5 and 6 find rich PbX_6^{4-} phonon activity associated with the electronic transition. Photoexcitation has been shown to couple to a number of phonon modes of the PbX_6^{4-} octahedra, including a 0.9 THz Pb-I-Pb bending mode[134], volume-preserving rotational distortions[135], and the elongation of Pb-X bonds[136]. The light-induced Pb-X bond elongation is consistent with observations of photostriction in $MAPbI_3$[137,138]. Lan et al use time-resolved multi-THz spectroscopy and identify a 3.7 THz effect LO phonon in single-crystalline $MAPbI_3$[35].

2.7 Ferroelectric Large Polaron Hypothesis

Having established both the strong anharmonicity of LHPs, the application of the Fröhlich large polaron model is clearly incongruous. A model predicated on harmonic oscillators and the linear carrier-phonon coupling regime cannot adequately describe carrier-lattice coupling in such anharmonic materials. Here, we

consider the combined evidence of fluctuating PNDs and the ferroelectric-like dielectric response and its ramifications on the large polaron picture. Miyata and Zhu propose that these local ferroelectric domains additionally screen charge carriers in a non-linear way. The double-well potential in LHPs is along a polar lattice mode that drives fluctuations between symmetry broken phases[34,60,77,91]. This double-well lattice potential is analogous to the double-well potential in ferroelectric materials[34,139]. This proposal is somewhat related to the superparaelectric polaron used to describe photoenhanced conductivity in STO[140,141]. **Figure 2.10A** shows the harmonic potential of the Fröhlich large polaron. The polarization response to the electric field is linear (**Figure 2.10B**), and the strength of the long-range electron-phonon interaction diminishes as a function of $\frac{1}{r}$. In LHPs, the electric field of the charge either polarizes the surrounding lattice, causing ordered polar displacements, or the charge preferentially localizes to the boundaries of ordered PNDs. Indeed, this explanation is consistent with the observation that charge localization is more pronounced at higher temperatures, where polar fluctuations are favored[142].

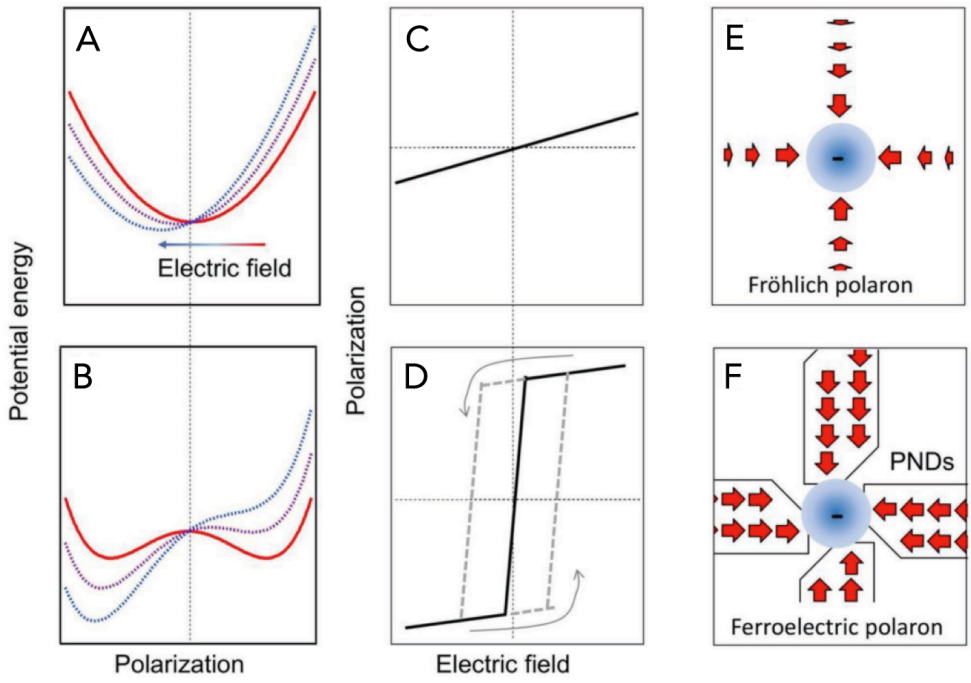

Figure 2.10 Fröhlich Large Polaron versus Ferroelectric Large Polaron. A, C, E, Harmonic potential, polarization response to electric field, and dipole moment in a Fröhlich large polaron. **B, D, F,** Anharmonic double well potential, polarization response to electric field, and dipole moment in ferroelectric large polaron. Reprinted with permission from ref. [77], Copyright 2019 Wiley; ref. [34], Copyright 2018 Springer Nature[34].

We can consider the ferroelectric large polaron as a local, transient ferroelectric phase transition that is related to the "hidden ferroelectric phase" recently observed in an oxide perovskite, $SrTiO_3$ (STO). A local symmetry breaking is observed using THz field-induced symmetry breaking (TFISH) and THz Kerr effect spectroscopy (TKE)[143]. With sufficiently THz high fields, TFISH and TKE responses demonstrate a phase transition to a ferroelectric phase. Notably, the authors observe the emergence of low-frequency phonons similar to our observations in Chapters 4 and 5. In the ferroelectric polaron model, the charge carrier, provides the transition-inducing field rather than the THz pulse.

3 Optical Methods

Sections 3.4 and 3.5 are adapted with permission from:

Maehrlein, S. F.*; **Joshi, P. P.***; Wang, F.; Juraschek, D. M.; Cherasse, M.; Zhu, X.-Y. Spectroscopic Signatures for Ferroelectric Charge Localization in Lead Halide Perovskites. *Submitted.*

*indicates equal author contribution

Abstract

The objective of this thesis is to understand the structural mechanisms that contribute to dynamic screening of charge carriers in lead halide perovskites (LHPs). Doing so requires the ability to probe the structural dynamics of LHPs on sub-picosecond timescales. Ultrafast pump-probe spectroscopies exploit the speed of light in order to achieve the necessary time resolution. A pump pulse excites the sample and a variably delayed probe pulse tracks the lifetime of the pump-induced change. Finely changing the relative path lengths of the pump and probe pulses changes the relative delay between the pulses.

Here, I outline the basic working principles of the laser system that supports this work and describe the specific techniques used here. To investigate LHPs' ultrafast structural dynamics, we track the transient polarization anisotropy created by a visible pump pulse using coherent phonon spectroscopy (CPS) and Fourier-transform coherent phonon spectroscopy (FT-CPS). CPS is a one-dimensional technique that is closely related to time-resolved optical Kerr effect spectroscopy (TR-OKE)[49]. In our CPS measurements, we modified the laser amplifier system and implemented a single-shot balanced detection scheme, which gives a higher signal-to-

noise ratio than optical heterodyne detection (OHD) used in previously published TR-OKE measurements[49]. For the sake of comparison, I describe the amplifier modifications and both detection schemes here. FT-CPS is a two-dimensional technique that resolves pump-wavelength dependent structural dynamics.

3.1 Regenerative Amplifier System

The majority of these measurements were supported by a Ti:sapphire single-pass regenerative amplifier system (modified KM Labs Wyvern, 10 kHz, 800 nm, 45 fs, 0.7 mJ/pulse). The amplifier is seeded by a broadband pulse from a Kerr-lens mode-locked oscillator (modified KM Labs Griffin, 80 MHz, <12 fs), which is pumped by a 532 nm CW laser (Spectra Physics Millenia, 5W). The low-energy seed pulse from the oscillator is amplified using chirped pulse amplification (CPA), in which the seed is temporally and spectrally stretched using a grating pair in order to decrease its peak power by 3-4 orders of magnitude. The seed is then passed through a single-stage regenerative amplifier. The amplifier is gated by a thin-film polarizer, quarter waveplate, and Pockels cell. When a voltage is applied across the electrooptic crystal in the Pockels cell, the Pockels cell behaves as a half waveplate, rotating the seed's polarization by 90° and trapping the seed pulse inside the amplifier cavity. The seed pulse is then amplified via stimulated emission in a Ti:Sapphire crystal by a Q-switched 532 nm laser (Northrop Grumman Patara, 10 kHz, 100 W). When the voltage is removed from the Pockels cell, the amplified pulse is ejected and then compressed by a grating pair to ~45 fs. The duration of the voltage applied to the Pockels cell determines the number of passes the seed makes through the gain medium[144–146].

The Pockels cell and Q-switched pump laser are driven at 10 kHz by a delay generator (Stanford Research Systems) that is triggered by the frequency-divided output of the oscillator from a fast photodiode inside the oscillator (80 MHz) that is passed through two frequency dividers (8 and 1000). Empirically, this modification improves the power stability and pulse duration stability of the final pulse.

3.2 Non-Collinear Optical Parametric Amplification (NOPA)

The tunable visible pump pulse is provided by a homebuilt non-collinear optical parametric amplifier (NOPA), in which a high-intensity pump pulse with frequency ω_p amplifies a lower-intensity signal pulse with frequency ω_s, where $\omega_p > \omega_s$. A third pulse, the idler, is also generated in accordance with conservation of momentum (or phase-matching condition):

$$\hbar\vec{k}_p = \hbar\vec{k}_s + \hbar\vec{k}_i \tag{3.2.1}$$

$\vec{k}_p$, $\vec{k}_s$, and $\vec{k}_i$ are the wave vectors of the pump, signal, and the idler, respectively[147].

The transfer of intensity from pump to signal is accomplished by spatially and temporally overlapping the pump and signal pulses in a birefringent crystal, typically beta barium borate (BBO). In this NOPA, we use type I phase-matching, in which the pump and the signal are perpendicularly polarized to each other.

The majority of a collimated fundamental of a Ti:Sapphire amplifier (800 nm, 45 fs, 10 kHz) is diverted towards the NOPA, and the remainder is used as a probing line, as shown in **Figure 3.1**. Inside the NOPA, the fundamental is split into a pump and seed line. In the pump line, the fundamental is doubled by a BBO with a cut angle optimized for second harmonic generation (SHG). In the seed line, a

broadband white light continuum is generated by focusing the fundamental into sapphire. Via the parametric amplification process, the pump amplifies a narrowband part of the white light continuum. The central wavelength of the amplified part is tuned by adjusting the relative temporal delay between pump and seed.

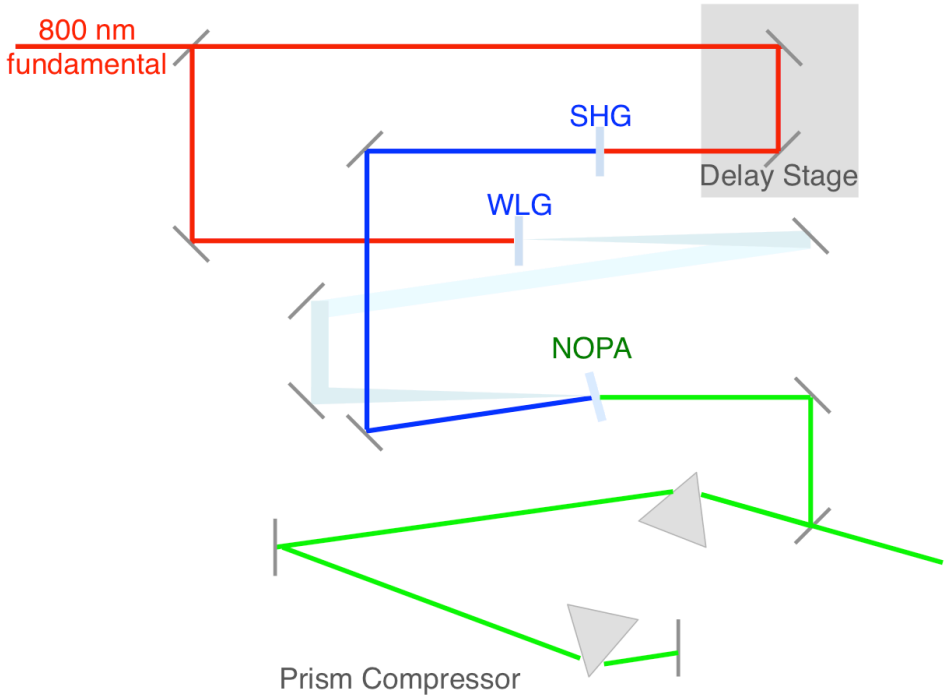

Figure 3.1 Schematic of a visible-range non-collinear optical parametric amplifier (NOPA). A white light seed is generated by focusing an 800 nm fundamental into an Al_2O_3 window. A 400 nm pump pulse is generated by doubling the fundamental with BBO. The pump and seed pulses are temporally and spatially overlapped on an appropriately cut BBO crystal that is oriented to satisfy the phase-matching conditions. The output is then directed into a prism compressor, yielding sub-30 fs pulses.

In this setup, the wavelength range of the signal ranges from 490 nm to 680 nm[148]. The efficiency of the NOPA process can be further modulated by adjusting the angles of the NOPA BBO in order to best satisfy the phase-matching condition. The amplified visible pulse is then compressed in a fused-silica prism compressor to sub-30 fs and characterized by frequency-resolved optical gating (FROG).

3.3 Time-Resolved Optical Kerr Effect Spectroscopy and Optical Heterodyne Detection

Time-resolved optical Kerr effect spectroscopy (TR-OKE) is an ultrafast pump-probe technique that is conventionally used to probe dynamics in liquids[149–153]. In time-resolved optical Kerr effect spectroscopy (TR-OKE), a linearly polarized visible pump pulse induces a transient birefringence in the sample, which is tracked with variable time delay by a narrow-band linearly polarized near-infrared (NIR) probe pulse. The 800 nm fundamental of the Ti:Sapphire amplifier is used as the probe pulse (**Figure 3.2**). The probe is mechanically chopped at 5 kHz and detected by a high-speed linear array detector. This detection scheme is compatible with transient absorption experiments, which require spectral resolution of the probe pulse.

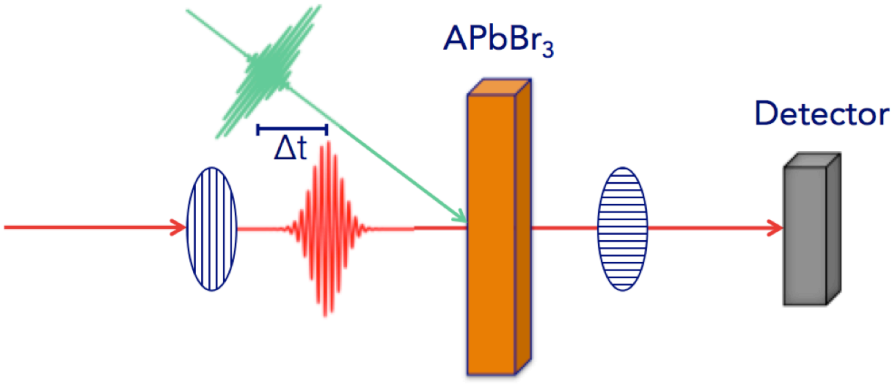

Figure 3.2 TR-OKE schematic. A linearly polarized pump pulse (green) induces a transient birefringence in the LHP sample. The transient birefringence is probed with a linearly pump probe pulse (red) with time delay Δt. The probe is cross-polarized after the sample, and the cross-polarization is slightly detuned to generate a local oscillator that coherently mixes with the Kerr signal. The resulting heterodyne is detected by a home-built spectrometer.

In the most general case, the excitation $Q(t)$ can be expressed as

$$Q(t) = \int_{-\infty}^{t} dt' \Phi_{ijkl}(t-t') E_k^*(t') E_l(t') \tag{3.3.1}$$

where $\Phi_{ijkl}(t-t')$ is the nonlinear optical polarization impulse response function and $E_k(t')$ and $E_l(t')$ are the electric fields from the optical pulses. We can use this representation as a general form to describe the transient birefringence is represented as

$$\Delta n(t) = \delta n(t)_{\parallel} - \delta n(t)_{\perp} = \int_{-\infty}^{t} dt' \Phi_{ijkl}^{Re}(t-t') I_{pump}(t') \tag{3.3.2}$$

where $\delta n(t)_{\parallel}$ and $\delta n(t)_{\perp}$ are the transient changes in the refractive index that are parallel and perpendicular to the pump polarization, $I_{pump}(t')$ is the intensity of the pump pulse, and $\Phi_{ijkl}^{Re}(t-t')$ is the real part of the nonlinear optical polarization impulse response function[152].

For the purposes of higher signal amplitude and signal-to-noise, we detect the heterodyne signal, in which the electric field of local oscillator, E_{LO}, coherently mixes with that of the signal, E_j. The heterodyne signal is generated by detuning the cross-polarization of the probe by $\pm 2^o$. The heterodyne signal is represented by

$$S(\tau) = \int_{-\infty}^{\infty} dt\, E_{LO}^*(t-\tau) E_j(t-\tau) Q(t) \tag{3.3.3}$$

where τ is the pump-probe delay time. The total signal at the detector is proportional to

$$I_{LO} + I_S + I_B + \frac{nc}{8\pi}(E_S^* E_{LO} + E_{LO}^* E_S) \tag{3.3.4}$$

where I_{LO} is the intensity of the local oscillator, I_S is the intensity of the homodyne Kerr signal, I_B is the intensity from any background radiation, E_S is electric field from the signal, and E_{LO} is the electric field from the local oscillator. The heterodyne term is $\frac{nc}{8\pi}(E_S^* E_{LO} + E_{LO}^* E_S)$. The heterodyne signal is advantaged over the

homodyne signal in multiple respects: higher signal amplitude, higher signal to noise, and linear scaling with the pump electric field[151,152,154,155].

3.4 Shot-to-Shot Balanced Detection

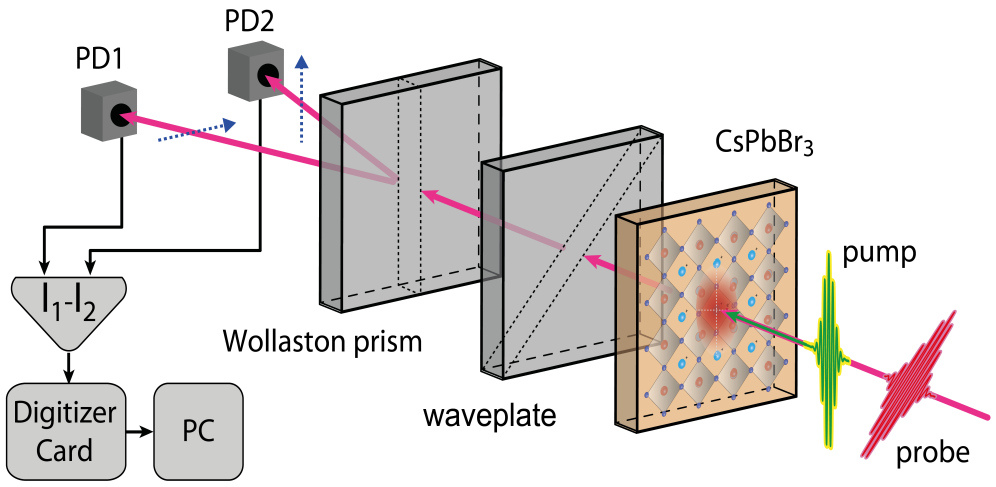

Figure 3.3 Shot-to-shot balanced detection. The sample is excited with a linearly polarized visible pump pulse (green) and probed with a linearly polarized near-IR probe pulse (red). The transmitted probe is passed through a waveplate and a Wollaston prism, which splits the probe into two components of perpendicular polarizations. A half- or quarter- waveplate tunes the linear polarization or ellipticity of the probe pulse prior to the Wollaston prism, allowing the probe polarization components to be "balanced" on Si-based photodiodes (PD1 and PD2). The difference between these two signals (I_1-I_2) is digitized and acquired at 10 kHz.

In these experiments, coherent phonons are excited by an ultrafast pump pulse with a time duration that is less than one half of the phonon period. The refractive index, n, is modulated by the first order Raman tensor, $\partial\chi/\partial Q$, and is probed by the transmittance, ΔT, as a function of delay time, Δt:

$$\Delta T = \frac{\partial T}{\partial n}\Delta n = \frac{\partial T}{\partial \chi}\frac{\partial \chi}{\partial Q}Q \tag{3.4.1}$$

where Q is the time-dependent coherent phonon amplitude[156,157].

The polarization anisotropy of the probe is detected via a balanced detection scheme[156]. The direct measurement of polarization anisotropy discriminates against isotropic polarization changes and transient absorption contributions, which allows for a higher signal-to-noise ratio than previous detection schemes which measure the change in intensity of a cross-polarized probe[20,49]. A sample transient is shown in **Figure 3.4**; CS_2 is used as a model system. In the experiments reported here, the signal-to-noise ratio of pump-induced polarization changes is 10^4:1.

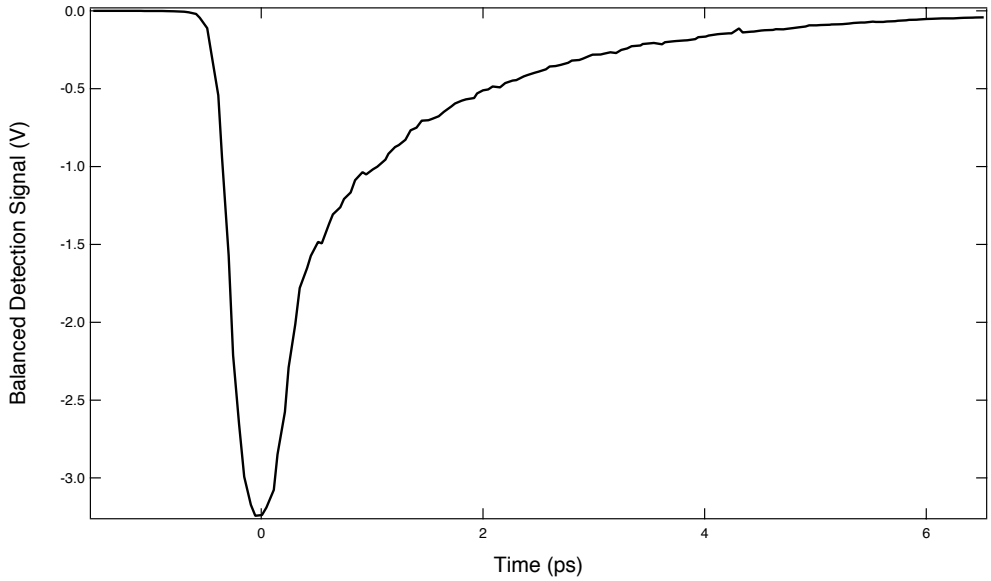

Figure 3.4 Pump-Probe Transient of CS_2 from Balanced Detection.

As shown in **Figure 3.3**, after transmission through the sample, the probe is passed through a broadband waveplate and a Wollaston prism. There are no additional optics between the sample and Wollaston prism to preserve polarization purity. The Wollaston prism spatially separates the probe into two different polarization components. Tuning the linear polarization or ellipticity of the probe with a half- or quarter-waveplate, respectively, controls the relative intensities of the two polarization components, specifically those parallel and perpendicular to the

pump pulse. Each polarization component is directed into a Si-based photodiode. The measured signal is the difference between the single-shot resolved photocurrents from each photodiode, $I_1 - I_2$. It is "balanced" by adjusting the waveplate prior to measurement such that the signals from the individual photodiodes are equal for the unexcited sample. The single shot difference signal ΔI is digitized and acquired at 10 kHz, allowing for single-shot detection of the difference signal.

3.5 Fourier Transform Coherent Phonon Spectroscopy

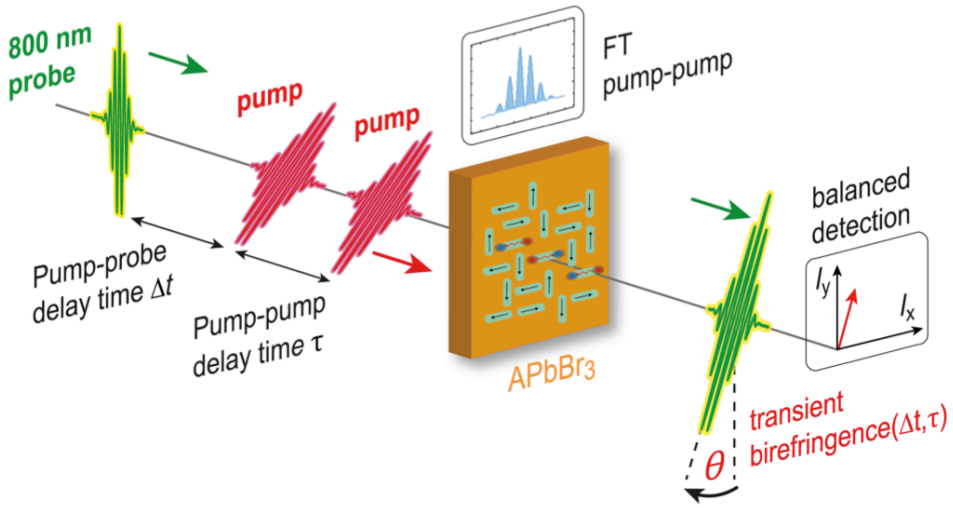

Figure 3.5 Fourier-transform coherent phonon spectra (FT-CPS) from $CsPbBr_3$ The experimental setup: the two coherent, co-propagating pump pulses created by pulse shaping and the time-delayed probe pulse measures the transient birefringence.

Electronic state specific Fourier transform coherent phonon spectroscopy (FT-CPS) requires a double pulse excitation scheme (**Figure 3.5**). To accomplish this, we generated double pulses from the NOPA output pulse by using an AOM based visible pulse shaper (PhaseTech QuickShape Visible)[158]. The phase shaper utilizes the

first order diffraction from an acoustic wave, which is used as a phase mask. The phase mask pattern was generated by an arbitrary waveform generator (AWG). The AWG output signal was synchronized to the arrival of the femtosecond laser pulse at the AOM. After each laser shot the next mask of a pre-defined mask sequence was send to the AOM. The phase of each spectral component in the pulse can be modified independently, thereby allowing the creation of double pulses with arbitrary carrier envelope phase. Compared to interferometer-based double pulse generation, the use of a pulse shaper exhibits several advantages[158].

First, compared to a mechanical delay stage the pump-pump delay τ can be controlled more precisely, without mechanical jitter, and much faster on a shot-to-shot basis. This enables a rapid scan approach to avoid laser drifts within one full pump-pump delay scan. Even with phase cycling, where every pump-pump delay step consists of 4 different AOM phase masks (see below), in our experiments, a typical pump-pump delay mask sequence of 904 sequences (226 delays) was acquired in 90.4 ms due to single shot detection. Within this time frame (<100 ms) thermal fluctuations of the NOPA and regenerative amplifier are negligible.

Second, the possibility of phase cycling is a unique advantage of using a pulse shaper. Due to the collinear propagation and parallel polarization of the two pump pulses E_1 and E_2, it is important to separate the higher order 2D signals resulting from a coherent interaction of E_1 and E_2 from linear signals (e.g. transient absorption or scattering caused be E_1 and E_2 separately)[3]. This was achieved by phase cycling, which is implemented by subtracting two signals $S(\tau, \Delta\phi = 0) - S(\tau, \Delta\phi = \pi)$ at the same pump-pump delay τ, where $\Delta\phi$ is the phase difference

between the to pump pulses. We used the following 4-sequence phase cycling scheme, which is common in 2D spectroscopy[3]:

$$\bar{S} = S(\phi_1 = 0, \phi_2 = 0) - S(\phi_1 = 0, \phi_2 = \pi) + S(\phi_1 = \pi, \phi_2 = \pi) - S(\phi_1 = \pi, \phi_2 = 0) \quad (3.5.1)$$

Additionally, we added a rotating frame with frequency ω_F by an additional phase factor $e^{-i\tau\omega_F}$, which reduced the number of sampling points and increased the frequency resolution in the frequency window of interest[158,159]. Both rotating frame and phase cycling was automatically implemented by the commercial phase shaper control software (PhaseTech QuickControl).

Importantly, we carefully excluded artifacts related to phase cycling and rotating frame by performing a single pulse excitation (1D) experiment for every FT-CPS data set (2D). In the single pulse excitation case, we use exactly the same optical path through the phase shaper to account for dispersion and divergence effects. The only difference is the AOM mask sequence, which is simply used as a 5 kHz chopper (masks "1" and "0"). No phase cycling or rotating frame is applied in this chopper mode. The 1D pump-probe delay $\Delta\tau$ is introduced by a conventional mechanical delay stage. The E_{ex}-integrated transient birefringence signal agrees with the single pulse excitation (1D OKE) signal (see **Figure 6.8B**, **C**; **Figure 6.6B**, **C**; **Figure 6.1C**).

4 Large Polaron Formation

Reproduced with permission from ref [49]:

Miyata, K.; Meggiolaro, D; Trinh, M. T.; **Joshi, P. P.**; Mosconi, E.; Jones, S. C.; De Angelis, F.; Zhu, X.-Y. Large Polarons in Lead Halide Perovskites. *Sci Adv.* 2017 **3**: e1701217

TR-OKE experiments were conducted by myself and Kiyoshi Miyata. Transient reflectance measurements were conducted by M. Tuan Trinh. LHP single crystals were synthesized by myself and Skyler Jones. DFT calculations were conducted by Daniele Meggiolaro and Edoardo Mosconi.

Abstract

Lead halide perovskites show remarkable defect-tolerance responsible for their excellent optoelectronic properties. These properties might be explained by the formation of large polarons, but how they are formed and whether organic cations are essential remain open questions. Here we provide a direct time-domain view of large polaron formation in single-crystal lead bromide perovskites: $CH_3NH_3PbBr_3$ and $CsPbBr_3$. We found large polaron forms predominantly from the deformation of the $PbBr_3^-$ frameworks, irrespective of the cation type. The difference lies in the polaron formation time, which in $CH_3NH_3PbBr_3$ (0.3 ps) is less than half of that in $CsPbBr_3$ (0.7 ps). First principles calculation confirms large polaron formation, identifies the Pb-Br-Pb deformation modes as responsible, and explains quantitatively the rate difference between $CH_3NH_3PbBr_3$ and $CsPbBr_3$. The findings reveal the general advantage of the soft $[PbX_6]^{4-}$ sub-lattice in charge carrier protection and suggest that there is likely no mechanistic limitations in using all inorganic or mixed cation lead halide perovskites to overcome instability problems and to tune the balance between charge carrier protection and mobility.

4.1 Introduction

The exceptional rise in research activities on hybrid organic-inorganic lead halide perovskites (HOIPs) is a direct result of their remarkable optoelectronic properties that resemble defect-free semiconductors, despite static and dynamic disorder[160–162]. Even with modest mobilities[14,15,25,163,164], they show long carrier lifetimes and diffusion lengths that are key to their successes in optoelectronic devices[11,165,166]. An HOIP crystal consists of a lead halide sub-lattice (PbX_3^-) which determines the band structure[115] and a disordered organic cation sub-lattice (A^+) which modulates the electronic properties[100,114,167–169]. This unique $APbX_3$ structure and associated dielectric responses[17,18] have led to the large polaron proposal[20,28] in which the dynamically screened Coulomb potential minimizes charge carrier scattering with defects, with other charges, and with longitudinal optical phonons. While this proposal may explain some of the carrier properties of HOIPs, there have been no direct observation or confirmation of (large) polaron formation. Whether A-site organic cations are essential[100,114,167,168,171] or not[132,172–174] also remains an open question. Here we provide a direct time-domain view of phonon dynamics in the $CH_3NH_3PbBr_3$ HOIP in comparison to its all-inorganic counterpart, $CsPbBr_3$, using time-resolved optical Kerr effect (TR-OKE) spectroscopy[151,153]. We show the dominance of coupling between $PbBr_3^-$ lattice motions to across bandgap electronic transitions in both perovskites, but different polaron formation time constants of 0.3 and 0.7 ps for $CH_3NH_3PbBr_3$ and $CsPbBr_3$, respectively.

4.2 Materials and Methods

We synthesized optically flat, single crystal $CH_3NH_3PbBr_3$ and $CsPbBr_3$ samples[14], with effective bandgaps of E_g = 2.28 eV and 2.35 eV, respectively (see Appendix for details). In TR-OKE, the electric field of a linearly polarized pump laser pulse creates transient anisotropy and the resulting birefringence is detected by the polarization rotation of a probe pulse, which allows us to measure the system's response in a wide time range (fs-ns). We implement heterodyne-detected TR-OKE using home-built two-color pump-probe systems (see Section 3.3 and 4.5.2 for details). The photon energy of the pump was tunable ($h\nu_1$ = 1.85 – 2.45 eV) and that of the probe was fixed ($h\nu_2$ = 1.55 or 1.65 eV).

4.3 Results and Discussion

We examine structural flexibility and dynamic disorder in $CH_3NH_3PbBr_3$ coupled to carriers by varying the pump photon energy from non-resonant (1.85 eV) to the pre-resonant (2.10 eV) regimes (**Figure 4.1A**). We see the broad and featureless nuclear response distinctively different from that of a typical solid, where impulsively stimulated Raman excitation should appear as oscillatory features[175], but is rather characteristic of liquids[151,153]. The absence of oscillatory features suggests that we detect predominantly over-damped phonon modes that can be attributed to strong anharmonicity and dynamic disorder[176,177]. As $h\nu_1$ moves closer (2.03→ 2.18 eV) to E_g, we find enhanced slow responses (≥ 1 ps). This is attributed to the resonant Raman mechanism where nuclear motions are coupled to electronic transitions[178]. As seen in Fourier spectra of the OKE transients (**Figure 4.1B**),

approaching the E_g resonance enhances low-frequency (< 100 cm^{-1}) motions corresponding to those of the $PbBr_3^-$ lattice[179], particularly the coupled Pb-Br stretching and Pb-Br-Pb bending motions, as shown by the calculated phonon spectrum at the top of **Figure 4.1B**.

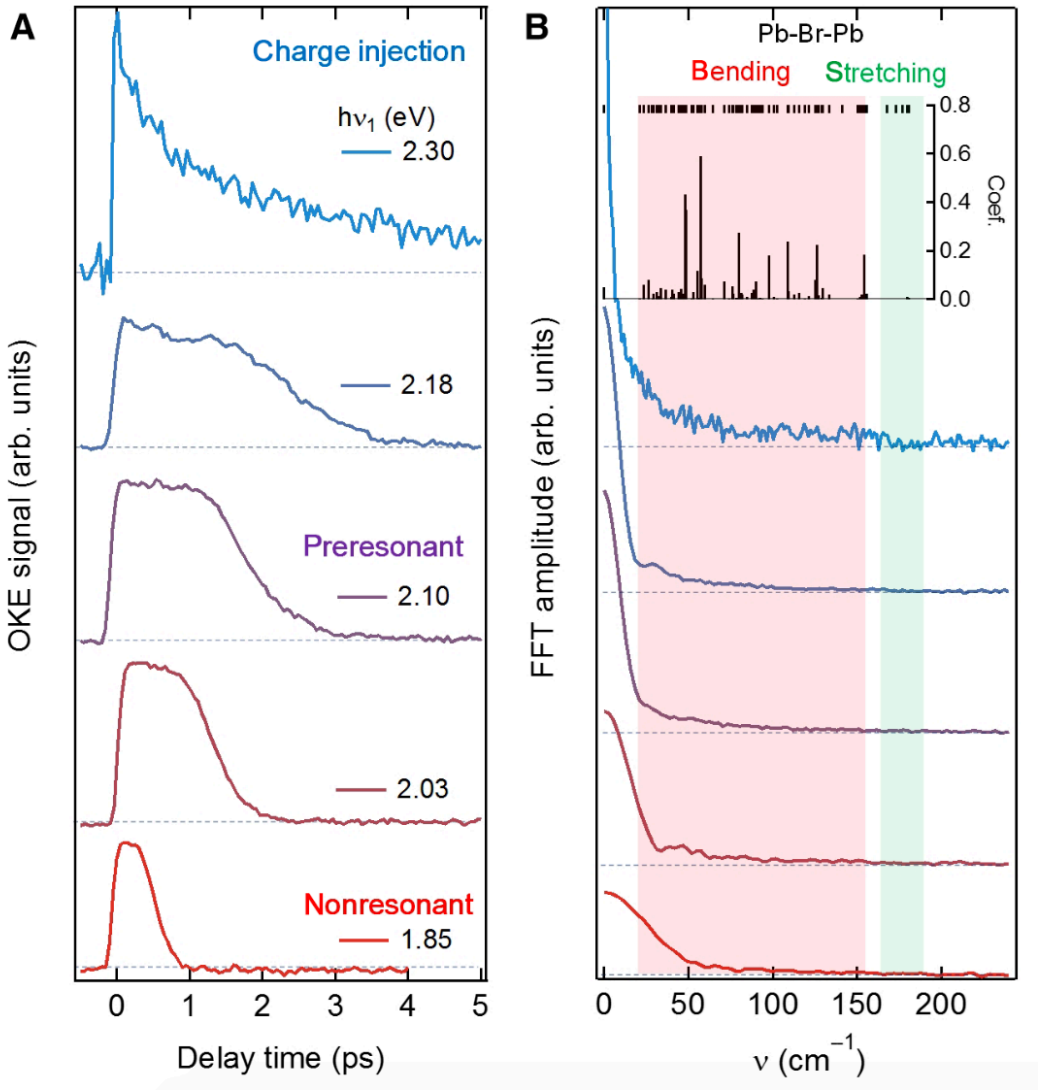

Figure 4.1 TR-OKE transients from a $CH_3NH_3PbBr_3$ crystal. A OKE transients from $CH_3NH_3PbBr_3$ as a function of pump energy (1.85 – 2.30 eV). As it moves from non-resonant to pre-resonant condition, contribution from low-frequency motions coupled to electronic excitation are enhanced. As it reaches to the carrier-injection regime, additional sub-ps dynamics manifests itself. **B** Fourier component of each OKE transient. The inset is the crystalline structure of $CH_3NH_3PbBr_3$. Black ticks at the top show calculated frequencies of normal modes and sticks represent projections of the displacement vector on the normal modes upon large polaron formation (see **Figure 4.8**). From ref. [49]. Reprinted with permission from AAAS.

By tuning $h\nu_1$ to 2.30 eV ($\geq E_g$) we directly probe the OKE response upon charge injection, topmost transient in **Figure 4.1A**. We observe qualitatively different structural dynamics: a sub-ps component with a time constant of τ_1 = 0.29 ± 0.04 ps and longer-lived anisotropy that decays with τ_2 = 3.4 ± 0.5 ps (see fitting in **Figure 4.3C** below). These features are absent in OKE transients for $h\nu_1 < E_g$ and are thus associated with the dynamic response of nuclei to the photo-injection of carriers, i.e. formation of (large) polarons. We show at the top of **Figure 4.1B** projections (sticks) of the displacement vector following a positive charge injection onto the calculated normal modes and find that a sub-set of stretching and bending modes of the inorganic sub-lattice is mainly responsible of such structural relaxation, as detailed later.

We compare the OKE responses in $CH_3NH_3PbBr_3$ with those in a fully inorganic $CsPbBr_3$ single crystal, **Figure 4.2**. When $h\nu_1$ (= 1.83 or 2.00 eV) is far below E_g, the OKE signal consists of two responses: a broad feature within ~0.3 ps and an oscillatory response distributed over a few ps (**Figure 4.2A**); the former is liquid-like[151,153] while the latter are Raman active vibrations typical of solids[175]. The corresponding Fourier spectra in **Figure 4.2B** for $h\nu_1$ = 1.83 and 2.00 eV show a broad low-frequency peak (<100 cm^{-1}) in the region of coupled lead-halide stretching and bending vibrations (see calculated frequencies in **Figure 4.2B** and **Figure 4.9**). A few partially resolved phonon peaks are also present in the Fourier spectrum for $h\nu_1$ = 2.00 eV. The broad low-frequency peak, which agrees with the Raman spectra of Yaffe et al.[176], reflects the structural softness of $CsPbBr_3$ whose Young's modulus is similar to that of $CH_3NH_3PbBr_3$; both are 10x lower than those of Si and GaAs[180].

As we increase $h\nu_1$ to the pre-resonant regime (2.21-2.25 eV), we see the resonance-enhancement of slower ps-scale responses in $CsPbBr_3$. This is similar to results from $CH_3NH_3PbBr_3$ and can again be attributed to $PbBr_3^-$ motions. There is one important distinction: in $CsPbBr_3$, we see particularly long-lived oscillations, as well as a broad overdamped feature, while in $CH_3NH_3PbBr_3$ only the overdamped feature is observed. Based on the calculated vibrational frequencies, we assign the particularly prominent peaks at ~50 and ~85 cm^{-1} to Pb-Br-Pb bending modes coupled with Pb-Br stretchings (**Figure 4.9**) and that at ~130 cm^{-1} to the pure Pb-Br stretching modes. When $h\nu_1$ (= 2.43 eV) exceeds E_g, the TR-OKE response changes completely. All oscillatory features disappear upon carrier injection, suggesting that a large number of low frequency modes could couple to photo-generated charge carriers and there could be increased overdamping of the phonon oscillation due to their Coulomb interaction with the charge carriers. Instead of oscilations, we see a sub-ps component with a time constant of τ_1 = 0.7 ± 0.1 ps and longer-lived anisotropy that decays with τ_2= 6.5 ± 0.3 ps (see fitting in **Figure 4.3C** below). Notably, the phonon dynamics upon charge injection are similar in both $CsPbBr_3$ and $CH_3NH_3PbBr_3$, albeit the time constants are longer by ~2x in the former. In $CH_3NH_3PbBr_3$, while there is negligible contribution of the high-frequency organic cation vibrations to polaron formation (see **Figure 4.8**), reorientational motions of such cations within the lead halide cage could couple to Pb-Br-Pb phonon modes, leading to faster polaron formation in $CH_3NH_3PbBr_3$ than that in $CsPbBr_3$ as we confirm below in first principles calculations.

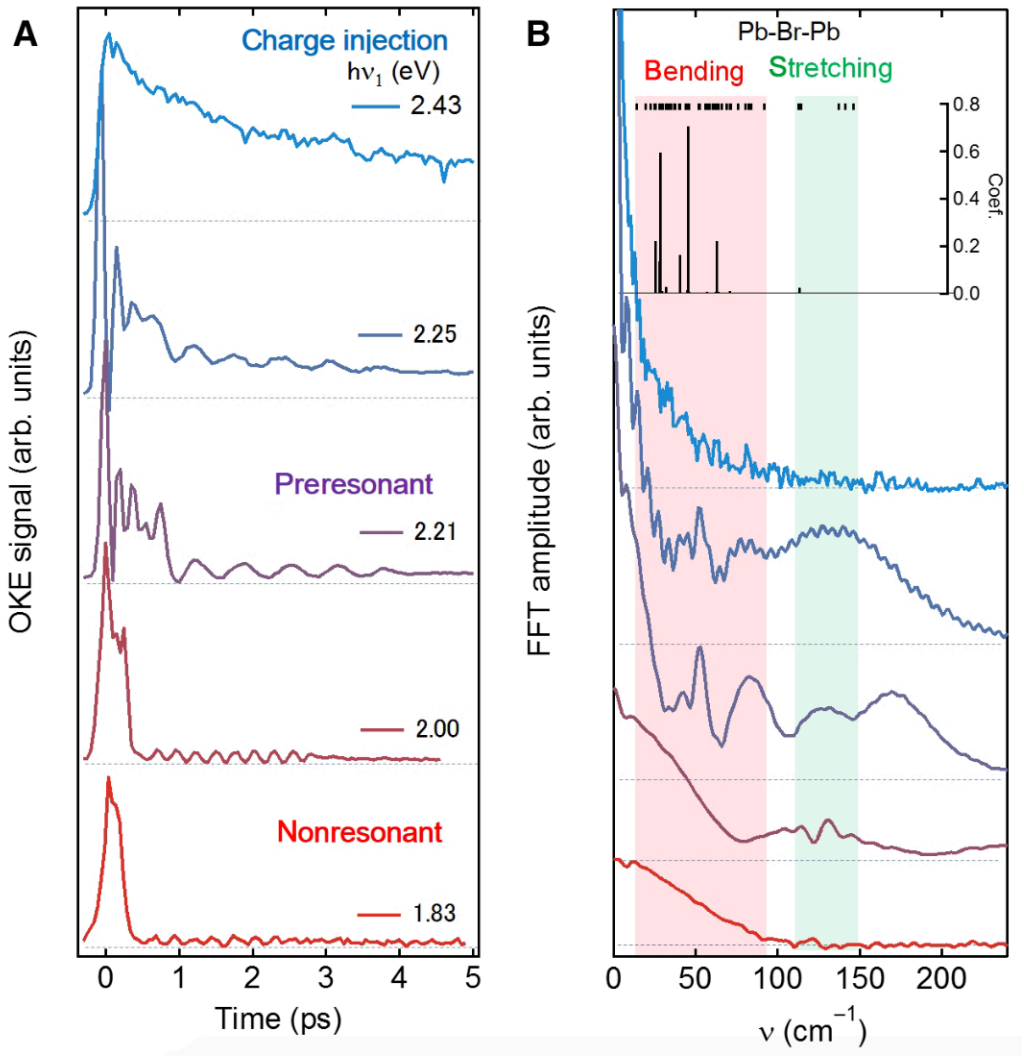

Figure 4.2 TR-OKE transients from a $CsPbBr_3$ crystal. A OKE transients from $CsPbBr_3$ as a function of pump energy (1.83 – 2.43 eV). At the pre-resonant regime, low frequency modes that is coupled to band-edge excitation is enhanced. At the carrier-injection regime, additional sub-ps dynamics manifests itself as well as long-lived polarization does. **B** Fourier spectra of selected transients in non-resonant regime (1.83, 2.00 eV), pre-resonant regime (2.21, 2.25 eV), and carrier injection regime (2.43 eV). The inset is the crystalline structure of $CsPbBr_3$. Black ticks at the top show calculated frequencies of normal modes and sticks represent projections of the displacement vector on the normal modes upon large polaron formation (see **Figure 4.9**). From ref. [49]. Reprinted with permission from AAAS.

The TR-OKE experiments with $h\nu_1 \geq E_g$ probe the injected charge dynamics from the phonon perspective. We now probe the same dynamics from the electronic degrees of freedom side using femtosecond transient reflectance. **Figure 4.3A** shows

a 2D pseudo-color plot of transient absorption coefficiency ($\Delta\alpha$) of $CH_3NH_3PbBr_3$ as a function of probe photon energy and pump-probe delay (Δt) following the excitation at time-zero by $h\nu_1$ = 2.92 eV. Here, α is obtained by a Kramers-Kronig transformation from time-dependent reflectance, $\Delta R/R$ (see Section 4.5.5 and **Figure 4.9** for details)[181]. At Δt > 1 ps, the band-edge spectral region corresponds to simple bleaching of the excitonic resonance, but at shorter times the spectrum features a derivative shape which corresponds to a red-shift in the absorption peak. The red shifted-feature is attributed to band renormalization due to many-body Coulomb interaction among photo-excited carriers, as is well known in inorganic semiconductors[182]. Since the ns lifetime of charge carriers[132] means carrier population remains constant on the sub-ps time scale, the disappearance of the red-shift can thus be attributed to the reduction of the many-body Coulomb potential, consistent with the dynamic screening of initially excited free carriers in polaron formation. A similar transient red-shift has also been observed for $CsPbBr_3$ **Figure 4.10**. The red-shifts disappear with time constants of 0.28 ± 0.04 ps and 0.6 ± 0.1 ps for $CH_3NH_3PbBr_3$ and $CsPbBr_3$, respectively (**Figure 4.3B**). These time constants are in excellent agreement with those of the ultrafast screening time in TR-OKE response at $h\nu_1 \geq E_g$, **Figure 4.3C**, where faster TR-OKE responses yield time constants of τ_1= 0.29 ± 0.04 ps and 0.7 ± 0.1 ps for $CH_3NH_3PbBr_3$ and $CsPbBr_3$, respectively. The long time constants (τ_2 = 3.4 ± 0.5 ps and 6.5 ± 0.3 ps) in TR-OKE are not seen in transient reflectance, suggesting that the ultrafast screening and polaron formation processes are already completed on the sub-ps time scale of τ_1. The

longer time scales can be attributed to further depolarization due to the polaron motion possibly coupled to the slower dynamics of the A-site cations.

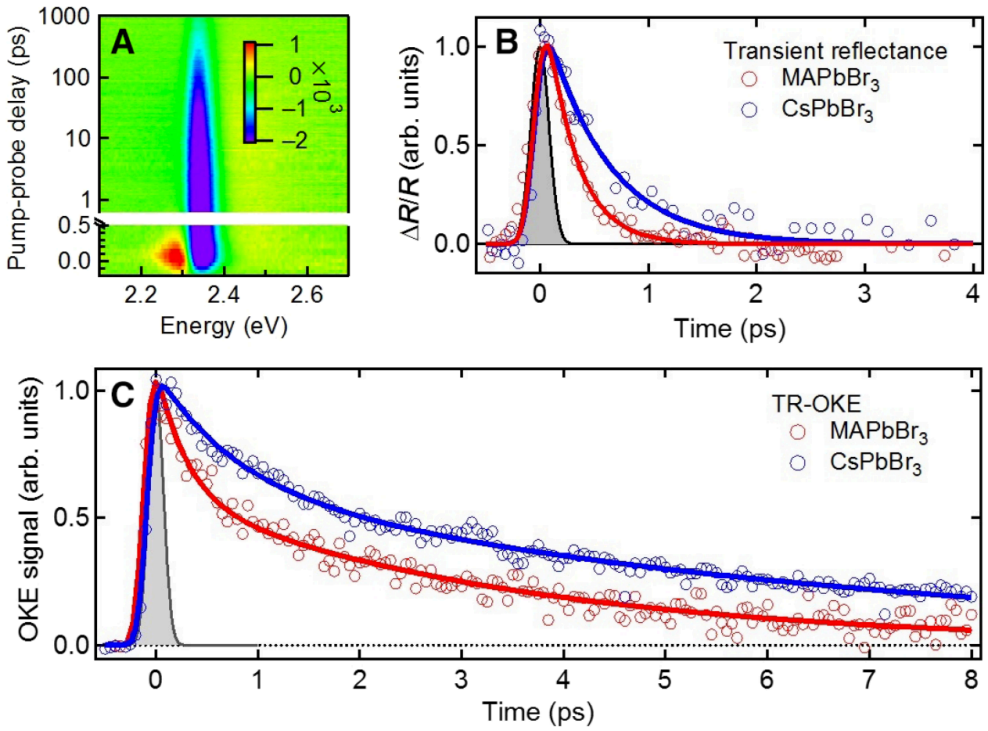

Figure 4.3 Comparison of transient reflectance and TR-OKE with above-gap excitation. A Pseudo-color ($\Delta\alpha$)) representation of transient absorbance spectra of a $CH_3NH_3PbBr_3$ single crystal retrieved from transient reflectance ($\Delta R/R$) pumped by 2.92 eV, 100 μW. **B** The dynamics of screening extracted from transient reflectance probed at 2.31 eV for $CH_3NH_3PbBr_3$ (blue) and at 2.38 eV for $CsPbBr_3$ (red) as a function of pump–probe delay. The lines are mono-exponential fits convoluted with a gaussian function which describes cross-correlation between pump and probe pulse (FWHM 100 fs). **C** The structural dynamics triggered by photo-carrier injection as a function of pump-probe delay observed by TR-OKE with across gap excitation. $CH_3NH_3PbBr_3$ (blue) and at 2.38 eV for $CsPbBr_3$ (red) as a function of pump–probe delay. The lines are double-exponential fits convoluted with a gaussian function which describes cross-correlation between pump and probe pulse (FWHM 70 fs). From ref. [49]. Reprinted with permission from AAAS.

While the TR-OKE responses appear different between CH3NH3PbBr3 and CsPbBr3 when the pump photon energy is below the band gap, as the Raman active phonon modes are partially resolved (oscillatory features in the time domain) in the latter but not in the former, the responses become very similar for across band gap

excitation (charge injection). To understand the seemingly similar origins of polaron formation in $CH_3NH_3PbBr_3$ and $CsPbBr_3$, and to reveal possible distinctive atomistic features underlying the different time response of the two perovskites, we carry out first-principles calculations on pseudo-cubic $CH_3NH_3PbBr_3$ and orthorhombic $CsPbBr_3$ 2x2x1 crystals (corresponding to the room-temperature stable phases) in the absence and presence of positive/negative added charges using the hybrid PBE0 functional[183,184] and the experimental cell parameters[185]. In both $CH_3NH_3PbBr_3$ and $CsPbBr_3$ crystals, we find that a positive added charge induces a much larger structural relaxation than a negative charge, with the most significant variation associated to the average Pb-Br bond length and Pb-Br-Pb bond angle (θ) involving the equatorial Br atoms, **Figure 4.4**. Here we are calculating the local relaxation starting from the minimum energy structure in the absence of charges, likely representing the fast component of the relaxation process observed experimentally. A stabilization energy of 0.06 eV and 0.14 eV is calculated for a positive added charge to $CH_3NH_3PbBr_3$ and $CsPbBr_3$, respectively, while the negative charge is stabilized in both cases by only a few meV. For $CH_3NH_3PbBr_3$, θ increases from 162° to 167° in the positively charged structure, **Figure 4.4B**. For $CsPbBr_3$, a correspondingly larger increase from θ = 153° to 163° is calculated, **Figure 4.4D**; the opposite holds for the negative charge, with θ decreasing by ~2° in both $CH_3NH_3PbBr_3$ and $CsPbBr_3$. The evident Pb-Br-Pb angle increase (decrease) is driven by the shortening (lengthening) of the Pb-Br average bond lengths (-0.04 vs. +0.01 Å for positive and negative added charges, respectively), **Figure 4.4B-D** and **Figure 4.4C-E**. The observed relaxation pattern is consistent with the dominant involvement of the coupled Pb-Br stretching and Pb-Br-Pb bending modes in

polaron stabilization. This is most obvious in projected displacement vectors associated with a positive charge in $CH_3NH_3PbBr_3$ and $CsPbBr_3$ (inset in **Figure 4.1B** and **Figure 4.2B** and detailed in **Figure 4.8** and **Figure 4.9**. Associated with the Pb-Br-Pb angle increase due to the positive charge, the CH_3NH_3 and Cs cations also respond by progressively moving towards their cubic sites, **Figure 4.4B-D**; the opposite holds for negative charge. Thus, the overall atomic relaxation associated with positive (negative) charge leads to more cubic (tilted) crystal structures. We confirm this trend also in $CH_3NH_3PbI_3$, with similar stabilization energy and structural distortion as for $CH_3NH_3PbBr_3$ (**Figure 4.11**) indicating the mechanism is common to lead-halide perovskites. This general conclusion is consistent with the observation of photostriction in $CH_3NH_3PbI_3$ single crystal[137] and with the suggestion of elongation of the $[PbBr_6]^{4-}$ octahedra in $CH_3NH_3PbBr_3$ nanocrystals upon charge injection[136].

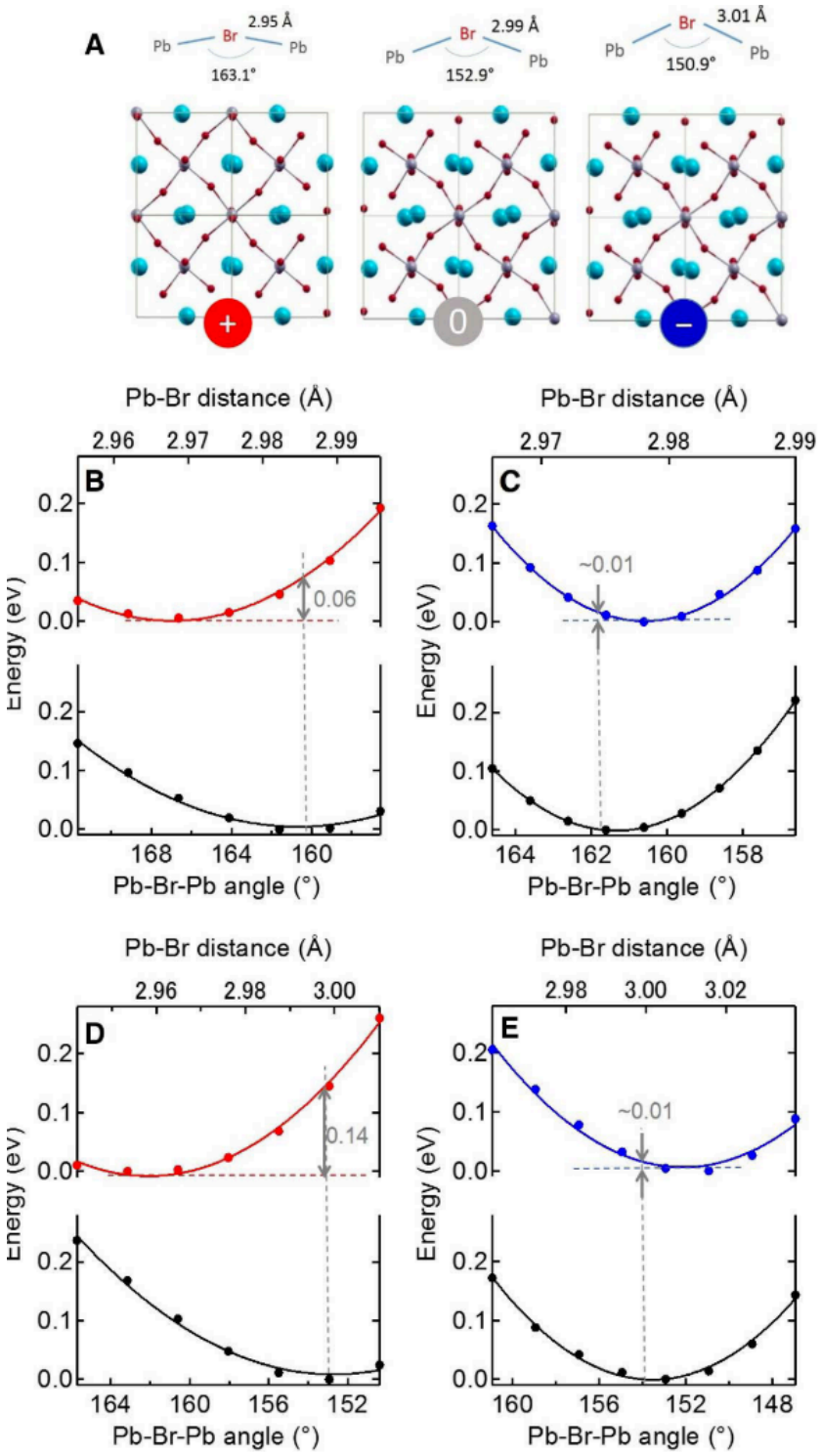

Figure 4.4 Hybrid DFT calculations. A The relaxed structures of $CH_3NH_3PbBr_3$ with positive and negative charge injection. Changes in Pb-Br-Pb bending and Pb-Br length are shown. **B-E** Potential energy surfaces for relaxation of the (**B, C**) $CH_3NH_3PbBr_3$ and (**D, E**) CsPbBr3 unit cell (four formula units) upon positive (**B, D**; red curve) and negative (**C, E**; blue curve) charge injection. The neutral state energy (black) along the distortion coordinate is also shown. From ref. [49]. Reprinted with permission from AAAS.

The structural reorganization for an added hole is much larger than that caused by an added electron in either $CH_3NH_3PbBr_3$ or $CsPbBr_3$. This contrast between positive and negative charges can be understood by the different origins of valcence and conduction bands. The valance band is comprised of antibonding combinations of Pb-6s and Br-4p orbitals, while the conduction band is domibated by the Pb-6p orbital. As a result, the valence band should be much more sensitive than the conduction band is to the bending/stretching of Pb-Br-Pb. This implies that electrons experience less localization from the octahedral distortion than the holes do. To estimate the size of the polaron, we have carried out additional hybrid DFT calculations on a 2x2x8 $CsPbBr_3$ supercell, obtained by replicating the crystal unit cell along the c axis. The cubic cell parameter was first optimized for the neutral case providing a value of 5.93 Å, matching the experimental value of 5.9 Å[185]. By simultaneously shortening the Pb-Br bonds and, thus, the long supercell dimension, we find an increase in energy of the neutral system, but ~0.1 eV stabilization for the positive system (**Figure 4.13**). Upon geometrical relaxation of the 2x2x8 supercell in the presence of a positive added charge, we obtain a distribution of Pb-Br distances along the long cell dimension, **Figure 4.5A**, which clearly correlates with the decay of density associated with the added hole away from a center of maximum distortion, **Figure 4.5B**. This is the signature of the large polaron distortion, which slowly decays away from the point of maximally localized charge (set at the center) and approaching saturation for a radius of $\rho_h \sim 2.5$ nm. This polaron dimension is likely a lower bound approximation to the actual value due to the finite size of the employed supercell. We are not able to similarly estimate the polaron size for an added electron due to the much smaller structural distortion requiring larger supercell sizes to

observe a saturation behavior. However, our calculation suggests that the electron and the hole are localized in spatially distinct regions. By varying the Pb-Br distances in different crystal regions, we are able to localize the excess positive (negative) charge in regions of shorter (longer) Pb-Br distances, **Figure 4.14**. A similar behavior is retrieved when we modulate the octahedra tilting (**Figure 4.15**), with the positive charge mainly localized in the untilted region characterized by shorter Pb-Br bonds. The opposite structural distortion accompanying positive and negative excess charges suggests a spatially separated distribution of photogenerated electrons (more delocalized) and holes (more localized), consistent with a barrier to electron-hole recombination[186].

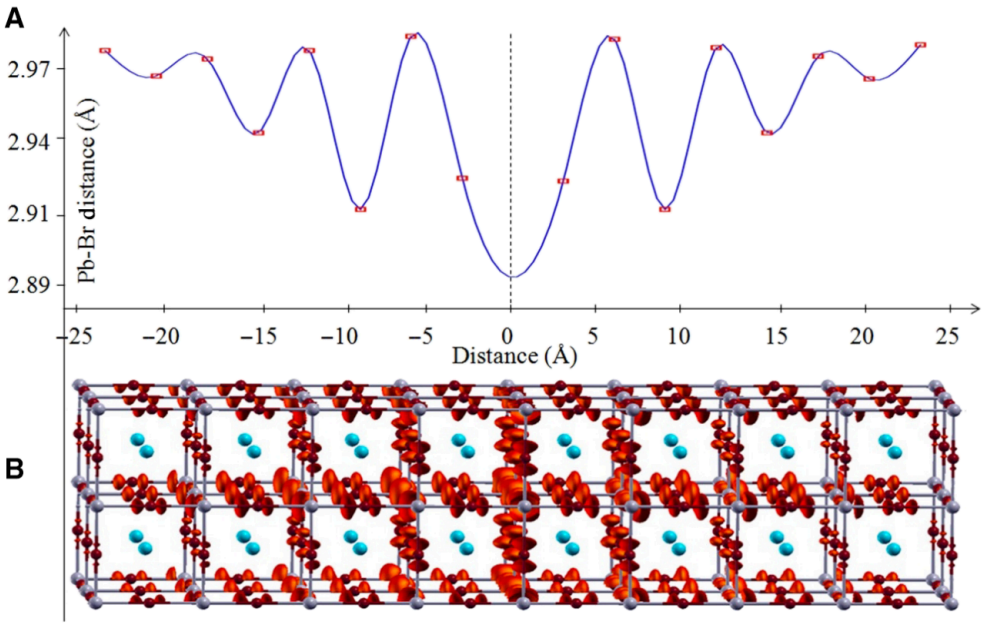

Figure 4.5. Estimation of polaron size from first principles. A Distribution of Pb-Br distances (Å, top panel) of the positive polaron state for a pseudo-cubic 2x2x8 $CsPbBr_3$ model made by 32 formula units. **B** The distribution of the excess positive charge (red isosurface) following the pattern of Pb-Br distances. The figure has been centered at the maximum of hole localization. From ref. [49]. Reprinted with permission from AAAS.

We point out that the present calculation focuses on $PbBr_3^-$ lattice phonons that are most strongly coupled to the electronic degrees of freedom in $APbBr_3$. It may be necessary to use a much larger supercell, possibly coupled to long-time scale molecular dynamics simulations, to account for the reorientational motion of the $CH_3NH_3^+$ cations in polaron formation. This approach is computationally beyond reach for the type of first-principles calculations used here, but could be feasible with more approximate methods. By sampling randomly generated configurations of the $CH_3NH_3^+$ cations in $CH_3NH_3PbI_3$, Ma and Wang found localization of conduction and valence bands to spatially separate regions with radii of $\rho_e \sim 8.3$ and $\rho_h \sim 5.6$ nm for electrons and holes, with estimated stabilization energies as large as 100 meV[114]. The larger screening exerted by the dipolar organic cations, as is illustrated in

the approximations of Ma and Wang[114], may also explain the different polaron stabilization energies between $CH_3NH_3PbBr_3$ (60 meV) and $CsPbBr_3$ (140 meV) in our calculation. This was verified in separate calculations in which we removed the A-cations and re-calculated the stabilization energy considering the geometries for the full system. In this case, we calculate a similar positive charge relaxation energy of ~0.09 eV in both $CH_3NH_3PbBr_3$ and $CsPbBr_3$ (**Figure 4.12**), clearly pointing to the A-cations as being responsible of the difference between the two perovskites beyond the different phases.

Our calculations not only reveal the essential role of the $PbBr_3^-$ sublattice in polaron formation, they also explain quantitatively the different polaron formation rates between $CH_3NH_3PbBr_3$ and $CsPbBr_3$. The projections of the displacement vector on the normal modes upon large polaron formation (black sticks in **Figure 4.1 B** and **Figure 4.2B**) give mean frequencies of $\langle\bar{\upsilon}\rangle$ = 92.4 cm^{-1} and 40.8 cm^{-1} in $CH_3NH_3PbBr_3$ and $CsPbBr_3$, respectively. These mean frequencies correspond to time constants of 0.36 ps and 0.82 ps, in excellent agreement with the corresponding time constants of τ_p = 0.3 ps and 0.7 ps in $CH_3NH_3PbBr_3$ and $CsPbBr_3$, respectively, observed in TR-OKE measurements. This difference can be attributed to the different coupling of cation motions to $PbBr_3^-$ lattice phonon modes; the faster motion of $CH_3NH_3^+$ (reorientation) than that of the heavier Cs^+ (displacement) can account for the different $\langle\bar{\upsilon}\rangle$ or τ_p between $CH_3NH_3PbBr_3$ and $CsPbBr_3$.

We can estimate charge carrier mobilities and large polaron sizes based on the formulism of Fröhlich[29] and Feynman[30]. Because the low frequency phonon modes (≤ 150 cm-1, **Figure 4.1 B** and **Figure 4.2B**) mainly responsible for polaron formation in $CH_3NH_3PbBr_3$ and $CsPbBr_3$ are highly populated at room temperature,

the more general formula of Osaka is more appropriate[187]. The strength of electron-LO phonon coupling is represented by the unit-less Fröhlich coupling constant, α_{e-ph}which can be calculated from the LO phonon frequency, carrier band mass, and dielectric constants. Based on our calculated LO phonon frequencies, we obtain α_{e-ph} = 1.54 and 1.87 in $CH_3NH_3PbBr_3$ for the electron and the hole, respectively. The corresponding values in $CsPbBr_3$ are α_{e-ph}= 2.64 and 2.76, for the electron and the hole, respectively (see Section 4.5.6). The weaker e-ph coupling in $CH_3NH_3PbBr_3$ than that in $CsPbBr_3$ and the weaker e-ph coupling for the electron than that for the hole are both in agreement with the first principles results in **Figure 4.4**. These coupling constants are a bit smaller than those in conventional inorganic perovskite materials, e.g., α_{e-ph}= 3-4 in $SrTiO_3$ [188]. We obtain from the Feynman-Osaka formula[30,187] electron and hole polaron mobilities of μ_e = 149.8 $cm^2V^{-1}s^{-1}$ and μ_h = 79.2 $cm^2V^{-1}s^{-1}$ with corresponding polaron radii of ρ_e= 4.18 nm and ρ_h = 3.13 in $CH_3NH_3PbBr_3$. The corresponding values in $CsPbBr_3$ are μ_e = 48.2 $cm^2V^{-1}s^{-1}$, μ_h = 41.3 $cm^2V^{-1}s^{-1}$, ρ_e = 2.67 nm, and ρ_h = 2.49 nm (see Section 4.5.6). The calculated ρ_h in $CsPbBr_3$ is in excellent agreement with the estimation value from first principles calculation, **Figure 4.5**. Our results are also in good agreement with similar treatments by Sendner et al. who estimated an average electron/hole polaron mobility in $CH_3NH_3PbBr_3$ of μ_{e-h} ~ 158 $cm^2V^{-1}s^{-1}$ for a polaron radius of 4.3 nm and by Frost who calculated electron and hole polaron mobilities in $CH_3NH_3PbI_3$ of 136 and 94 $cm^2V^{-1}s^{-1}$, respectively[189]. These estimated polaron mobilities are in good agreement with the uppers bounds in the range of experimental values from single crystals at room temperature[14,15,25,26,132,190]: 10-115 $cm^2V^{-1}s^{-1}$ for $CH_3NH_3PbBr_3$, 24-164

$cm^2V^{-1}s^{-1}$ for $CH_3NH_3PbI_3$, and 38 cm^2 V^{-1} s^{-1} for $CsPbBr_3$. Thus, it is mainly optical, not acoustic, phonons that limit charge carrier mobility in lead halide perovskites. Note that while the experimentally determined temperature dependences in charge carrier mobility [26,186,191] are in agreement with the $\mu \propto T^{-1.5}$ scaling law predicted from acoustic phonon scattering in nonpolar semiconductors [192], analysis based on this mechanism yields charge carrier mobilities of the order of 10^3 $cm^2V^{-1}s^{-1}$[1193–196] which is one order of magnitude higher than experimental values[14,15,25,26,132,190]. Note also that the weakly bound large polarons obtained here are responsible for coherent transport[28], in contrast to the more tightly bound small polarons that may function as minority trapped charges[129].

4.4 Conclusions

In summary, we provide a time-domain experimental view and first-principles verification of large polaron formation in $CH_3NH_3PbBr_3$ and $CsPbBr_3$. The combined experiment and calculation establish deformation of the $PbBr_3^-$ sublattice as mainly responsible for large polaron formation in both crystals. The large polaron model predicts modest charge carrier mobilities that are in excellent agreement with experimental measurements. The lower frequencies of the $PbBr_3^-$ sublattice motions (coupled to A-cation motion) in $CsPbBr_3$ than those in $CH_3NH_3PbBr_3$ also explains quantitatively the experimentally observed large polaron formation time constants. The difference in large polaron formation rate accounts for its competitiveness with hot carrier cooling in $CH_3NH_3PbBr_3$ and $CH_3NH_3PbI_3$[20,21], not in $CsPbBr_3$[20], but the large polarons may otherwise show similar properties due to common deformations

of the lead halide sublattice. The latter suggests a similar mechanism for the protection of band-edge carriers in HOIPs and their all-inorganic counterparts, thus accounting for similar solar cell performance and similar bandedge carrier properties obtained with purely organic, inorganic and mixed-cation perovskites[132,172–174]. Alloying different organic and inorganic A-cations, which was shown to be an effective strategy towards high efficiency devices[197], could be a way of tuning the extent of polaron stabilization to balance charge carrier protection (screening) and mobility.

4.5 Appendix: Supplementary Materials

4.5.1 Synthesis and structural characterizations of LHP macro-crystals

Millimeter-scale single crystal samples of $CH_3NH_3PbBr_3$, and $CsPbBr_3$ were prepared under ambient conditions via a vapor diffusion method in which the vapor of an antisolvent slowly diffuses into a perovskite precursor solution as described in the Appendix[117]. $CH_3NH_3PbBr_3$ crystals were grown by the slow diffusion of dichloromethane (DCM) into a solution of $PbBr_2$ and CH_3NH_3Br (1:2 molar ratio, 0.5 M and 1.0 M) in N,N-dimethylformamide (DMF). $CsPbBr_3$ crystals were grown by the modified vapor diffusion method described in The Appendix in which a solution of $PbBr_2$ and CsBr (1:1 molar ratio, 0.4 M) in DMSO was prepared. The antisolvent was MeOH[198].

The single crystalline nature of the perovskite samples were confirmed by SCXRD as shown in **Figure 0.1**. The lattice constants are given in **Table 0.1**. These are consistent with literature values and reflect the pseudocubic phase for $CH_3NH_3PbBr_3$ and the orthorhombic phase for $CsPbBr_3$[199,200].

4.5.2 Time-resolved optical Kerr effect measurements

We carried out femtosecond TR-OKE measurements using a home-built two-color pump-probe system described in Section 3.3. The outputs from two non-collinear optical parametric amplifiers (NOPAs) served as pump and probe lasers pulse for the measurements for $CH_3NH_3PbBr_3$ except the one at $h\nu_1$ = 2.30 eV. In this measurement, the NOPAs were pumped by the second and third harmonic of a Yb-doped fiber laser (Clark-MXR Impulse) operated at 500 kHz. The center wavelengths of the visible pump and NIR probe pulses were in the range of 1.85-2.25 eV (tunable) and 1.61-1.66 eV, respectively. The bandwidths for both pulses were ~0.10 eV (full-width-at-half-maximum). Pulse energies were 4 nJ and 0.3 nJ for the pump and probe pulses with its spot sizes of about 600 μm and 120 μm, respectively. The pulses are focused on the sample with polarizations set to 45° with respect to each other, whereas a delay line is used to control the time delay between the pulses. The probe polarization was along the [100] crystal direction. The pump beam beam was blocked after the sample, whereas the probe beam was directed through a second polarizer, which was set at the crossed-polarization against the first polarizer in front of the sample. To achieve heterodyne detection, a local oscillator was introduced by rotating the second polarizer by either +2 or -2° away from the homodyne orientation which gives maximum extinction of the probe beam. This is described in further detail in Section 3.3. The Kerr signal was detected by a large area amplified PIN photodiode (THORLABS, 100A) with 700 nm longpass filter to eliminate an scattered pump beam, and recorded by a lock-in amplifier (Stanford Research Systems, SR830) synchronized with the modulation of the pump beam intensity by a mechanical chopper at 5 kHz. For the measurements for a

$CH_3NH_3PbBr_3$ crystal at $h\nu_1$ = 2.30 eV and all the OKE measurement for a $CsPbBr_3$ crystal, the output pulses from NOPA pumped by the second harmonic of a Ti:Sapphire laser (Wyvern1000-50, KMLabs) operated at 10 kHz was used as tunable pump pulses (1.83-2.48 eV) in order to gain higher energy pulses, and its fundamental pulses (1.55-1.57 eV) was used as probe. Pulse energies were 30 nJ and 3 nJ for the pump and probe pulses, respectively. The Kerr signal was detected by home-built spectrometer equipped with a high-speed linear array detector (AVIIVA EM4, EV71YEM4CL1014-BA9, e2v) synchronized with the modulation of the pump beam intensity by a mechanical chopper at 5 kHz for shot-to-shot detection. Data collection was done via a home-built program based on Labview. The typical temporal response measured by the cross-correlation between the pump and probe pulses from a 1 mm thick glass plate was 70 ± 5 fs (FWHM).

4.5.3 Time resolved reflectance measurements

Transient reflection measurements made use of a 1 mJ Ti:sapphire femtosecond regenerative amplifier operating at a repetition rate of 1 kHz (Newport Spectra-Physics). The pump laser light (~100 fs pulse width) comes from an optical parametric amplifier (TOPAS). The probe, a white-light supercontinuum (450-900 nm), was focuses onto sample with a small overlapped angle to the pump. The reflected probe light from a perovskite crystal was collected by a mirror and lenses. The detection consists of a pair of high-resolution multichannel detector arrays coupled to a high-speed data acquisition system (Ultrafast Systems). A heat filter was added to the probe beam path prior to the sample to remove the residual fundamental laser beam. The probe power over the entire spectrum was a few

hundred nanowatts. The sample was mounted inside a quartz window cell containing inert gas to avoid sample degradation by absorbing oxygen and moisture.

4.5.4 Theoretical calculations

DFT calculations have been performed on the tetragonal phases of $MAPbI_3$ and $MAPbBr_3$ (48 atoms in unit cells) and on the orthorhombic phase of $CsPbBr_3$ (20 atoms in the unit cell), corresponding to 4 formula units in all cases. We employed the experimental cell parameters throughout the work. We relaxed the geometries of both the neutral, positive and negative (+1 and -1 charge) systems in periodic boundary conditions by GGA-DFT. This procedure is representative of the crystals being investigated at low temperature, where dynamic fluctuations due to thermal energy can be neglected. Thus the results refer to the perfect crystals at zero temperature although the phases are those corresponding to the room temperature stable phases for each system. The displacement vector was extracted as the difference of the geometrical coordinates in the neutral and charged states. This defines a global configurational coordinate that drives the system across the two minima, defined by the neutral and charge systems. Next, the energy was calculated as a function of the displacement along the identified distortion pathway, by performing both GGA (PBE)[201] and hybrid (PBE0)[183] DFT calculations. To quantify the displacement on the same scale for all the investigated systems we calculated the mean square displacement (MSD) of all atoms in the cell along the pathway, as well as the variations of the Pb-Br distances and of the Pb-Br-Pb angles.

Frequency calculations have been performed by GGA-DFT at the experimental cell parameters for consistency with the relaxation and projection

procedures. A 4x4x4 k-point mesh was employed, which ensures converged results (see ref. [171]).

PBE calculations (structural relaxations and phonon calculations) have been performed by using ultrasoft pseudopotentials with a cutoff on the wavefunction of 25 Ryd (200 Ryd on the charge density) and uniform 4x4x4 grid of k-points in the Brillouin Zone. Single point PBE0 calculations have been performed employing norm-conserving pseudpotentials with a cutoff on the wavefunctions of 40 Ryd and the same k-points grids used for the PBE calculations. The convergence of the cutoff in hybrid calculations as well as the reliability of our approach in the determination of the minima and the relaxation energies of the charged systems have been checked by performing full PBE0 relaxation calculations on the charged and neutral orthorhombic phase of CsPbBr3 with a cutoff of 70 Ryd on the wavefunctions. Relaxation of ions for the neutral, positive and negative charged systems show relaxed geometries and relaxation energies in excellent agreement with the simulated pathways. All calculations in the work have been carried by using the QuantumEspresso simulation package[202].

4.5.5 Kramers-Kronig Analysis

The complex refractive index is given by:

$$\tilde{n} = n + ik \tag{4.5.1}$$

Here, the real part *n* is the refractive index and the imaginary part *k* is the extinction coefficient. The change of refractive index can be calculated from transient reflectance signal as[203]:

$$\frac{\Delta R}{R}(\hbar\omega) = \frac{4\Delta n(\hbar\omega)}{n(\hbar\omega)^2 - 1} \tag{4.5.2}$$

where $n(\hbar\omega)$ was adapted from Saidaminov et al[190].

The Kramers-Kronig Relations is given by:

$$Im[\tilde{n}(\omega)] = \frac{-2\omega}{\pi} P \int_0^\infty \frac{Re[\tilde{n}(\omega')]}{\omega'^2 - \omega^2} d\omega' \tag{4.5.3}$$

$$Re[\tilde{n}(\omega)] = \frac{2}{\pi} P \int_0^\infty \frac{\omega' Im[\tilde{n}(\omega')]}{\omega'^2 - \omega^2} d\omega' \tag{4.5.4}$$

We used eq. (4.5.2) to calculate $\Delta n(\hbar\omega)$, and plug this value into eq. (4.5.3) to calculate the change of imaginary part, $\Delta k(\hbar\omega)$. The change of absorption coefficient is then calculated by:

$$\Delta\alpha(\hbar\omega) = \frac{4\Delta k(\hbar\omega)}{\lambda} \tag{4.5.5}$$

4.5.6 Estimation of Fröhlich couplings and mobilties

The behavior of polarons have been analyzed by Fröhlich model where a charge in polar medium coupled to harmonic optical phonons. A strength of electron-phonon coupling is characterized by so called Fröhlich coupling, α_{e-ph}, defined by

$$\alpha_{\mathrm{e-ph}} \equiv \frac{e^2}{\hbar}\frac{1}{4\pi\epsilon}\left(\frac{1}{\varepsilon_\infty}-\frac{1}{\varepsilon_0}\right)\sqrt{\frac{m}{2\hbar\omega}}, \tag{4.5.6}$$

where e is the charge of carrier; $2\pi\hbar$ is the Planck's constant; ϵ is the dielectric constant of vacuum; ε_∞ and ε_0 are optical and static dielectric constants, respectively; m is effective mass of bare electron band; ω is angular frequency of a characteristic longitudinal optical (LO) phonon mode. Parameters for the calculation of α_{e-ph} in **Table 4.1**. We estimate ω from the calculated Im$[1/\varepsilon(\omega)]$ spectra in far infrared region (see **Figure 4.16**).

We find that the polaron in $CH_3NH_3PbBr_3$ and $CsPbBr_3$ are in large-intermediate regime (α_{e-ph}= 1~3). The most successful model for describing the polaron in the regime at finite temperature is provided by Osaka based on the path integral calculation demonstrated by Feynman. In the model, the self free energy of polaron, F, with α_{e-ph}, under the phonon occupation factor $\beta = \hbar\omega/k_{\mathrm{B}}T$ (where k_{B} is the Boltzman constant and T is temperature) is calculated with two free parameter v and w.[30,204] To obtain the ground state of the polaron, we numerically find v and w that give the minimum $F = -(A + B + C)$ where

$$A = \frac{3}{\beta}\left[\ln\left(\frac{v}{w}\right) - \frac{\ln(2\pi\beta)}{2} - \ln\frac{\sinh\left(\frac{v\beta}{2}\right)}{\sinh\left(\frac{w\beta}{2}\right)}\right] \tag{4.5.7}$$

$$B = \frac{\alpha v}{\sqrt{\pi}[\exp(\beta)-1]}\int_0^{\frac{\beta}{2}} \frac{\exp(\beta-x)+\exp(x)}{\sqrt{w^2x\left(1-\frac{x}{\beta}\right)+\frac{Y(x)(v^2-w^2)}{v}}}\,\mathrm{d}x \tag{4.5.8}$$

$$Y(x) = \frac{1}{1-\exp(-v\beta)}[1+\exp(-v\beta)-\exp(-vx)-\exp\{v(x-\beta)\}] \tag{4.5.9}$$

$$C = \frac{3(v^2-w^2)}{4v}\left(\coth\left(\frac{v\beta}{2}\right) - \frac{2}{v\beta}\right). \quad (4.5.10)$$

v and w have a unit of ω, and in particular v is the frequency of relative motion between a charge and a coupled LO phonon. We can calculate reduced mass (m_{red}) of the relative motion and the expectation value of the squared distance between the charge and the phonon which defines Feynman large polaron radius (ρ) as below.[205]

$$m_{\mathrm{red}} = m\frac{v^2-w^2}{v^2} \quad (4.5.11)$$

$$\rho = \sqrt{\frac{3\hbar}{2m_{\mathrm{red}}\times v\times 2\pi\omega}} \quad (4.5.12)$$

In the theory, mobility, μ, is described by[206,207]

$$\mu = \frac{3\sqrt{\pi}e}{2\pi\omega m\alpha}\frac{\sinh(\beta/2)}{\beta^{5/2}}\frac{w^3}{v^3}\frac{1}{K} \quad (4.5.13)$$

$$K = \int_0^\infty \frac{\cos(u)}{(u^2+a^2-b\cos(v\cdot u))^{3/2}}\,\mathrm{d}u \quad (4.5.14)$$

$$a^2 = \left(\frac{\beta}{2}\right)^2 + \left(\frac{v^2-w^2}{w^2v}\right)\beta\coth\left(\frac{\beta v}{2}\right) \quad (4.5.15)$$

$$b = \left(\frac{v^2-w^2}{w^2v}\right)\frac{\beta}{\sinh\left(\frac{\beta v}{2}\right)}. \quad (4.5.16)$$

The calculated parameters for the polarons. Fröhlich coupling constants ($\boldsymbol{\alpha}$), phonon occupation factors ($\boldsymbol{\beta}$), parameters at the lowest energy polaron in the Feynman-Osaka formula (v and w), Feynman polaron radii ($\boldsymbol{\rho}$) and mobilities ($\boldsymbol{\mu}$) are tabulated in **Table 4.2**.

4.5.7 Supplementary Figures

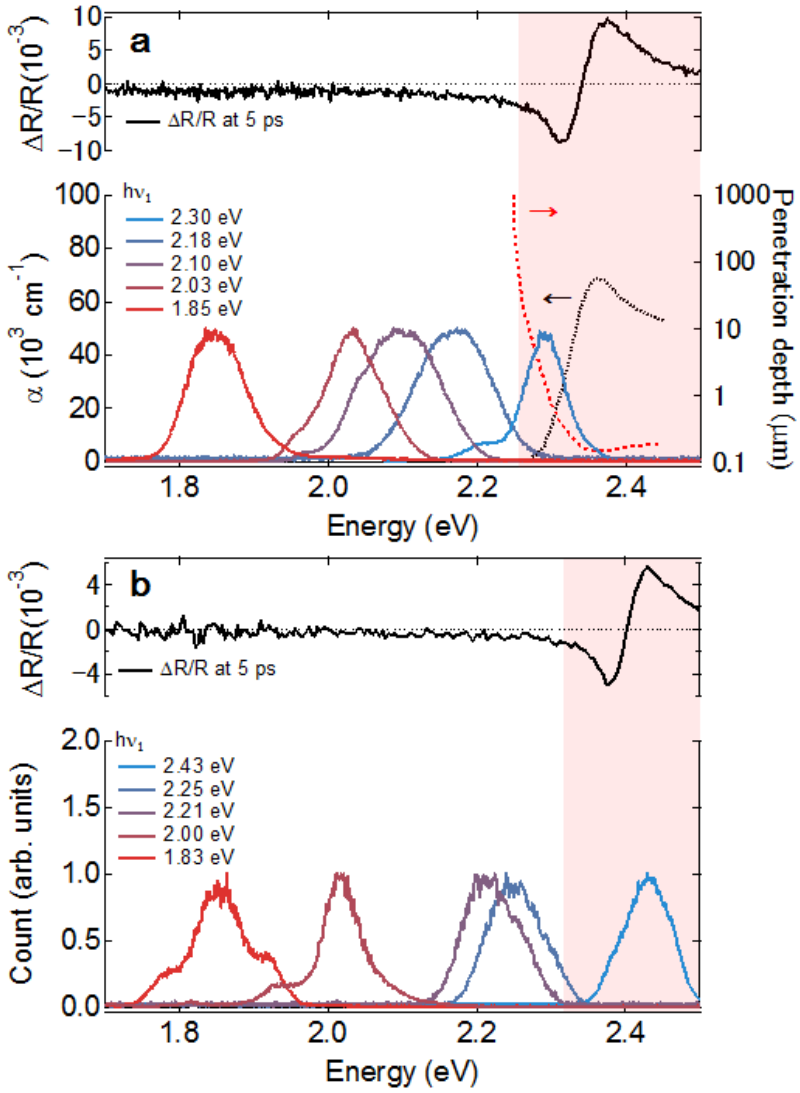

Figure 4.6 The spectra of pump pulses in the TR-OKE measurement for **A** $CH_3NH_3PbBr_3$ and **B** $CsPbBr_3$. Extinction coefficient (red broken line) from Ref. 181 and calculated penetration depth (black broken line) as a function of photon energy (a). Spectra of pump pulses (solid colored lines) and $\Delta R/R$ at the delay time at 5 ps (solid black line) are also shown (**A,B**). Red shaded areas show effective regions where photons are absorbed to create carriers estimated from the position of exciton absorption peak and its width extracted from the $\Delta R/R$ spectra and the penetration depth. From ref. [49]. Reprinted with permission from AAAS.

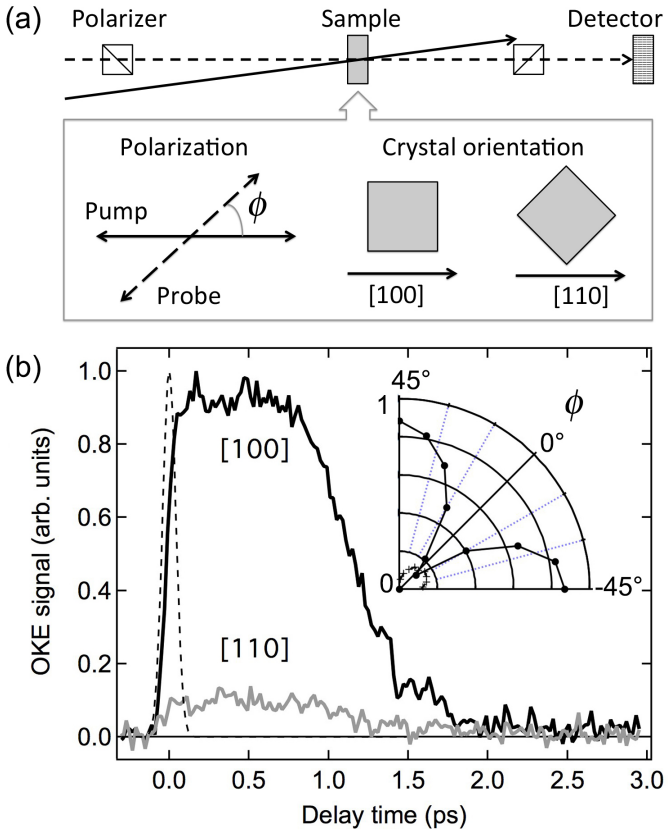

Figure 4.7 TR-OKE schematic and pump-polarization dependence of $CH_3NH_3PbBr_3$. A A schematic diagram of TR-OKE measurement. **B** Polar plots of TR-OKE signals for a $CH_3NH_3PbBr_3$ crystal as a function of the polarization of a pump pulse. (Red line) measured with $E_{\mathrm{probe}} \parallel [110]$ (Blue line) $E_{\mathrm{probe}} \parallel [100]$. (**C,D**) TR-OKE transients as a function of the polarization of a pump pulse **C** measured with $E_{\mathrm{probe}} \parallel [110]$, **D** $E_{\mathrm{probe}} \parallel [100]$. The black spectrum in **B** shows TR-OKE response from $CH_3NH_3PbBr_3$ with the pump polarization along the [100] crystal direction ($h\nu_1$ =2.0 ± 0.05 eV). The absolute signal intensity varies as a function of f and peaks at f = 45° (polar plot in the insert), confirming that the single comes from light-induced transient anisotropy with heterodyne detection. While the prompt rise of OKE signal can be attributed to the ultrafast electronic response represented by the laser pump-probe cross correlation (dashed curve), the signal remains for over 1 ps from nuclear contributions. The broad picosecond OKE response in **B** is distinctively different from those of typical solids, but is characteristic of OKE responses from liquids of anisotropic molecules. There are no oscillatory features in the TR-OKE response from $CH_3NH_3PbBr_3$, indicating that we are detecting predominantly over-damped phonon modes due to strong anharmonicity and dynamic disorder. Interestingly, the TR-OKE signal is suppressed by one order of magnitude when the pump electric field is changed from the [100] direction to the [110] direction. Note that the weak residual signal from polarization along the [110] direction does not show the dependence on f as expected from heterodyne detection of OKE signal (gray dots and curve in the polar plot); it likely comes from scattering of probe light from imperfections of the crystalline sample. From ref. [49]. Reprinted with permission from AAAS.

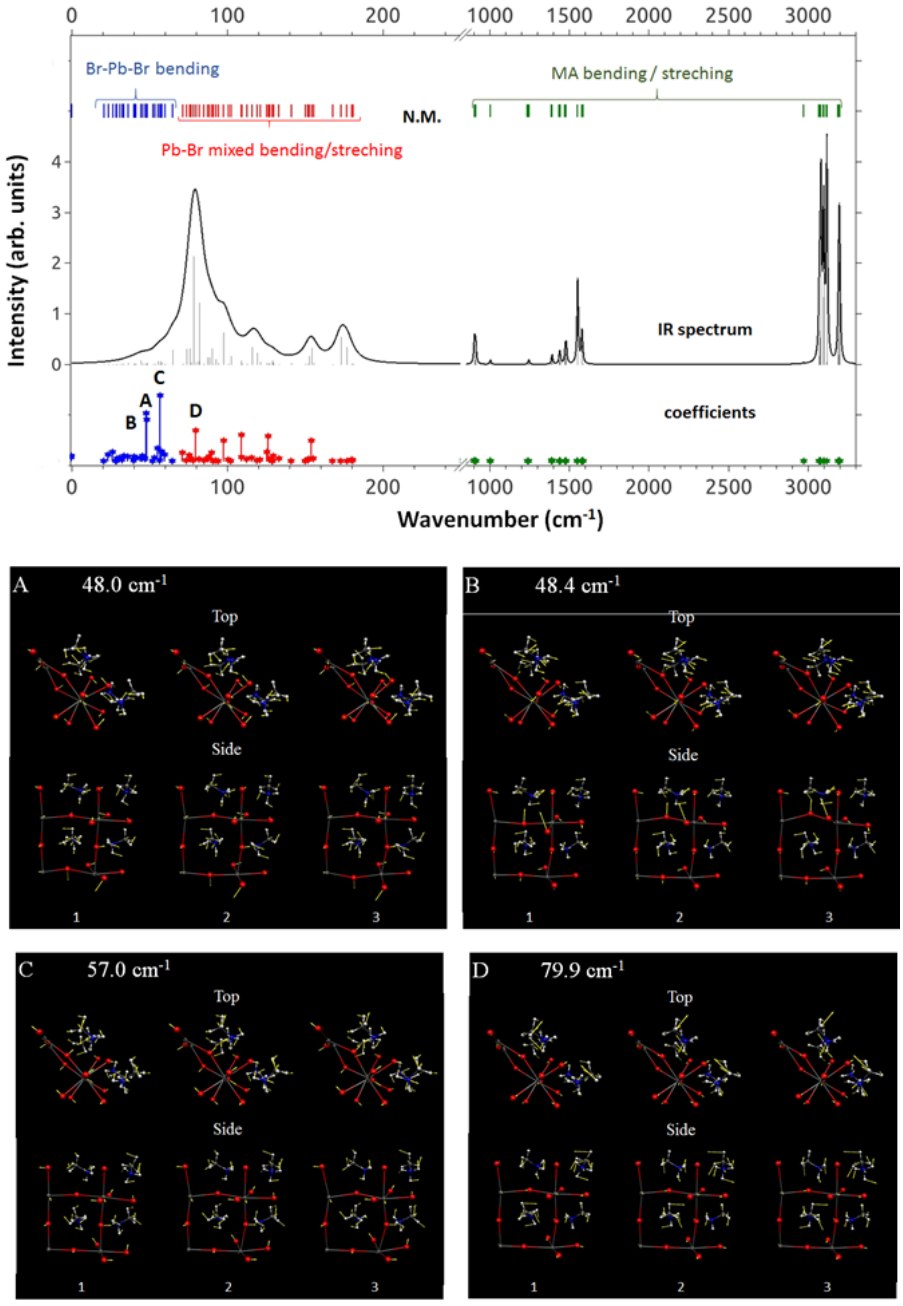

Figure 4.8 (Top panel) Calculated IR spectrum and the coefficients of the displacement vector associated with a positive charge injection in $CH_3NH_3PbBr_3$ projected to the normal modes. A-D show the four strongest-coupled modes to the displacement. (Lower panels) Specific atomic motions for selected normal modes. Strongly coupled modes (**A-D**) contain Pb-Br-Pb bending motion. Note that all the frequencies show higher frequency shifts compared to $CsPbBr_3$ due to the lighter cation mass. In addition, higher frequencies over 300 cm^{-1} which are assigned to pure CH_3NH_3 (MA) cation motions can be found, but their couplings to the displacement are almost negligible. These trends clearly show $PbBr_3$ framework largely contributes to large polaron formation even in the presence of MA cations, which is consistent with the observation of strong couplings on slow inorganic motions. From ref. [49]. Reprinted with permission from AAAS.

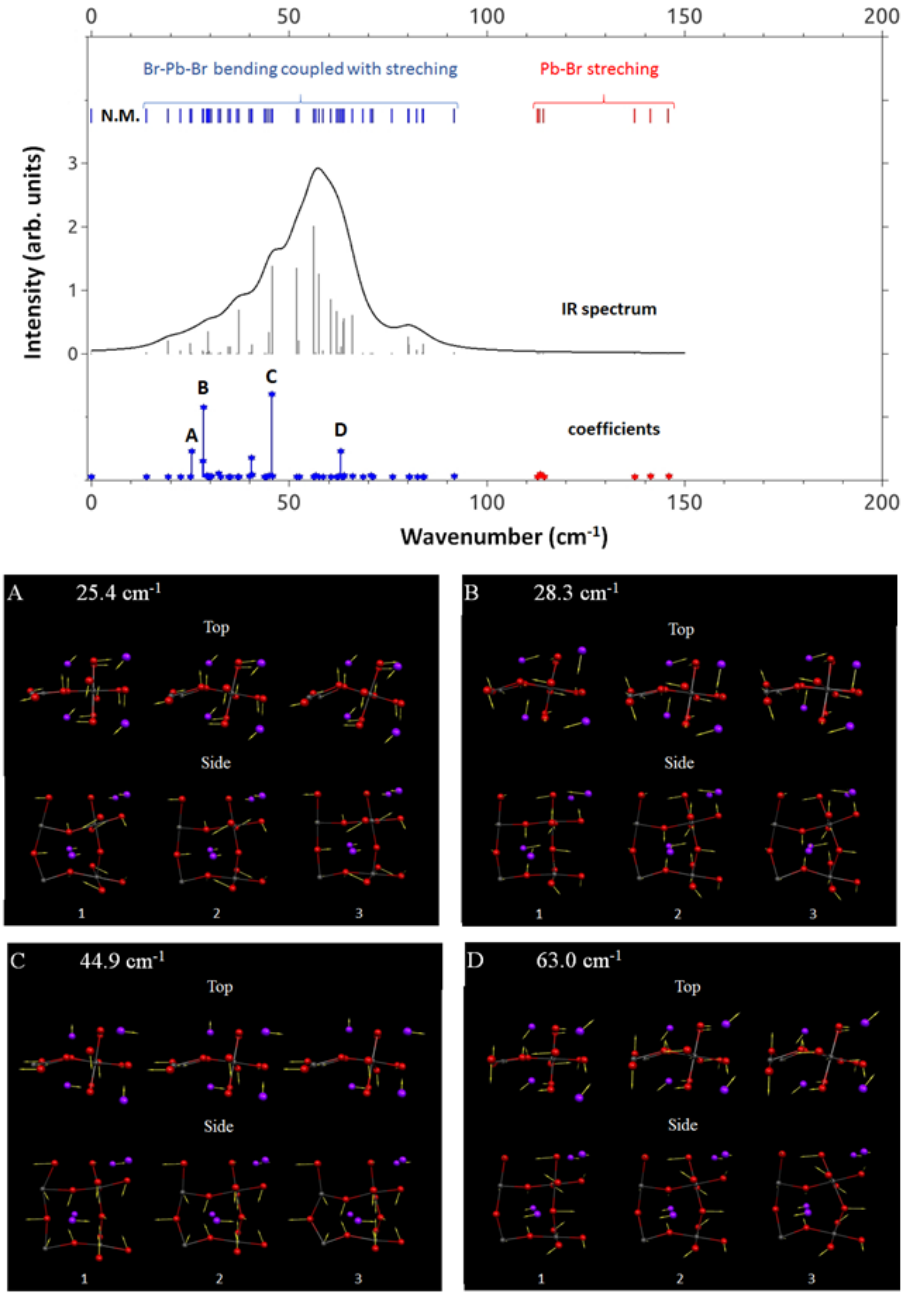

Figure 4.9 (Top panel) Calculated IR spectrum and the coefficients of the displacement vector associated with a positve charge injection in $CsPbBr_3$ projected to the normal modes. **A-D** show the four strongest-coupled modes to the displacement. (Lower panels) Specific atomic motions for selected normal modes. All strongly coupled 4 modes (**A-D**) clearly show Pb-Br-Pb bending. In contrast, modes at higher frequencies (>100 cm^{-1}) are less coupled. From ref. [49]. Reprinted with permission from AAAS.

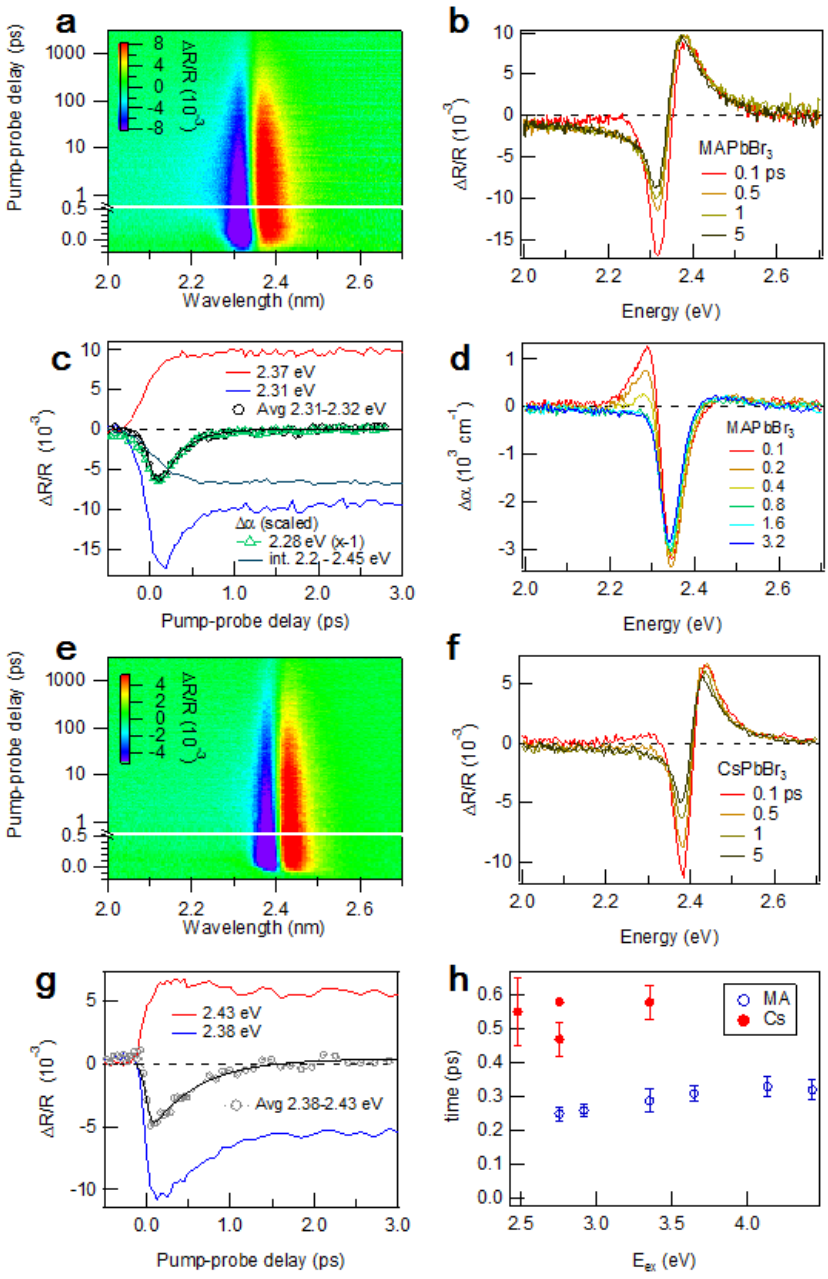

Figure 4.10. **A,B** $\Delta R/R$ for $CH_3NH_3PbBr_3$ single crystal pump at 2.92 eV. **C** Comparison of the dynamics of transient reflectance and $\Delta\alpha$ in $CH_3NH_3PbBr_3$. The dynamics of retrieved $\Delta\alpha$ corresponds well with that of $\Delta R/R$. **D** Calculated $\Delta\alpha$ as a function of pump-probe delay in $CH_3NH_3PbBr_3$. Kramers-Kronig analysis clearly shows the change is rather red-shift than changing in the bleaching of the excitonic absorption at 2.35 eV. **E,F** $\Delta R/R$ for CsPbBr3 single crystal pump at 2.75 eV. **G** The dynamics of transient reflectance in CsPbBr3. **H** Time constants of sub-ps dynamics as a function of pump energy, showing the time constant is nearly independent of excitation energy. From ref. [49]. Reprinted with permission from AAAS.

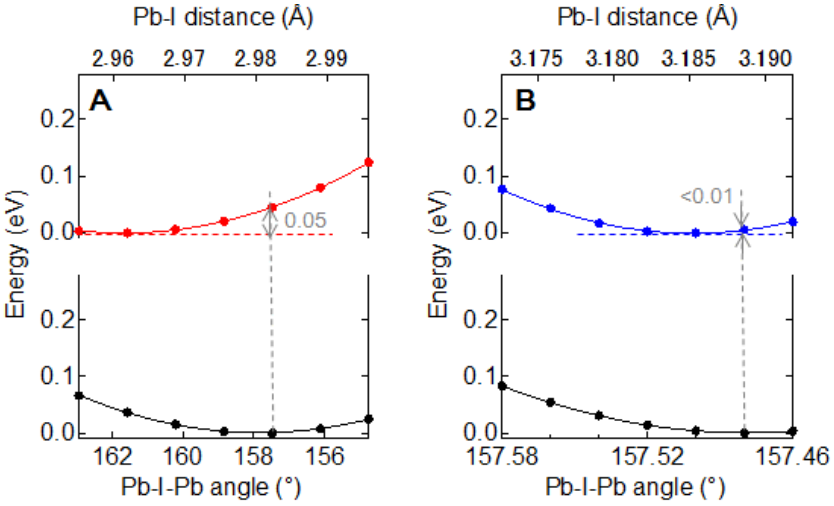

Figure 4.11 Hybrid DFT calculations of the relaxed structures of $CH_3NH_3PbI_3$ with positive and negative charge injection. A Potential energy surfaces for relaxation upon positive (**A**; red curve) and negative (**B**; blue curve) charge injection. The neutral state energy (black) along the distortion coordinate is also shown. From ref. [49]. Reprinted with permission from AAAS.

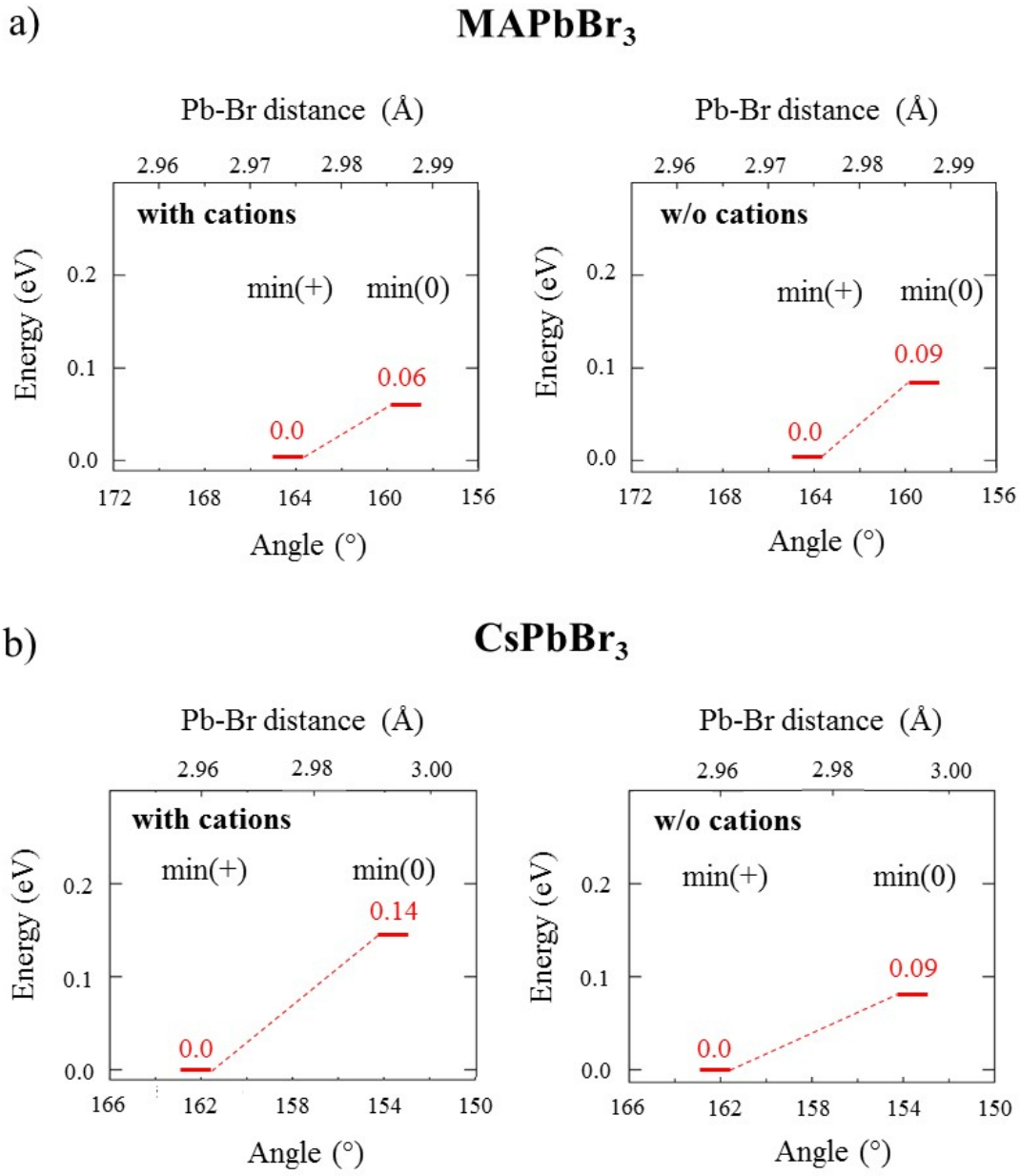

Figure 4.12 Hybrid DFT calculations. Stabilization energy of $CH_3NH_3PbBr_3$ **A** and $CsPbBr_3$ **B** with positive added charge in the full system (left panels) and excluding the A-cations (right panels). Changes in Pb-Br-Pb bending and Pb-Br length for the full systems are also shown. The geometries of the systems without A-cations were kept fixed to those optimized by PBE0 for the full system. From ref. [49]. Reprinted with permission from AAAS.

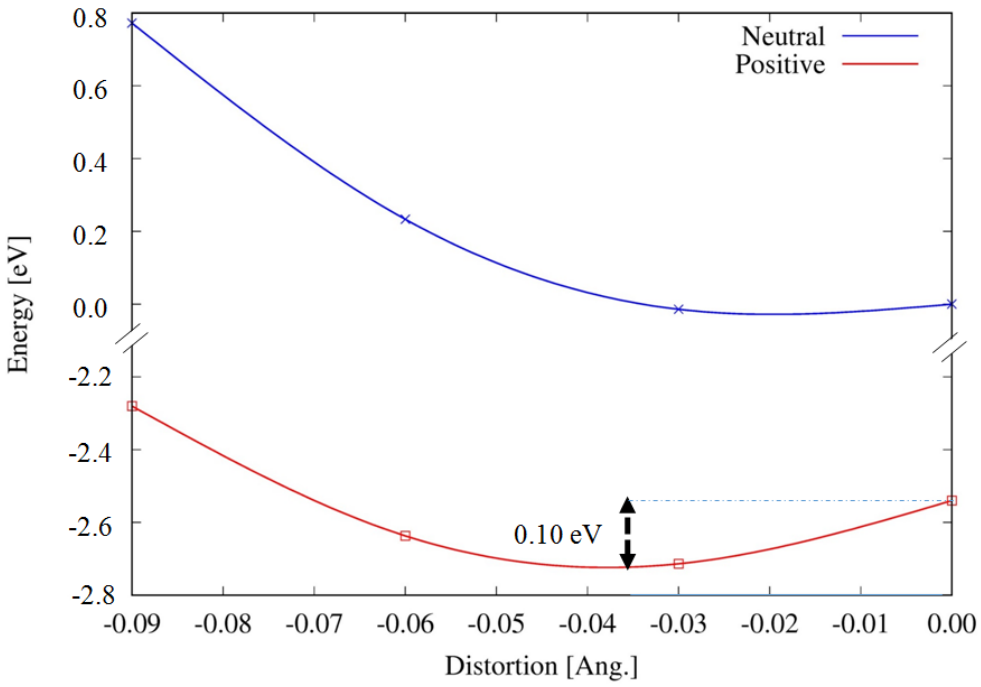

Figure 4.13 Potential energy surface for the neutral (blue) and positive (red) charged 2x2x8 cubic $CsPbBr_3$ supercells as a function of the contraction of Pb-Br bond lengths (Å) and correspondingly of the lattice parameter along the long cell dimension. Notice that while the positively charge supercell shows a 0.10 eV stabilization, the neutral system does not show any stabilization, indicating the preferential stabilization of the positive charge along the explored Pb-Br coordinate. From ref. [49]. Reprinted with permission from AAAS.

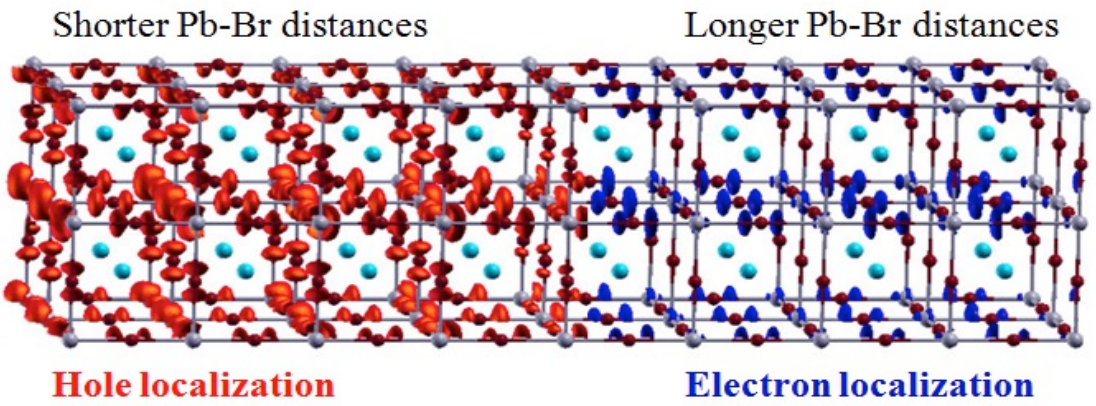

Figure 4.14 Pseudo-cubic 2x2x8 $CsPbBr_3$ model with elongated (shortened) Pb-Br bonds in the left (right) halves of the supercell, superimposed to the excess negative (blue) and positive (red) charge densities from separate calculations on the entire supercell adding in turn a negative and positive charge. From ref. [49]. Reprinted with permission from AAAS.

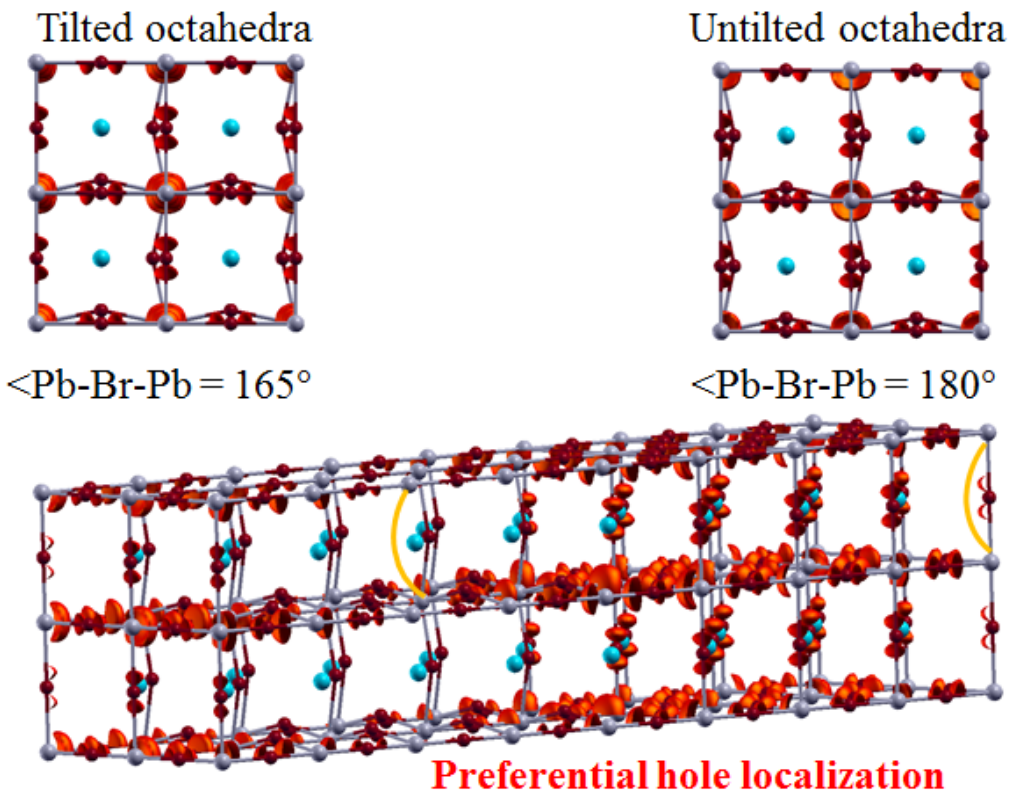

Figure 4.15 Exploring the localization of the positive charge as a function of the octahedral tilting in the left 2x2x8 $CsPbBr_3$ supercell side. Notice the preferential localization of the positive charge in the untilted, right side of the Figure. Along with reducing the tilting angle from 180° to 165°, a lengthening of the Pb-Br bonds of ~0.06 Å is computed. From ref. [49]. Reprinted with permission from AAAS.

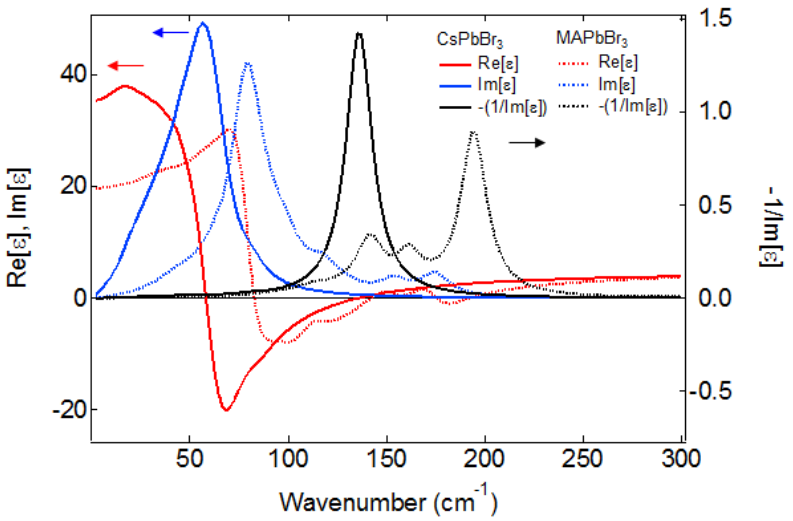

Figure 4.16 Calculated dielectric functions of $CsPbBr_3$ (solid lines) and $MAPbBr_3$ (dashed lines) in far infrared region. Real part (red), imaginary part (blue) of dielectric function and imaginary part of the inverse dielectric function (black). The dominant LO phonon frequencies are at 194 and 136 cm^{-1} for $CsPbBr_3$ and $MAPbBr_3$, respectively. From ref. [49]. Reprinted with permission from AAAS.

4.5.8 Supplementary Tables

Table 4.1 The list of input parameters for the polaron calculations. Optical and static dielectric constants (ε_∞ and ε_0, respectively), angular frequencies of a characteristic LO phonon mode (ω), and effective masses of bare electron bands (m). From ref. [49]. Reprinted with permission from AAAS.

Material	ε_∞	ε_0	$\omega/2\pi$ [THz]	m
$MAPbBr_3$ - h	4.4	21.36	5.81*	0.19
$MAPbBr_3$ - e				0.13
$CsPbBr_3$ - h	4.3	29.37	4.07*	0.24**
$CsPbBr_3$ - e				0.22**

* The frequencies of dominant LO phonon are estimated from –Im[1/ ε] spectra in **Figure 4.16**.

** Taken from ref. 207.

Table 4.2 The list of calculated parameters for the polarons. Fröhlich coupling constants (α), phonon occupation factors (β), parameters at the lowest energy polaron in the Feynman-Osaka model (v and w), Feynman polaron radii (ρ) and mobilities (μ). From ref. [49]. Reprinted with permission from AAAS.

Material	α	β	v	w	ρ [nm]	μ [cm^2/Vs]
$MAPbBr_3$ - h	1.87	0.97	7.83	6.43	3.13	79.2
$MAPbBr_3$ - e	1.54		7.66	6.53	4.18	149.8
$CsPbBr_3$ - h	2.76	0.68	11.29	8.73	2.49	41.3
$CsPbBr_3$ - e	2.64		11.22	8.79	2.67	48.2

5 Coherent Phonon Transfer and Softening

Adapted with permission from:

Maehrlein, S. F.*; **Joshi, P. P.***; Wang, F.; Juraschek, D. M.; Cherasse, M.; Zhu, X.-Y. Spectroscopic Signatures for Ferroelectric Charge Localization in Lead Halide Perovskites. *Submitted.*

*indicates equal author contribution

Discussed experiments were conducted by Sebastian F. Maehrlein and myself. Single crystals were grown by Feifan Wang. The coupled-oscillator model was developed by Dominik M. Juraschek.

Abstract

Anharmonic and dynamically disordered phonons in lead halide perovskites (LHPs) play vital roles in their exceptional optoelectronic properties[50,52,67,91,176]. Electron-phonon interaction in LHPs has been hypothesized to result in large polaron formation[20,34,49,104,112,208], charge localization by polar nano domains[209–211], and electronic band splitting in momentum space in the presence of local symmetry breaking[97–100]. The standard picture for electron-phonon coupling is the Fröhlich polaron theory[29,30], which has been applied to LHPs[49,103,189], but the implicit harmonic approximation is problematic for an explicitly anharmonic lattice. Unveiling the hitherto-unknown local lattice environment specific to charge carriers is a critical step towards understanding electron-phonon interaction in LHPs. Here, we use time-resolved coherent phonon spectroscopy (CPS) to probe the lattice dynamics specific to localized charge carriers in $CsPbBr_3$ single crystals[212]. We selectively excite the below-bandgap polaronic state which initiates localized coherent phonons. Surprisingly, the initially excited phonon at 5.3 THz is transferred on sub-picosecond time scales to phonon modes at ~2.6 THz, which continuously soften to 1.6 THz,

with coherence maintained throughout the process. Such ultrafast coherent transfer and effective softening are absent for phonons not associated with charge carriers in $CsPbBr_3$ and are unprecedented in solid materials[213–216]. Our finding provides a direct time-domain view of the extreme anharmonicity in the local lattice environment of polarons in LHPs.

5.1 Introduction

Phonons in LHPs are known to be highly anharmonic and dynamically disordered, as shown by X-ray and neutron scattering, low-frequency Raman spectroscopy, solid-state NMR, and molecular dynamics simulations[60,62,76,79,176,217,218]. While some disorder can be attributed to the reorientation of organic cations in the $CH_3NH_3PbX_3$ (X = Cl, Br, I) family, the dominant contribution arises from fluctuations of the lead-halide sub-lattice[62,63,176,217,219]. The interaction between a charge carrier and optical phonons can be inferred in part from the dielectric response. The real part of the frequency dependent dielectric function (ε_1) increases by up to an order of magnitude across the broad transverse optical (TO) phonon resonances in LHPs[34,52]. For comparison, the relative increase of ε_1 across the TO resonance is only 18% in the harmonic lattice of GaAs[34,107]. While the standard Fröhlich polaron theory[29,30] treats the displacement of lattice ions by an extra charge within the linear response limit, it is now increasingly evident that electron-phonon coupling in LHPs needs to be treated in the context of the nonlinear, highly anharmonic, and dynamically disordered lattice environment[34,220]. Despite extensive

studies on phonon dynamics and electron-phonon coupling in LHPs, little is known about the anharmonic environment specific to a localized charge.

Here, we use time-resolved coherent phonon spectroscopy (CPS) to probe single crystalline $CsPbBr_3$ with a linearly polarized and tunable visible pump pulse ($h\nu_1$= 2.25 or 2.05 eV, pulse width sub-30 fs, 10 kHz). The lattice dynamics are tracked by the polarization change of a probe pulse ($h\nu_2$ = 1.55 eV, pulse width 45 fs, 10 kHz). All measurements were carried out at room temperature (295 K). We improve upon previous optical Kerr effect (OKE) experiments[20,49] by implementing a balanced detection scheme, as discussed in Chapter 3. The suppression of unpolarized scattering and transient absorption contributions improves the signal-to-noise ratio by orders-of-magnitude, thus allowing us to improve upon the work by Miyata and coworkers[49] and detect coherent phonon transfer and softening in $CsPbBr_3$ in the present study. In concurrent work shown in Chapter 6,[212] we showed that the tunability of the pump pulse allows us to access two distinct regions: when $h\nu_1$ is in the range of 2.15-2.30 eV, i.e. within 150 meV of the bandgap (E_g = 2.30 eV), the pump pulse selectively excites polaronic states and displacively launches coherent phonons specific to the local lattice environment. At $h\nu_1$ < 2.15 eV, the pump pulse excites coherent phonon modes via impulsive stimulated Raman scattering in the $CsPbBr_3$ crystal[49].

5.2 Results and Discussion

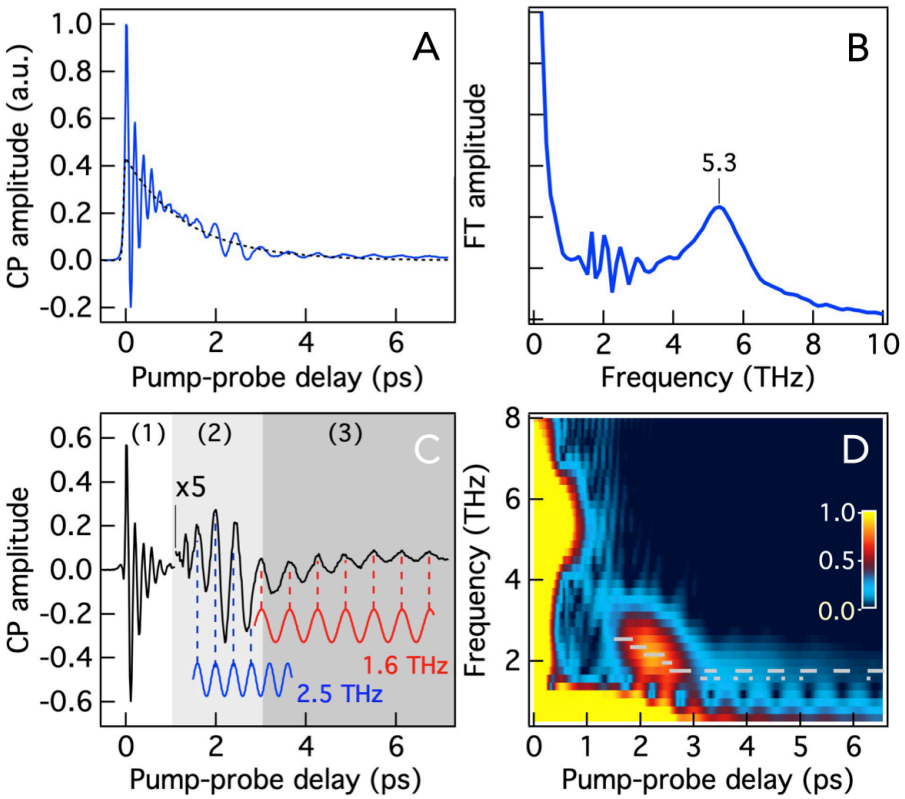

Figure 5.1 CsPbBr3 at 295 K. A CP trace with $h\nu_1$ = 2.25 and $h\nu_2$= 1.55 eV for pump-probe delay (Δt) up to 7 ps. The dashed curve is a single exponential fit, which represents an incoherent background. **B** FT of the CP trace in **A** with the background subtracted. **C** The background subtracted CP trace (black, intensity x5 for Δt > 1 ps) in comparison to two sine waves (blue, 2.5 THz; red, 1.6 THz). The vertical dashes mark the peaks of the sine waves. **D** Pseudo color (FT amplitude) representation from a moving-window FT analysis of the CP trace in **A**. The grey dots mark the peak position in the 2.6-1.6 THz range.

Figure 5.1A shows the pump induced polarization rotation from $CsPbBr_3$ pumped at $h\nu_1$= 2.25 eV, which is within the photon energy range for excitation of below-gap polaronic states.[212] We observe coherent oscillations on top of an incoherent background (dashed curve, a single exponential fit). The oscillation consists of multiple frequencies, as evident in the Fourier transform (FT) of the transient birefringence, **Figure 5.1B**, which shows a broad high-frequency peak centered at ν

~ 5.3 THz and multiple low frequency peaks around 2 THz. The most surprising result from the high-resolution time domain study is that the multiple coherent phonon frequencies seen in the FT spectrum (**Figure 5.1B**) do not occur at the same time (**Figure 5.1A**). At the sub-picosecond timescale, the high frequency mode at 5.3±0.8 THz dominates. After ~1 ps, we observe a beating between the 5.3 THz mode and growing low frequency modes centered at approximately half the frequency of ~2.6 THz. The latter does not remain constant, but rather shifts continuously to 1.6 THz until ~ 3 ps and there is little change at longer times.

To illustrate the evolution of the coherent phonon frequency with time, we show in **Figure 5.1C** the background-subtracted TR-OKE trace and divide the pump-probe delay into three windows: (1) Δt = 0-1 ps; (2) Δt = 1-3 ps; and (3) $\Delta t >$ 3 ps; note the signal intensity is scaled by 5x in regions (2) and (3). Also shown for comparison are two sine waves with frequencies of 2.5 THz (blue) and 1.6 THz (red), respectively. The chirp or softening of region (2) is obvious from the increasing offset of coherent maxima in the time trace from those in the sine wave (blue). In contrast, peaks in region (3) remain in phase with the sine wave (red), indicating little change to the coherent phonon frequency. The distortion of peaks in region (3) from the sine shape suggests a further beating of multiple components in a narrow frequency range. As another representation of the time-dependent evolution of coherent phonon frequency, we perform a time-frequency analysis of the coherent phonon trace that is based on Fourier transform using a moving time window (width 1.2 ps), also called short-time Fourier Transform (STFT). This analysis gives the average coherent phonon frequency as a function of pump-probe delay, as shown in two-dimensional pseudo-color plot in **Figure 5.1D**. The gray dots at $\Delta t \geq$ 1.5 ps

indicate the local maxima in the Fourier amplitude. This analysis clearly reveals the coherent transfer of the 5.3 THz mode to the ~2.6 THz mode in ~ 1 ps and the subsequent coherent softening from 2.6 THz to 1.6 THz within the Δt window of 1-3 ps. At $\Delta t \geq 3$ ps, the coherent phonon frequency remains nearly constant at 1.6±0.1 THz, albeit with an increasing beating feature attributed to the interference of multiple frequencies slightly below 1.6 THz.

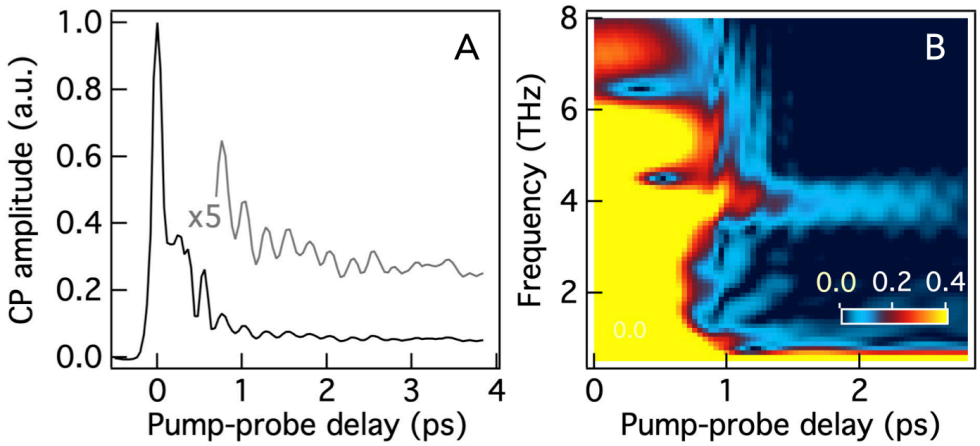

Figure 5.2 TR-OKE of $CsPbBr_3$ at 295 K with $h\nu_1$ = 2.05 eV and $h\nu_2$ = 1.55 eV. A CP trace (black) for pump-probe delay (Δt) up to 4 ps. The trace for Δt > 0.7 ps is multiplied by 5x and reproduced as the grey trace. **B** Pseudo color (FT amplitude) representation from a moving-window FFT analysis of the CP trace in **A**. The blue dashed line shows the center frequency at 3.9 THz.

When the pump photon energy $h\nu_1$ is below the range for the excitation of polaronic states, we observe impulsively stimulated Raman excitation of phonon modes[49,212]. This is investigated for $h\nu_1$ = 2.05 eV, **Figure 5.2A**, where the coherent phonon response of the CP signal is weaker than that in **Figure 5.1**B. At $h\nu_1$ = 2.05 eV, the transient birefringence trace consists of an initial sharp peak with width characteristic of the pump-probe cross correlation. This initial response is attributed

to the instantaneous non-resonant electronic polarization. It is followed by weaker phonon responses of mostly sinusoidal oscillations at Δt > 0.5 ps, as obvious in the scaled trace (x5, gray). The constant frequency of the coherent phonon is most evident in the STFT analysis (width 2 ps), shown as pseudo-color plot in **Figure 5.2**B. The phonon frequency of n = 3.9±0.2 THz does not change with pump-probe delay. Similar results are obtained for other excitation photon energies < 2.15 eV ($h\nu_1$ = 1.88 – 2.14 eV, **Figure 5.5**). Based on FT analysis, we estimate an upper limit in full-width-at-half-maximum of $\Delta\nu \leq$ 0.45 THz, which corresponds to a dephasing time of $\tau_d \sim$ 0.7 ps; for comparison, the dephasing time of the 5.3 THz mode in **Figure 5.1** is shorter, at $\tau_d \sim$ 0.3 ps (**Figure 5.7**).

As detailed elsewhere[212], $h\nu_1$ in the range of 2.15-2.30 eV selectively excites the below-gap polaronic states with binding energies of E_b = 150-0 meV. The frequency of the initially launched coherent phonon by displacive excitation varies from ν_{ph}= 3.5±0.2 THz for E_b = 0 to 7.0±0.2 THz for E_b = 150 meV. Specifically, the coherent phonon frequencies for $E_b \geq$ 30 meV are outside the range of normal phonon modes in ground state $CsPbBr_3$ and are specific to the local lattice environment of polarons[212]. Here, coherent phonon-to-phonon transfer and softening are only observed for below-gap polaronic transitions, **Figure 5.1**, not for phonon modes excited outside this range, **Figure 5.2**. We conclude that the ultrafast phonon transfer and softening dynamics reflect the unique local lattice environment specific to polarons.

In conventional solids, phonon softening occurs with increasing electronic excitation density. In a pump-probe experiment, the excitation density decreases with

time. The initial phonon softening thus appears as an increase in phonon frequency, i.e., hardening, with pump-probe delay after pulsed excitation[214–216]. However, our observation of the drastic decrease in coherent phonon frequency with time (5.3 THz → 1.6 THz), **Figure 5.1**, is the complete opposite. The relative change in phonon frequency is order(s)-of-magnitude higher than those in all solids reported to date[214–216,221,222] and notably occurs at a fixed excitation density, due to the long carrier lifetimes in single crystal LHPs[12,132]. This dramatic change in phonon frequency also occurs in the absence of a macroscopic phase transition. Both the ultrafast time scale and the coherent nature of phonon transfer/softening in **Figure 5.1** reveal extremely large and anharmonic coupling of the initially excited local phonon mode to the surrounding phonon bath. To illustrate this point, we carry out model simulation of the first step in the phonon-phonon coupled dynamics in **Figure 5.1**.

In phonon-phonon scattering, the dominant process requires the participation of three phonons to satisfy energy and momentum conservation[222]. In the present case, one phonon at ~5.3 THz mode is coherently transferred to two phonons at ~2.65 THz, which corresponds to a parametric decay process (**Figure 5.3A**)[221]. Coherent parametric phonon decay has been observed for the coupling of a zone-center optical mode to two high wavevector longitudinal acoustic modes in bismuth via X-ray diffuse scattering[221]. Here, we uniquely witness a Γ- to Γ-point parametric optical phonon decay, which is directly observed optically. It can be seen as a reverse of sum-frequency ionic Raman scattering[223].

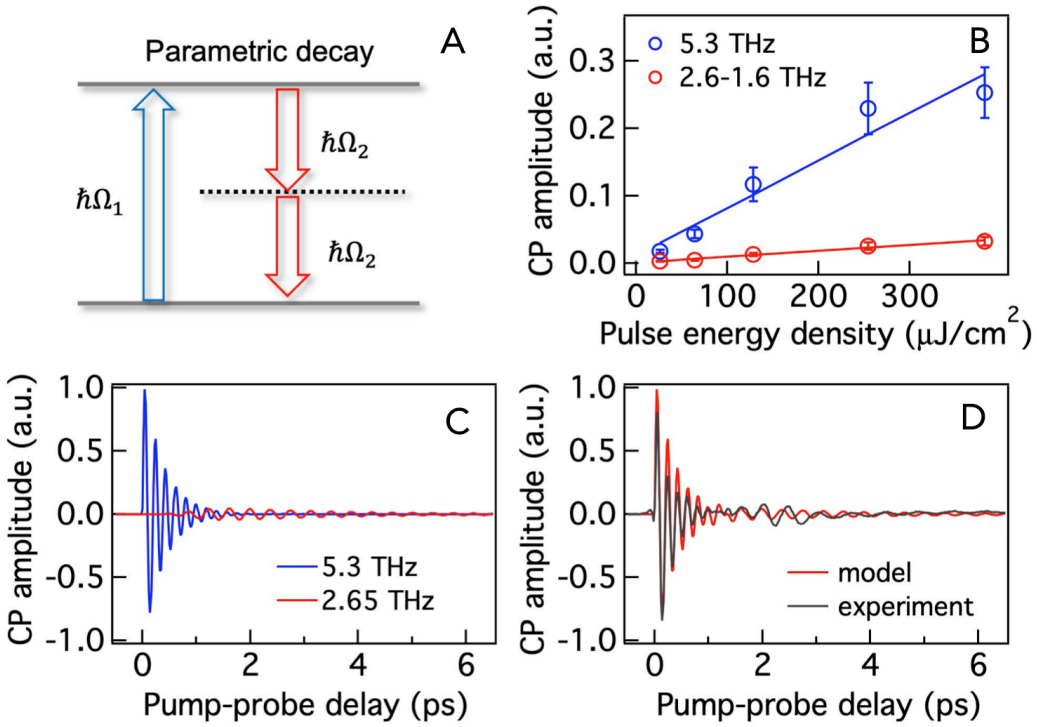

Figure 5.3 Model simulation of coherent phonon-to-phonon transfer and comparison to experiment. A Schematic illustration of parametric decay; **B** Excitation laser power dependence of the coherent phonon amplitudes. Blue-circles: the 5.3 THz mode; red circles: the 2.6-1.6 THz modes. The lines are linear fits. **C** Simulation results from equations (5.2.2) and (5.2.3) of the time-evolution of the 5.3 THz (blue) to 2.65 THz (red) modes. **D** A comparison of simulated coherent phonon oscillations (black) with experimental result from **Figure 5.1** (red).

We simulate this process classically using a driven oscillator model of two coupled coherent phonons. We describe the coupling of the strongly-damped high-frequency mode to a weakly-damped low frequency mode and set the two frequencies to 5.3 THz and 2.65 THz, respectively. In a minimal model of nonlinear phonon coupling, the potential energy V_{ph} of the two coupled oscillators is given by[222,223]:

$$V_{ph} = \frac{\Omega_1^{\,2}}{2} Q_1^{\,2} + \frac{\Omega_2^{\,2}}{2} Q_2^{\,2} + c Q_1 Q_2^{\,2} \qquad (5.2.1)$$

where Q_1 and Q_2 are the normal mode coordinates of the primary driving and secondary target mode, respectively; Ω_1 and Ω_2 are the angular frequencies of the 5.3

THz and the 2.65 THz modes, respectively; c is the linear-quadratic coupling coefficient. The system of coupled differential equations are[223]:

$$\ddot{Q}_1 + \kappa_1 \dot{Q}_1 + {\Omega_1}^2 Q_1 = \alpha E^2(t) + c{Q_2}^2 \quad (5.2.2)$$

$$\ddot{Q}_2 + \kappa_2 \dot{Q}_2 + \left({\Omega_2}^2 + cQ_1\right) Q_2 = 0 \quad (5.2.3)$$

where κ_1 and κ_2 are phenomenological damping coefficients which account for incoherent energy dissipation. We model the excitation of the primary mode via a stimulated Raman scattering process with an effective Raman cross section α and the electric field of the pump laser pulse, $E(t)$; the amplitude of the primary mode is proportional to the laser intensity (F): $Q_1 \propto E^2 \propto I$. The last term in equation (5.2.2), $c{Q_2}^2$, is the back-action of the coupled secondary mode and is negligible due to the strong damping of the primary mode. The cQ_1 term in equation (5.2.3) dynamically modifies the frequency of Q_2, which leads to a parametric resonance at $\Omega_1 = 2\Omega_2$.[221] The amplitude Q_2 is linearly dependent on the amplitude of the parametric drive cQ_1, and therefore we also expect a linear dependence of Q_2 on laser intensity: $Q_2 \propto Q_1 \propto I$. These linear dependences are experimentally confirmed in **Figure 5.3B** (see spectra at different pump pulse energy densities in **Figure 5.6**), which shows the maximum amplitudes of the high- and low-frequency coherent phonons.

Figure 5.3C shows simulation results from the coupled equation of motions, (5.2.2) and (5.2.3), for the coherent conversion of the 5.3 THz mode to the 2.65 THz mode. This model simulation, detailed in Section 5.4.3, qualitatively reproduces the first step in the observed coherent phonon dynamics, as shown by a comparison of simulation to experiments, **Figure 5.3D**. The model does not include the continuous softening in the range of ~2.6-1.6 THz, which gives rise to the phase mismatch

developing with time between model simulation and experiments. Phonon softening may be simulated similarly as further coherent phonon-phonon redistribution from 2.6 to 1.6 THz, corresponding to the range of a dense manifold of Pb-Br-Pb bending modes[49].

The presence of coherence in phonon-to-phonon transfer and softening dictates that the coupling constants among the sub-set of phonons involved must be higher than their coupling to the remaining incoherent phonon bath. Indeed, the model simulation in **Figure 5.3** shows that, in order to account for the experimental results, the linear-quadratic phonon coupling coefficient *c* must be two to four orders of magnitude higher than those in most bulk dielectrics[222]. The giant phonon-phonon coupling constant can be only explained by the extreme anharmonicity of the local lattice environment amplified by polarons that are excited within 150 meV below the bandgap. In contrast, such extreme anharmonicity is absent for normal coherent phonons excited outside the range of polaronic states (**Figure 5.2**).

5.3 Conclusions

The time domain observation of coherent coupling and softening (5.3 → 1.6 THz) among zone-center optical phonon modes presented here is closely related to the energy domain observation of correlation between local LO phonon frequency (3.5→7.0 THz) and polaron pair localization energy (0-150 meV) detailed elsewhere[212]. Both observations reveal the extreme anharmonicity of the lattice environment associated with charge carrier localization in LHPs. In the present study, we witness a parametric down-conversion of a highly distorted local

vibrational state associated with the excited polaron pair to more delocalized normal modes of the ground state lattice. The photo-excited electron-hole pair induces a transient lattice state, which enforces phase coherence among a subset of optical lattice modes through extremely large anharmonic coupling. This imposed lattice coherence is directly observed over a wide frequency range (5.3-1.6 THz) among zero wavevector lattice modes, surviving for more than 7 ps. We interpret this results as a key prerequisite for phonon-wave packet generation leading to ferroelectric large polaron formation beyond the bare Fröhlich interaction[34,212]. The localization of charge carriers in the anharmonic and dynamically disordered LHP lattice dramatically amplifies the local anharmonicity. Our finding demands the development of new polaronic theory, but also suggests a new design principle for high performance semiconductors in optoelectronics from materials with extreme anharmonic phonon responses to the presence of charge carriers.

5.4 Appendix: Supplementary Materials

5.4.1 Experimental Setup

The 800 nm fundamental of a Ti:Sapphire regenerative amplifier (modified KMLabs Wyvern, 10 kHz, 45 fs, 0.8 mJ/pulse) was used as the probe pulse. Narrow-band pump pulses were generated by a homebuilt BBO-based non-collinear optical parametric amplifier (NOPA) as described in Chapter 2. The pump pulse was optimized for a central wavelength of 550 nm or 605 nm, with pulse width of < 25 nm and compressed to sub-30 fs. The pump pulse was modulated by a synchronized 5 kHz chopper wheel. The pump fluence was measured at the sample.

The probe beam was focused to 40 μm on the sample. The pump beam was overlapped on the probe beam's focus with an angle of <5° and focused to 100 μm in order to ensure homogeneous excitation across the probing volume. Both pump and probe were linearly polarized by a broadband thin film polarizer.

5.4.2 Time-Frequency analysis

We conduct time-frequency analysis of coherent oscillations using a short-time Fourier transform (STFT), which is available in MATLAB as a standard function. In STFT, a transient is split into windows of constant width, and a fast Fourier transform (FFT) is applied to each window.[224,225] By specifying window width and overlap, we achieve a time-resolved frequency analysis of the coherent phonon (CP) transient. The specified window sizes are as follows: in **Figure 5.1D**, the window size was 60 and the window overlap was set to 59 (step size: 20 fs). In **Figure 5.2B**, these parameters are 50 and 49, respectively (step size: 40 fs).

5.4.3 Coupled Oscillator Model

In this section, we present a model of coherently coupled phonons to reproduce the temporal shape of the coherent oscillations at 5.3 and 2.65 THz. We describe the coupling of a strongly-damped high-frequency fully-symmetric A_g mode to a weakly-damped low-frequency mode of arbitrary symmetry. Our model is fully consistent with a previously described approach for the parametric coupling of the anharmonic A_g mode in bismuth.[221] The harmonic part of the potential energy of the two phonons, V_h, is given by

$$V_{\mathrm{h}} = \frac{\Omega_1^2}{2} Q_1^2 + \frac{\Omega_2^2}{2} Q_2^2 \tag{5.4.1}$$

where Q_1 and Q_2 are the normal mode coordinates (or amplitudes) of the initial 5.3 THz and the target mode given in $\text{Å}\sqrt{\text{amu}}$, where amu is the atomic mass unit. Ω_1 and Ω_2 are the respective eigenfrequencies given in 2π THz.

Anharmonic coupling between different phonons is allowed, when their product contains the fully symmetric representation of the system, which, for orthorhombic $CsPbBr_3$, is the A_g representation. For a coherently-excited A_g mode, this leaves nonlinear coupling terms of the type

$$V_{\mathrm{nl}} = c Q_1 Q_2^2 \tag{5.4.2}$$

in cubic order of the phonon amplitude, where $Q_1 \equiv Q_{A_g}$, and c is the linear-quadratic coupling coefficient given in $\text{eV}/(\text{Å}\sqrt{\text{amu}})^3$. This is fundamentally different from the nonlinear phonon couplings that have been intensively studied in recent years in the context of ionic Raman scattering, in which a coherently-excited infrared (IR)-active phonon scatters by a Raman (R)-active phonon. This type of interaction is described by a quadratic-linear $Q_{\mathrm{IR}}^2 Q_{\mathrm{R}}$ [222,226] or trilinear $Q_{\mathrm{IR},1} Q_{\mathrm{IR},2} Q_{\mathrm{R}}$ [227] coupling and cannot be used to reproduce the temporal signal obtained in this work.

We model the excitation of the initial mode via a stimulated Raman scattering process, which can be described by the potential

$$V_{\mathrm{R}} = \varepsilon_0 R Q_1 E^2(t) \tag{5.4.3}$$

where ε_0 is the static dielectric constant, R is the frequency-dependent Raman tensor of the A_g mode, and $E(t)$ is the electric field of the incoming laser pulse. $E(t)$ can be modeled as $E(t) = E_0 \exp\{-(t-t_0)^2/[2(\tau/\sqrt{8\ln 2})^2]\} \cos(\omega_0 t + \phi_{\mathrm{CEP}})$, where τ

is the full width at half maximum pulse duration, ω_0 is the frequency of the laser pulse, and the carrier-envelope phase ϕ_{CEP} can be chosen to be zero without loss of generality[223] The resulting system of coupled differential equations is

$$(4.\ddot{Q}_1 + \kappa_1\dot{Q}_1 + \Omega_1^2 Q_1 = \varepsilon_0 R E^2(t) + cQ_2^2 \tag{5.4.4}$$

$$\ddot{Q}_2 + \kappa_2\dot{Q}_2 + (\Omega_2^2 + cQ_1)Q_2 = 0. \tag{5.4.5}$$

Here, κ_1 and κ_2 are the damping coefficients of the initial and the target mode, respectively. As the intial mode is excited via stimulated Raman scattering, its amplitude depends on the square of the electric field, which is proportional to the fluence F: $Q_1 \propto E^2 \propto F$. The cQ_2^2 term in equation (5.4.4) is the back-action of the coupled target mode, which can be assumed to be negligible due to the strong damping of the initial mode. The cQ_1 term in equation (5.4.5) dynamically modifies the frequency of the secondary (Q_2) mode, and for a resonance condition $\Omega_1 = 2\,\Omega_2$, the secondary mode gets excited through parametric amplification.[221] The amplitude Q_2 is linearly dependent on the amplitude of the parametric drive cQ_1, and therefore we expect a linear dependence on the fluence: $Q_2 \propto Q_1 \propto F$. We list the parameters that we used for equations (5.4.4) and (5.4.5) in **Table 5.1**. Note that, in order to reproduce the temporal signal through nonlinear phonon coupling, the value of the coupling coefficient that we assume here ($\approx$ eV/(Å$\sqrt{\text{amu}}$)^3) is two to four orders of magnitude higher than common values found in bulk dielectrics ($\approx$ meV/(Å$\sqrt{\text{amu}}$)^3)[222]. This emphasizes the importance of the existence of local polar nanodomains, in which the coupling strength may potentially be stronger than in the average lattice ground state.

$\frac{\Omega_1}{2\pi}$	5.3 THz
$\frac{\Omega_2}{2\pi}$	2.65 THz
κ_1	5.3 THz
κ_2	0.75 THz
R	$100\ \text{Å}^2/\sqrt{\text{amu}}$
c	$17\ \text{eV}/(\text{Å}^2\sqrt{\text{amu}})^3$
E_0	10 MV/cm
ω	550 nm
τ	10 fs

Table 5.1 Parameters used in the evaluation of equations (5.4.4) and (5.4.5).

5.4.4 Figures and Extended Data

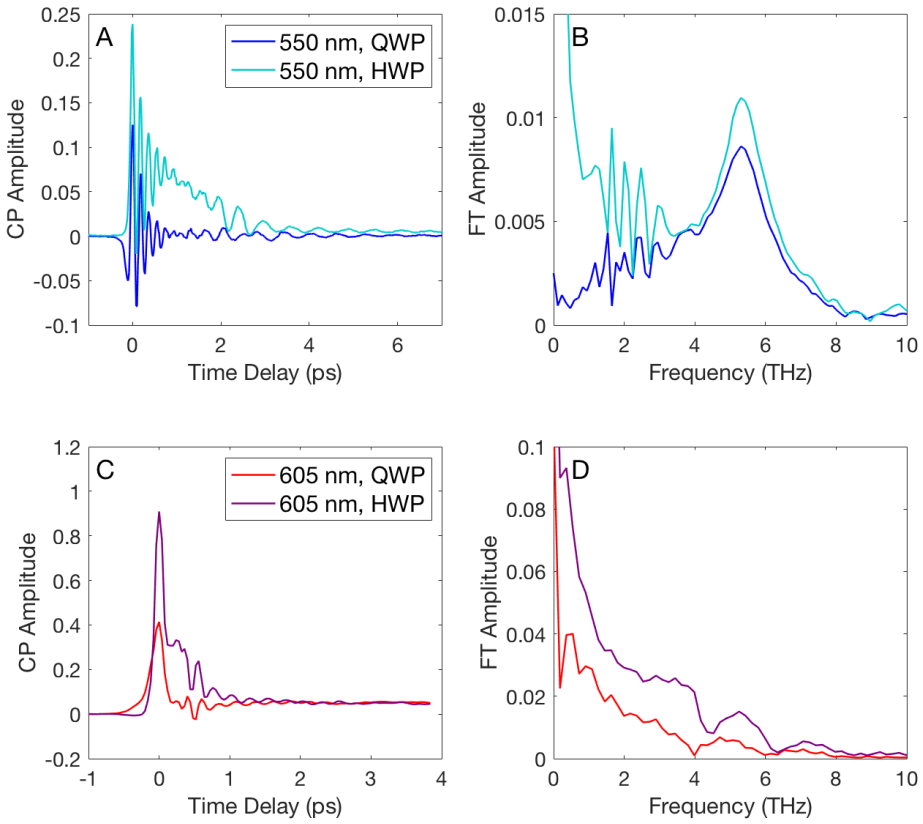

Figure 5.4 Comparison of linear and circular birefringence A, **B** The raw data taken with pump excitation of 550 nm, 0.15 mW. **C**, **D** The raw data taken with pump excitation of 605 nm, 0.35 mW. The trace taken with the quarter waveplate (QWP), shown in dark blue and red, shows the pump-induced change in probe ellipticity. The trace taken with the half waveplate (HWP), shown in light blue and purple, shows the pump-induced change in linear polarization of the probe. In these experiments, the coherent features are visible in traces from both the HWP and QWP. As expected in coherent phonon spectroscopy, the linear and circular birefringence are modulated in the same way by the coherent phonon. The electronic Kerr effect leads to a different response in only the incoherent part of the signal.

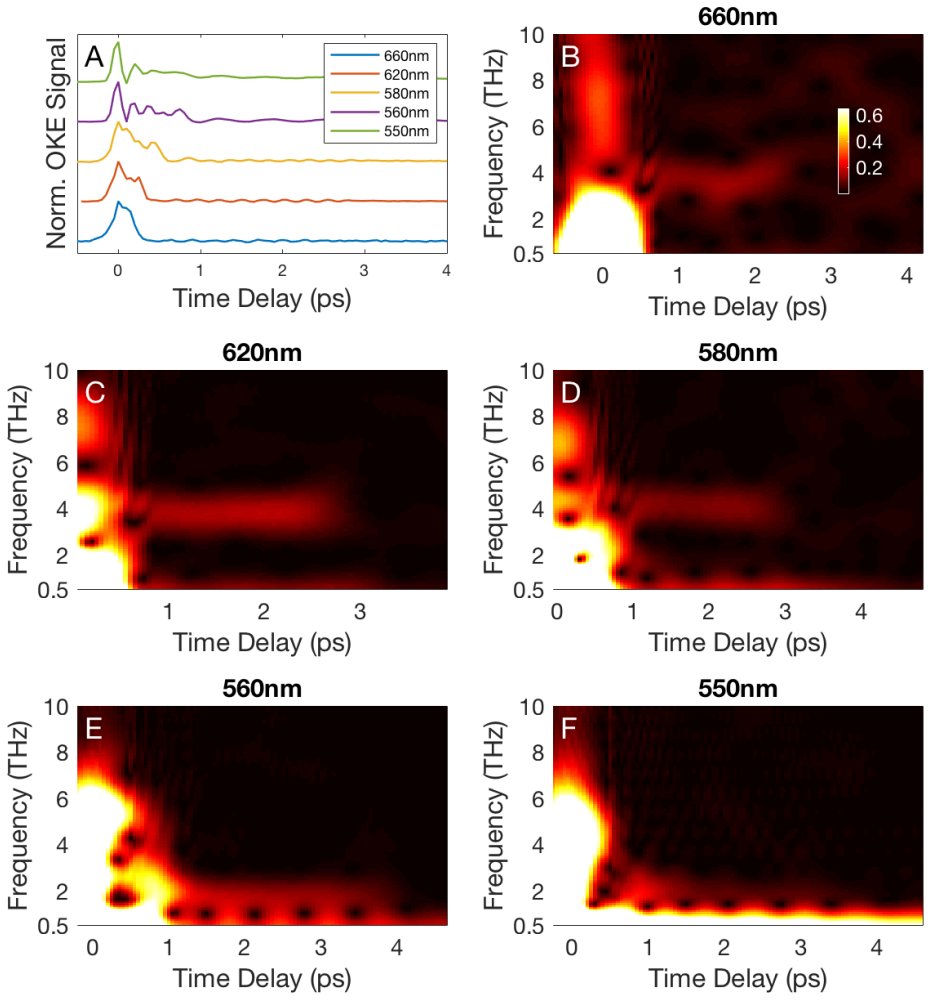

Figure 5.5 Time-frequency analysis for different pump excitation wavelengths. A OKE transients previously reported by Miyata and coworkers for pump excitation wavelengths of 660 nm (1.88 eV), 620 nm (2.00 eV), 580 nm (2.14 eV), 560 nm (2.21 eV), and 550 nm (2.25 eV)[49]. These data sets are from different $CsPbBr_3$ samples and are taken with a different experimental setup, in which the anisotropic polarization change is detected by the pump-induced change in intensity of a cross-polarized 800 nm probe. The respective short-time Fourier transform analyses are shown in **B** – **F**. This analysis is described Section 5.4.2. We see that the coherent coupling and softening of phonons arises only as the pump excitation energy approaches the bandgap energy, confirming that this extreme anharmonic behavior is only observed in the presence of photoexcited charge carriers.

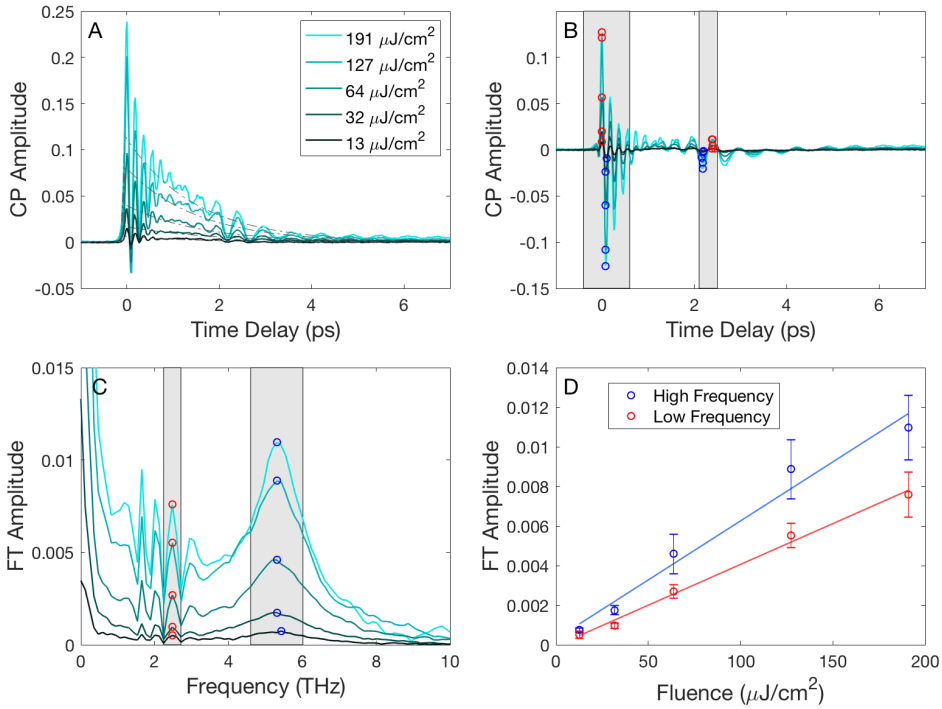

Figure 5.6 Fluence-dependent CPS traces with 550 nm pump excitation. A The raw data taken with pump fluences of 191, 127, 64, 32, and 13 μJ/cm^2. The incoherent contribution is shown with gray-broken traces (single-exponential decay). **B** The coherent contribution to the CPS trace, taken by subtracting the incoherent part in **A** from the respective raw trace. The gray shaded regions indicate areas in which the high-frequency and low-frequency phonon contributions are separated. The red markers indicate the maximum in the gray shaded regions, the blue markers indicate the minimum in the same regions. The phonon amplitude used in **Figure 5.3** is calculated by taking the difference between the respective maxima and minima (peak to peak) for each phonon frequency for each trace. **C** The Fourier transform (FT) of the raw data shown in **A**. The blue and red markers indicate the maximum FT amplitude of the respective gray shaded regions. D The maxima of the phonon peaks in C plotted against pump power. As shown, both the higher frequency and lower frequency phonons scale linearly with fluence. This agrees very well with the linear fits shown in **Figure 5.3.**

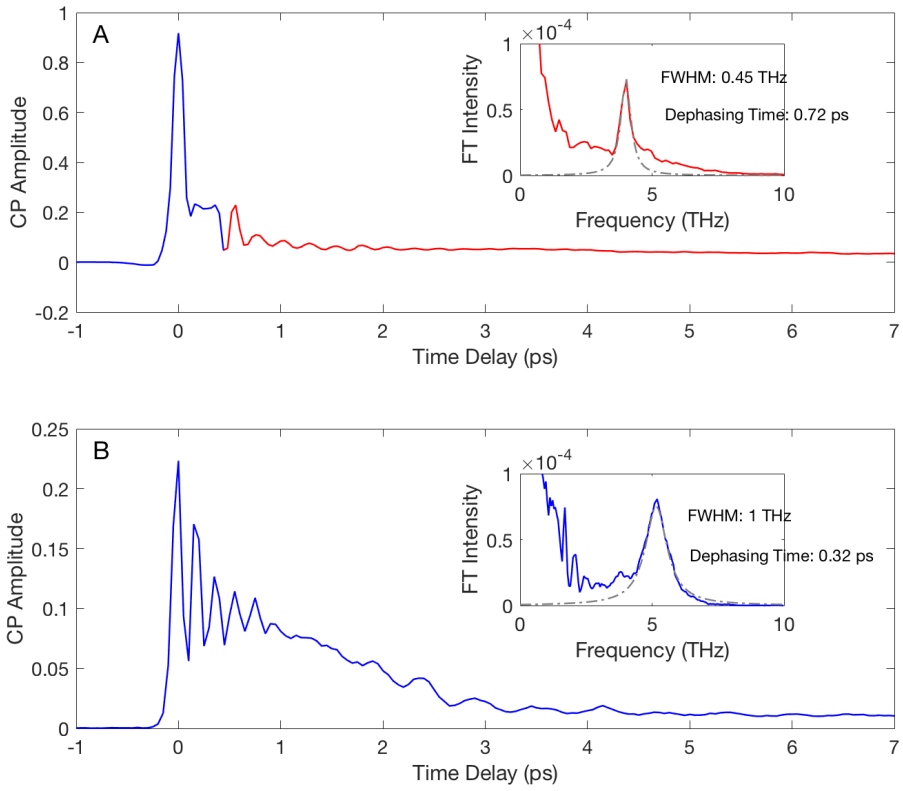

Figure 5.7 Dephasing times for coherent phonons. Here, we fit a Lorentzian to the phonon peaks in the Fourier Transform (FT) intensity. The dephasing time is given by $(\pi * FWHM)^{-1}$ where the full-width half maximum (FWHM) of the Lorentzian fit is in THz. **A** The CP signal when the pump wavelength is 605 nm. Here, we take the FT of the coherent oscillations, which are shown by the red trace. The inset shows the intensity of the FT of this region. Fitting a Lorentzian to the peak at 4 THz yields a FWHM of 0.45 THz and a dephasing time of 0.72 ps. **B** The CPS transient when the pump wavelength is 550 nm. We show the square of the FFT of the entire transient. Fitting a Lorentzian to the peak at 5.3 THz yields a FWHM of 1 THz and a dephasing time of 0.32 ps.

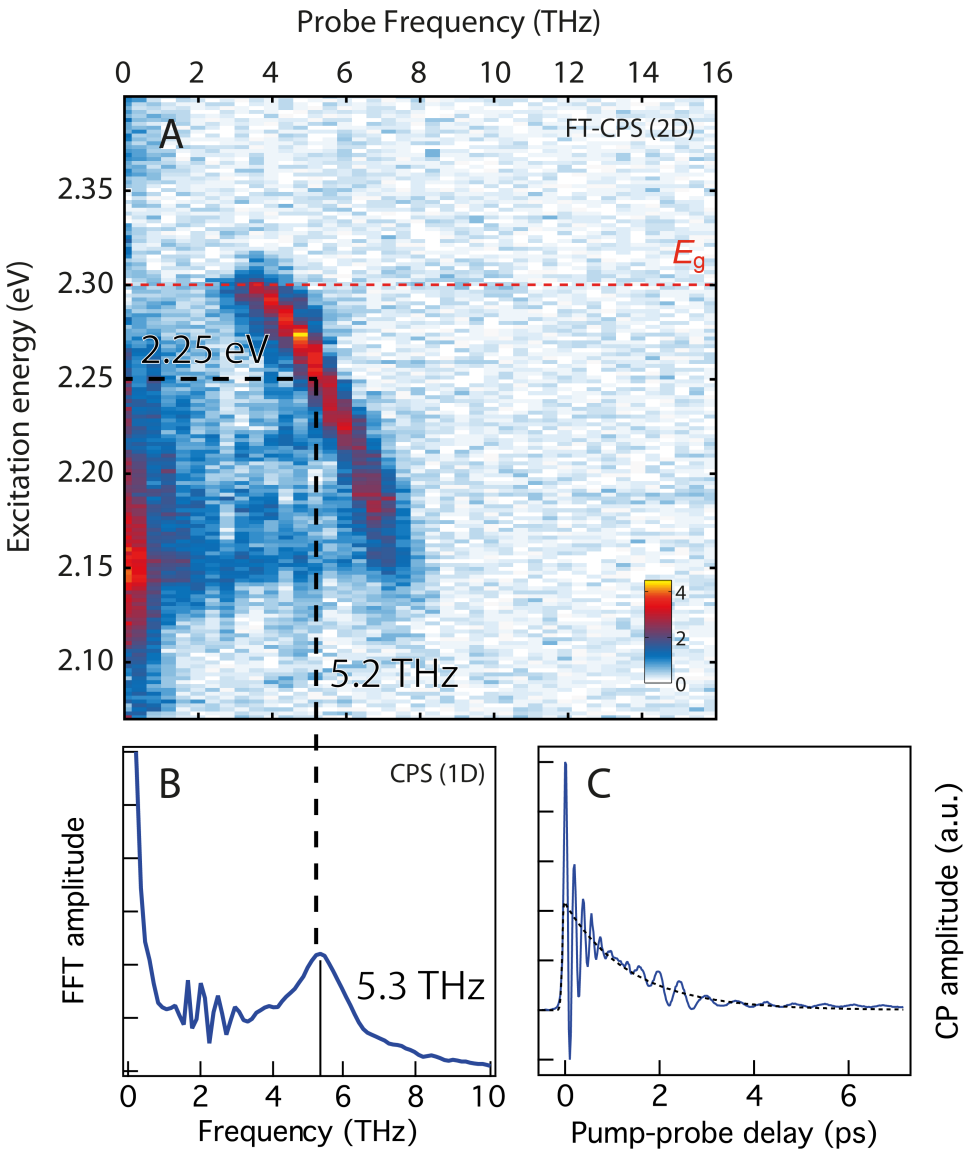

Figure 5.8 Comparison of Coherent Phonon Spectroscopy and Fourier-Transform Coherent Phonon Spectroscopy (FT-CPS). A The pump-energy resolved Fourier transform of FT-CPS on $CsPbBr_3$ (**Figure 6.2**). As the pump excitation energy decreases from the bandgap (E_g) , 2.30 eV, to 150 meV below the bandgap, the initial phonon hardens with decreasing excitation energy from 3.5 THz to 7.0 THz. The dotted line indicates that at an excitation energy of 2.25 eV the corresponding phonon frequency is 5.2 THz. **B, C** The static Fourier transform and the one-dimensional CP trace of $CsPbBr_3$ excited at 2.25 eV. The initial high-frequency phonon in c corresponds to the broad peak centered at 5.3 THz in **B**. Note that **A** and **B** share a frequency axis, and the close match between the dotted line (5.2 THz) and the solid line (5.3 THz) emphasizes the agreement between FT-CPS and 1D CPS.

6 Ferroelectric Charge Localization

Adapted with permission from:

Maehrlein, S. F.*; **Joshi, P. P.***; Wang, F.; Juraschek, D. M.; Cherasse, M.; Zhu, X.-Y. Spectroscopic Signatures for Ferroelectric Charge Localization in Lead Halide Perovskites. *Submitted.*

*indicates equal author contribution

Discussed experiments were conducted by Sebastian F. Maehrlein and myself. Single crystals were grown by Feifan Wang.

Abstract

The high efficiencies of solar cells and light emitting devices from lead halide perovskites (LHPs) are direct consequences of the long carrier diffusion lengths and lifetimes. A number of mechanistic proposals have been put forward to explain the origins of such carrier properties in a dynamically disordered lattice. Prominent among them are 1) electron-hole pair separation in real space on a dynamic landscape of ferroelectric polar nanodomains[114,209–211]; 2) efficient screening of charge carriers in large polaron formation[20,49,103,104,112,113,228]; and 3) electron-hole pair separation in momentum space from a dynamic Rashba effect[97–100]. While these proposals have enjoyed success in explaining various aspects of carrier properties in LHPs, their experimental verifications have eluded researchers to date. Here we develop Fourier transform coherent phonon spectroscopy to directly probe charge localization in LHPs. We selectively excite the below-gap states and probe their local environments by coupled coherent phonons. In single crystal $CsPbBr_3$ at room temperature, the total electron and hole localization energy, E_b, varies continuously in the energy range of 0-150 meV. The magnitude of E_b, and, thus, the extent of

charge localization, is correlated with a dramatic increase in the coherent lattice response frequency ν_{pb}, from 3.5±0.2 THz for nearly free carriers at the bandgap to 7.0±0.2 THz for the most localized states at E_b = 150±20 meV. These results reflect the strong anharmonicity of lattice vibrations coupled to localized charges. Modification of an anharmonic potential, as exemplified by a ferroelectric double well from local symmetry breaking[79,229], by the electric field from a spatially separated electron-hole pair can explain the correlation between E_b and ν_{pb}. Similar below gap states are observed for $CH_3NH_3PbBr_3$. These findings provide spectroscopic signatures of charge localization in LHPs by dynamic ferroelectric nanodomains, i.e., ferroelectric large polarons.

6.1 Introduction

There are two characters central to all three mechanistic proposals discussed above for LHPs: 1) dynamic symmetry breaking and 2) formation of below-gap states. Dynamic symmetry breaking can result in polarization of the unit cell and the polarization vectors, i.e., local dipoles, can transiently order to form polar nano domains (PNDs)[60,79,229]. In the ferroelectric proposal, the electron and the hole are dynamically localized to spatially distinct PND boundaries[209–211]. In the large polaron proposal, each charge carrier is screened by induced polarization of the lattice[20,49,103,104,112], but local ferroelectric ordering may enhance the screening effect[34]. In the dynamic Rashba proposal[99], the PNDs provide the local field necessary for band splitting in momentum space. While earlier proposals suggested local dipoles originating from the organic cations, the current consensus is that the dipoles result

mainly from polarization of the LHP unit cell, irrespective of the cation type[60,79,229]. The second character is the formation of below gap states from ferroelectric[114,209–211] and/or polaronic[34,49,220] localization of charge carriers. Here we consider electron/hole localization, not exciton localization, since excitons are mostly dissociated at room temperature in LHPs because dynamic screening lowers the exciton binding energies to below kT[50,52]. Below gap states have also been attributed to the emission or absorption of phonons in the optical transition between momentum indirect states from the dynamic Rashba effect[230].

Spectroscopic verifications of carrier localization mechanisms in LHPs have been elusive because the below-gap states possess weak optical transition strength and are overwhelmed by at- or above-gap transitions. Moreover, it is not clear how local lattice environments specific to below-gap states can give rise to spectroscopic signatures. To overcome these difficulties, we develop Fourier transform coherent phonon spectroscopy (FT-CPS) for energy-resolved excitation of below-gap states and probing of coupled coherent lattice vibrations of the local environment. Our group has applied time-resolved optical Kerr effect (TR-OKE) spectroscopy to establish phonon disorder[20] and dynamic response of phonons to charge injection from above-gap excitation in LHPs[49]. TR-OKE spectroscopy revealed complex phonon activity which is sensitive to pump photon energy below the bandgap, but the intrinsic bandwidth of femtosecond laser pulses prohibited a quantitative analysis[49]. This has necessitated the development of a two-dimensional variation of TR-OKE, which we call FT-CPS, to provide high pump-energy resolution without compromising time resolution. This approach is related to the two-dimensional

electronic-vibration spectroscopy of Fleming and coworkers[231] and the pump-pump-probe phonon spectroscopy of Nelson and coworkers[232].

6.2 Results and Discussion

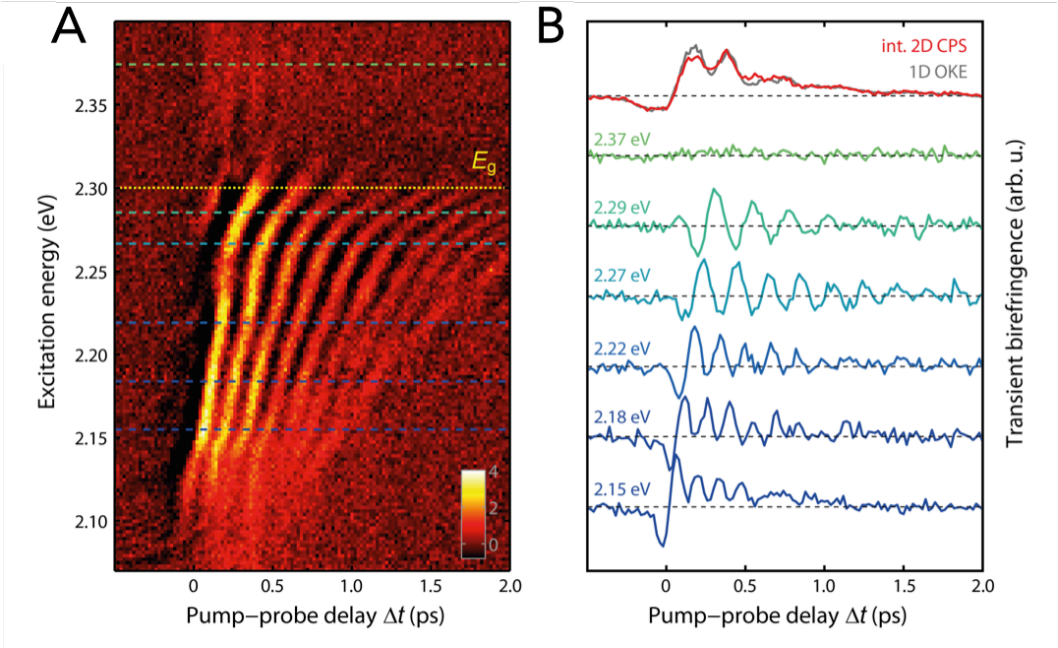

Figure 6.1 Fourier-transform coherent phonon spectra (FT-CPS) from $CsPbBr_3$. A Pseudo-color (transient birefringence) 2D plot of FT-CP spectra from a CsPbBr3 single crystal at 295 K. The excitation energy (Eex) comes from Fourier-transform along the time delay (t) between the two coherent pulses. The positions of the estimated bandgap (Eg) and selected Eex values for horizontal cuts (panel **B**) in the 2D spectra are shown as dashed lines. In addition to the horizonal cuts (blue to green), shown in **B** are single pulse excitation (1D) spectrum (gray) and E_{ex}-integrated 2D spectrum (red).

All experiments are carried out at 295 K on single crystal CsPbBr3 and CH3NH3PbBr3 (see **Figure 0.1**) in inert atmosphere. We implement FT-CPS using a pulse shaper (PhaseTech, Madison) as detailed in Chapter 3. Briefly, a femtosecond laser pulse ($h\nu_1$= 2.25 eV, 27 fs pulse width, 10 kHz) is sent through the pulse shaper to generate two collinearly polarized pulses with precisely controlled time

delay (t) and controllable phase difference. The two coherent pulses induce a polarization oscillating at distinct frequencies depending on t and the resulting anisotropy in refractive index is detected at a variable time delay (Δt) by a transmitted probe pulse ($h\nu_2$ = 1.55 eV, 45 fs pulse width, 10 kHz) in the electro-optic sampling configuration, which enables the observation of coherent phonons of longitudinal optical (LO) modes[233]. We implement rotating frame[158], phase cycling[158], and balanced detection to optimize signal-to-noise ratio and eliminate incoherent contributions to the signal (see Methods). Fourier transform with respect to pump-pump delay t yields high resolution in excitation energy (E_{ex}).

Figure 6.1A shows a FT-CPS spectrum from $CsPbBr_3$, with the real part (pseudo color) of Fourier transform plotted against Δt and E_{ex} (see **Figure 6.5** for 2D time-time domain data). Prominent in the spectra are oscillatory features, as most evident in line cuts for selected E_{ex} in **Figure 6.1A**. The frequencies of the oscillatory features are in the THz region and are attributed to transient birefringence modulated by coherent phonons (see Chapter 3). There are two distinct features associated with the appearance of these spectral features: 1) these coherent phonons are only excited in a limited energy range, E_{ex} = ~2.30-2.15 eV. The high energy limit is close to the photon energy where the $CsPbBr_3$ sample is no longer transparent and it coincides with the bandgap E_g (=2.30±0.03 eV)[172]; and 2) the frequency of the coherent phonon increases as excitation energy E_{ex} decreases. In addition, there is an increasing offset on top of the oscillatory features in CP signal as Eex decreases, which cannot be related to electronic absorption effect; the latter should increase with Eex and is also eliminated by phase cycling. This is consistent with a displacive mechanism for coherent phonon generation, as detailed below. To illustrate the

importance of the FT-CPS (2D) implementation in resolving the E_{ex} dependent coherent phonons, we also show in **Figure 6.1B** a single pulse excitation (1D) CP trace (grey), which has been detailed before in TR-OKE experiments[49]. The 1D-CP trace is in excellent agreement with the Eex-integrated spectrum (red) from 2D data in **Figure 6.1A.** The superposition of coherent phonon signals with different frequencies at different E_{ex} results in fast dephasing of the 1D-CP signal.

To highlight the strong correlation between electronic excitation energy (E_{ex}) and coherent phonon frequency (ν_{ph}), we Fourier transform with respect to the pump-probe delay (Δt) in **Figure 6.1A** to give **Figure 6.2**, which shows the 2D FFT intensity as functions of E_{ex} and ν_{ph}. The anti-correlation between ν_{ph} and E_{ex} is represented by a nearly linear relationship: ν_{ph} increases from 3.5±0.2 THz to 7.0±0.2 THz as E_{ex} decreases from 2.30 eV to 2.15 eV. Such a strong influence of the excitation energy on the phonon frequency is unprecedented in coherent phonon spectroscopy[233–235]. The observed ν_{ph} at the low frequency limit (3.5±0.2 THz) for excitation at the bandgap is in the range for LO phonons of the Pb-Br-Pb stretching modes[49,220,236,237]. The higher ν_{ph} in the 4.5-7.0 THz range is surprisingly outside the range of phonon bands in $CsPbBr_3$.[49,238] We found a quantitative agreement of this frequency shift across different samples (see e.g. **Figure 6.7** and **Figure 6.8** in Section 6.4.3) and also by detecting elliptic transient birefringence (**Figure 6.9**).

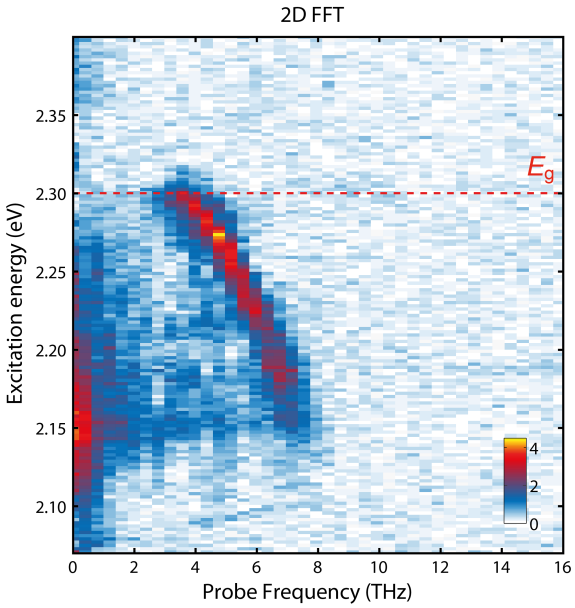

Figure 6.2 Correlation between excitation energy and coherent phonon frequency. The 2D pseudo-color plot obtained from the Fourier transform (FFT) with respect to Δt from the FT-CP spectra in **Figure 6.1B**. The color scale is the FFT amplitude.

In contrast to the extraordinary increase in phonon frequency, the total electron and hole stabilization energy, $E_b = E_g - E_{ex}$ (0-150 meV) is in agreement with reported values for carrier localization below the bandgap. Wu et al. analyzed the tail states in the optical spectra of three $APbBr_3$ [A = Cs+, $CH_3NH_3^+$, or $CH(NH_2)_2^+$] perovskite single crystals and showed stabilization energies of 120-140 meV below E_g at room temperature[230]. Guo et al. analyzed the temperature dependent absorption and emission spectra from $CsPbBr_3$ and $CH_3NH_3PbBr_3$ single crystals[220]. They attributed the Stokes shifts (~50-60 meV peak-to-peak, ≥ 100 meV for low energy emission tails) to the solvation like response of charge carriers by an effective LO phonon mode at ~20 meV (4.8 THz) in the anharmonic and disordered phonon environment.

Based on the two facts that the observed coherent phonons are excited below the bandgap and the resulting frequencies are shifted outside the normal phonon range for $CsPbBr_3$, we assign the observed coherent phonons to local polar structural dynamics initiated by the localized charge carriers. The correlation between E_{ex} and ν_{ph} can be explained by carrier localization in the presence of PNDs. Both the ferroelectric proposal[114,209–211] and the large polaron proposal[49,239] predict localization of an electron (e) and a hole (h) to spatially distinct regions in an LHP crystal. These two proposals are consolidated in the ferroelectric large polaron model where a charge is stabilized both by induced polarization and transiently formed polarization on the fluctuation potential landscape[34]; this proposal has also received support from scanning tunneling microscopy imaging[240]. A charge separated e-h pair or, more precisely, a polaron pair can be formed dynamically from the localization of free carriers generated by an initial optical excitation at or above the bandgap[49,239]. Alternatively, on a fluctuating lattice landscape in an LHP crystal, below gap optical excitation can selectively excite localized e-h pair states with specific charge stabilization energy under the corresponding resonant condition. Such below gap excitation has been observed in both 3D LHPs[230,241] and 2D LHPs[242]. In an LHP crystal with local symmetry breaking and thus local polarization, the dynamic fluctuation of PNDs can be described by a double-well potential, as is well known in the Landau theory for ferroelectric phase transitions[243]. Such a double well potential has been confirmed in calculations for $CH_3NH_3PbI_3$ and $CsPbI_3$ perovskites[79,229]. A key property of an anharmonic potential is the sensitivity of eigen frequency to the addition of a linear term, $-\overrightarrow{E_e} \cdot \vec{P}$, where $\vec{P}$ is the polarization vector and $\overrightarrow{E_e}$ is an extra electric field. In contrast, the addition of this linear term to a harmonic

potential ($\propto P^2$) only shifts the potential minimum, with negligible effect on the eigen frequency. The combination of the ferroelectric-like anharmonic potential and a local electric field from the charge separated/localized below-gap states can explain the correlation between ν_{ph} and E_{ex}.

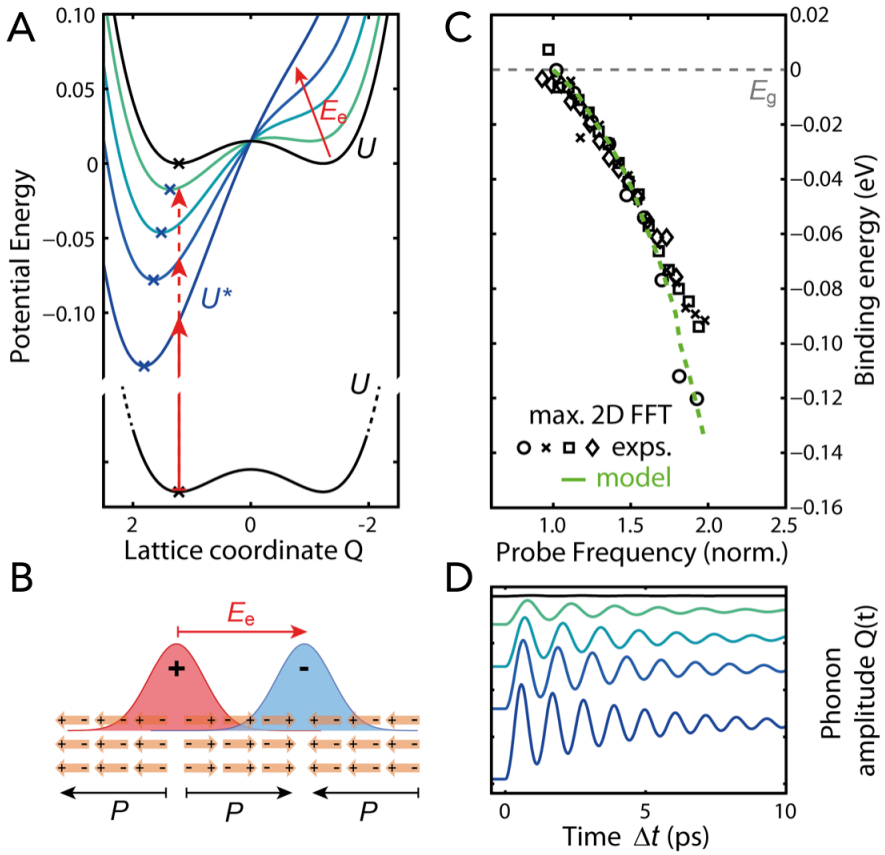

Figure 6.3 Model shows the correlation between the binding energy of ferroelectric potential and phonon frequency. A Generic Landau potentials for the ferroelectric double well in the ground state (U) and excited state (U^*). In the latter, the different extents of distortion (black→ green → blue) correspond to linearly increasing electric fields (E_e) from the charge pair separated at ferroelectric domain boundaries, as illustrated in **B**. **C** A comparison of model simulation result (green dashed curve) with four experimental data sets (black markers) from FT-CPS of three different $CsPbBr_3$ crystals. The phonon frequency is normalized to that at zero binding energy, i.e., free carriers with across E_g excitation. **D** Simulated coherent phonon oscillations for the five U^* curves in **A**, vertically offset for clearer visibility.

Figure 6.3A illustrates a double well potential from local symmetry breaking. Here we adopt a minimal Landau potential[243] (black curve), $U(P) = -\frac{\alpha}{2}P^2 + \frac{\gamma}{4}P^4$,

as a function of polarization, *P*. This double well potential is similar to those calculated for $CH_3NH_3PbI_3$ and $CsPbI_3$ perovskites[79,229]. In $CsPbI_3$, the unit cell polarization (*P*) is described by the relative displacement motion of Cs^+ cation from the I^- anions[79]. In electronic excited state for the charge separated and localized polaron pair, the lattice potential can be distorted by the switching-on of an additional electric field ($\overrightarrow{E_e}$) to $U^*(P, E_e) = -\frac{\alpha}{2}P^2 + \frac{\gamma}{4}P^4 - \overrightarrow{E_e} \cdot \vec{P}$. This distortion lowers the energy minimum and increases the steepness (and thus the eigen frequency) of the potential. As illustrated in **Figure 6.3B**, the local electric field in the excited state can come from e-h separation to two opposite boundaries of a PNDs[34,209–211,240]. The extent of charge separation gives different magnitudes of $\overrightarrow{E_e}$. The direction of $\overrightarrow{E_e}$ is determined by the PND boundaries and therefore is always unidirectional to $\vec{P}$, independent of the absolute orientation of the PND. Thus, the excited potentials $U^*(P, E_e) = U^*(-P, -E_e)$ of two oppositely orientated PNDs do not cancel out. We solve the resulting equation of motion following vertical transition from $U(P)$ to $U^*(P)$ for $P(Q) = ZQ$, where Z is the Born effective charge of the local polar mode and Q is a local phonon coordinate. Details on the simulation and parameters used can be found in Chapter 3 and **Figure 6.10**. The simulation results, green curve in **Figure 6.3C**, indeed show the correlation between Eb and nph, in agreement with what is observe in FT-CPS for CsPbBr3 in 3 different samples (black markers, see also **Figure 6.11**). Moreover, the below-gap and vertical optical transition from an un-distorted double well to a distorted one initiates the displacive excitation of the coherent phonon. Since a higher E_b corresponds to more displacement of the potential minimum, this mechanism yields

also a higher offset on top of the coherent oscillation, as shown by simulation results in **Figure 6.3D**, corresponding to the different potentials U* in **Figure 6.3A**. This further agreement with the experimental results in **Figure 6.1B** confirms the dominant displacive nature of the coherent phonon generation for large E_b[233,234,244]. Note that, in the electronic ground state, projection of the PND's polarization vector to the Pb-Br-Pb stretching mode is much smaller than that to the bending mode[79]. Although these experiments cannot directly identify the type of structural distortion, contribution by the stretching mode should increase for an excited e-h polaron pair, as both experiments and theory showed the dominance of lead-halide stretching mode in electron-phonon coupling[220,236,237,245]. Note that anharmonicity specific to lattice environment of a localized charge is usually not captured in DFT calculations.

We also carry out FT-CPS measurements for the hybrid MAPbBr3 perovskite crystal, **Figure 6.4**. Similar to CsPbBr3, we observe enhanced lattice response for excitation within ~100 meV below the bandgap. Since the lattice exhibits much higher anharmonic coupling in $MAPbBr_3$ than that in $CsPbBr_3$ at room temperature[49,176], the coherent phonons from such below-gap excitation are over-damped. As a result, we are seeing an over-damped local lattice response instead of coherent oscillations. In CsPbBr3, **Figure 6.1A** and **Figure 6.1B,** the dephasing rate decreases with increasing excitation energy E_{ex} as reflected in the longer-lived coherent phonon signal as E_{ex} approaches the bandgap. Despite the overdamping in $MAPbBr_3$, we observe an extension of spectral feature to longer Δt at higher E_{ex}, **Figure 6.4**, similar to the results in **Figure 6.1A** and **Figure 6.1B** for $CsPbBr_3$. The interpretation of ferroelectric charge localization likely applies to both.

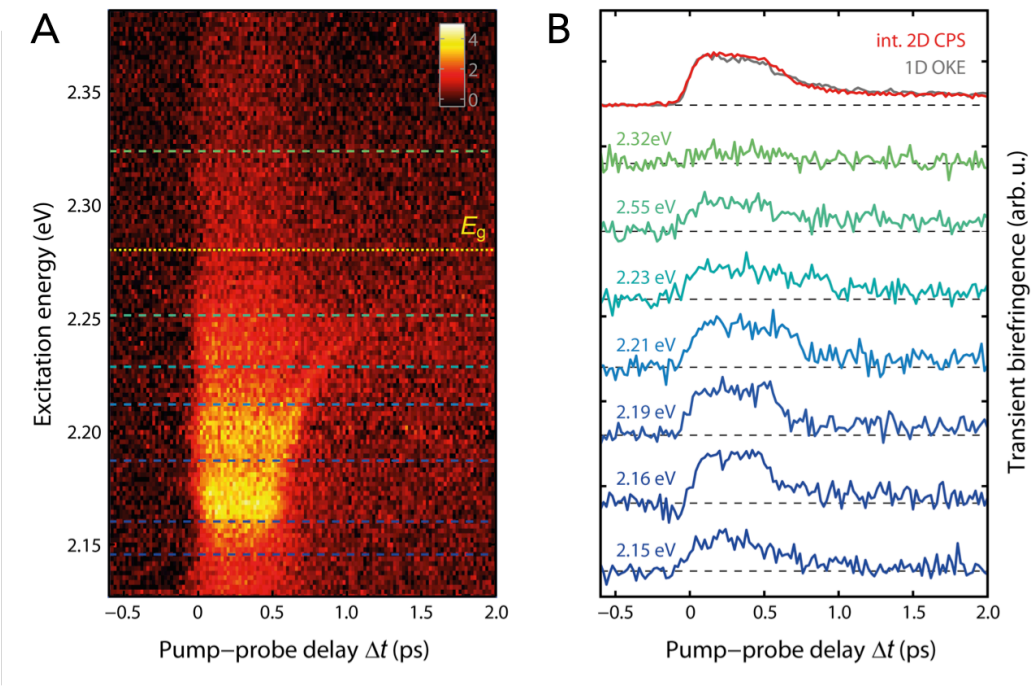

Figure 6.4 FT-CP spectra from $CH_3NH_3PbBr_3$. **A** Pseudo-color (transient birefringence) 2D plot of FT-CP spectra from a $CH_3NH_3PbBr_3$ single crystal at 295 K. The positions of the estimated bandgap (E_g) and selected E_{ex} values for horizontal cuts (panel **B**) in the 2D spectra are shown as dashed lines. In addition to the horizonal cuts (blue to green), shown in **B** are 1D spectrum (gray) and E_{ex}-integrated 2D spectrum (red).

6.3 Conclusions

In summary, we develop electronic state specific Fourier transform coherent phonon spectroscopy to optically excite the below-gap states and probe their local phonon response in $CsPbBr_3$ at room temperature. These experiments show a strong correlation between carrier localization energy (E_b = 0-150 meV) and coupled polar modes with local phonon frequencies ranging from 3.5 to 7.0 THz. We take this as spectroscopic signature for the much-discussed mechanisms in LHPs of charge carrier separation and localization dynamically at fluctuating PND boundaries, as consolidated in the ferroelectric large polaron model[34]. This can be seen as the dynamic counterpart to the known charge carrier trapping at static domain

boundaries in oxide perovskite based ferroelectric materials[246,247]. Our findings reveal the central role of local symmetry breaking and the resulting ferroelectric-like lattice dynamics in charge carrier screening and localization. Compared to a free band electron or hole, such a partially screened and localized charge is expected to possess reduced scattering with other charge carriers, with charged defects, and with the residual optical phonon bath, albeit at the expense of mobility. This suggests a design principle of high-performance semiconductors for optoelectronics from materials with phonon-disorder and ferroelectric-like dielectric responses.

6.4 Appendix: Supplementary Materials

6.4.1 Model Potential

We modeled the local anharmonic equilibrium lattice potential U under two assumptions. First, in the unperturbed state we accounted for lattice anharmonicities[79,229] by adding the lowest order nonlinear term, namely a quartic term $\sim Q^4$ in the phonon coordinate Q. Without loss of generality, we can restrict our model to polar modes with Born effective charge $Z = \frac{\partial P}{\partial Q}$. This first assumption of polar mode in a nonlinear lattice potential directly leads to a Gibb's free energy potential $U(P)$ as known from the Landau theory of phase transitions[92,243,248]:

$$U(P) = \frac{\alpha'}{2} P^2 + \frac{\gamma}{4} P^4 \tag{6.4.1}$$

where the coefficient γ is always positive and determines the anharmonicity. In the Landau-Devonshire theory for second order phase transitions, the sign of the harmonic coefficient $\alpha' \propto (T - T_0)$ is temperature dependent and determines the ferroelectric or paraelectric order for temperatures T above and below the Curie

temperature T_0, respectively[92]. As we assign the coherent lattice vibrations to local modes of the PNDs, as a second assumption, we assume a local ferroelectric order[211,249]. Therefore, the free energy $U(P)$ must exhibit a double well potential and thus, $\alpha' = -\alpha < 0$. Due to the known local polar fluctuations[60,79,229], the barrier height of the double well U_d must be smaller than the room temperature thermal energy kT. Besides this limitation ($U_d \leq 25\ \mathrm{meV}$), U_d is treated as a free scaling factor in our model.

In order to estimate the excited potential energy U^* for a complicated local vibrational mode associated with a PND in the presence of excited charge carriers, we motivate the following approximation: As already discussed by Cho et al. in 1990, the excitation of coherent LO-phonons (detected in electrooptic sampling configuration) can be seen as initiated by an instantaneous electric field resulting from charge separated photocarriers[233]. In the case of dilute excitation of photoexcited carriers in LHPs, electrons and holes spatially separate to opposite ferroelectric domain boundaries[209–211,249]. In the static case, this phenomenon is also known in oxide perovskite-based ferroelectrics[246]. Therefore, we estimate the effect of a photoexcited electron-hole pair, separated and localized to the opposite domain boundaries of a PND, as an additional constant electric field $\boldsymbol{E}_\mathrm{e}$ in the local lattice potential:

$$U^*(\boldsymbol{P}, \boldsymbol{E}_e) = -\frac{\alpha}{2}\boldsymbol{P}^2 + \frac{\gamma}{4}\boldsymbol{P}^4 - \boldsymbol{E}_e \cdot \boldsymbol{P}\ . \tag{6.4.2}$$

The magnitude of the field E_e is given by the charge separation and therefore by the size of the polar nanodomain. The stronger the localization (higher stabilization energy E_b), the higher the additional charge separation field E_e. The orientation of

$\boldsymbol{E_e}$ is determined by the orientation of the polar nanodomain and thus $U^*(P, E_e) = U^*(-P, -E_e)$, which means that the potential shift due $-E_e P$ in oppositely oriented PNDs does not cancel out. This is an important requirement for the coherent phonon amplitudes to constructively add up to a macroscopic signal throughout the whole probing volume.

Finally, we emphasize that the theory of local lattice vibrations is a challenging field, especially for DFT approaches. Therefore, the theory of electron-phonon interaction in anharmonic and dynamically disordered materials would greatly benefit from attention by the theory community.

6.4.2 Displacive excitation of coherent phonons in model potential

First, we convert the free energy as function of the polarization P to a lattice potential along the corresponding polar normal coordinate Q via the Born effective charge $P = ZQ$:

$$U^*(Q, E_\mathrm{e}) = -\frac{\alpha}{2} Z^2 Q^2 + \frac{\gamma}{4} Z^4 Q^4 - E_\mathrm{e} Z Q \ . \tag{6.4.3}$$

Notably, for an oppositely orientation PND, the charge separation field E_e and the Born-effective charge Z change their sign simultaneously. Thus $U^*(Q, E_\mathrm{e}) = U^*(Q, -E_\mathrm{e})$ is implicitly fulfilled.

To simulate the coherent lattice dynamics following an instantaneous change of the lattice potential $U(Q, 0)$ to $U^*(Q, E_\mathrm{e})$ in presence of a localized electron-hole pair, we model the local field by a Heaviside step function $E_e(t) = E_e H(t)$, as the rising time of E_e during the excitation with a 35 fs laser pulse is much faster than a

phonon half-period $2/\nu_{\mathrm{ph}}$. Therefore, the equation of motion, derived from Eq. (3) by the Euler-Lagrange equation,

$$m\ddot{Q} + \beta\dot{Q} - aQ + bQ^3 = E_{\mathrm{e}}H(t)\,Z, \tag{6.4.4}$$

is identical to the equation of motion for the impulsive excitation of a coherent phonon in the displacive limit (short: displacive excitation)[22,23]. This agrees with our understanding that the potential along the coordinate Q is instantaneously changed and thus the shifted potential minimum leads to the generation of a coherent phonon. Consequently, the equation of motion can be solved for $t \geq 0$ by setting $E_{\mathrm{e}}(t) = \mathrm{const.}$ with the starting conditions $Q_0 = Q_{\mathrm{min}}^{(0)}$ and $\dot{Q}_0 = 0$. Here, $Q_{\mathrm{min}}^{(0)}$ is the first minimum of the unexcited potential $U(Q, 0)$ (see cross markers in **Figure 6.10A**). Please note, that finite coherence time of the phonon was introduced by a phenomenological damping term $\beta\dot{Q}$.

We solved the equations of motion (Eq. (4)) under the aforementioned starting conditions for the excited state potentials $U^*(Q, E_{\mathrm{e}})$ shown in **Figure 6.3A** and **Figure 6.10A**. These correspond to linear increasing field parameters E_e in arbitrary units. We solve this ordinary differential equation (ODE) by a numerical 4th order Runge-Kutta method. The resulting coherent phonon amplitudes $Q(t)$ are shown in **Figure 6.3D** and **Figure 6.10B**, respectively, and vertically offset for clarity. This simple model reproduces the two main features of the experimentally observed coherent phonons (see **Figure 6.1C**: First, the coherent phonon frequency increases significantly with a stronger localization (higher E_{e}), see **Figure 6.10C**. Second, for a strong localization, the coherent phonon signal shows a significant

displacive feature, identified as an offset of the mean $Q(t > 0)$, see **Figure 6.10B** and **Figure 6.6D**.

The magnitude of the frequency shift depends on the anharmonicity of the potential as determined by the ratio between the harmonic and quartic potential coefficient in (5.4.3). For the simulations shown in **Figure 6.3** and detailed in **Figure 6.10**, we used a ratio of $a/b = 3$ for the harmonic vs. quartic contribution. In this case of a high anharmonicity the frequency doubling of ν_{ph} already occurs with a field increasing of E_e by one order of magnitude, which corresponds to a lowering of the potential minimum energy by a factor of 10 (see **Figure 6.10D**). Considering an electron and hole with Gaussian charge distributions (see **Figure 6.3B**), decreasing the spatial separation can easily lead to increases of E_e by several orders of magnitude. Therefore, even lower anharmonicities may be sufficient.

Finally, the so far unitless potential energy is calibrated to the experimental data by using the unperturbed double well barrier U_d (black curve in **Figure 6.3A** and **Figure 6.10A**) as a scaling parameter. For identical model parameters, we find a global agreement of our model with different experimental data sets (different samples, slightly different pump spectra) for an unperturbed barrier height of $U_d = 15\ \mathrm{meV}$ (see **Figure 6.3C**, **Figure 6.11B**, and **Figure 6.11C**). This is in full agreement with our previous assumption of $U_d \leq 25\ \mathrm{meV}$.

6.4.3 Extended data figures

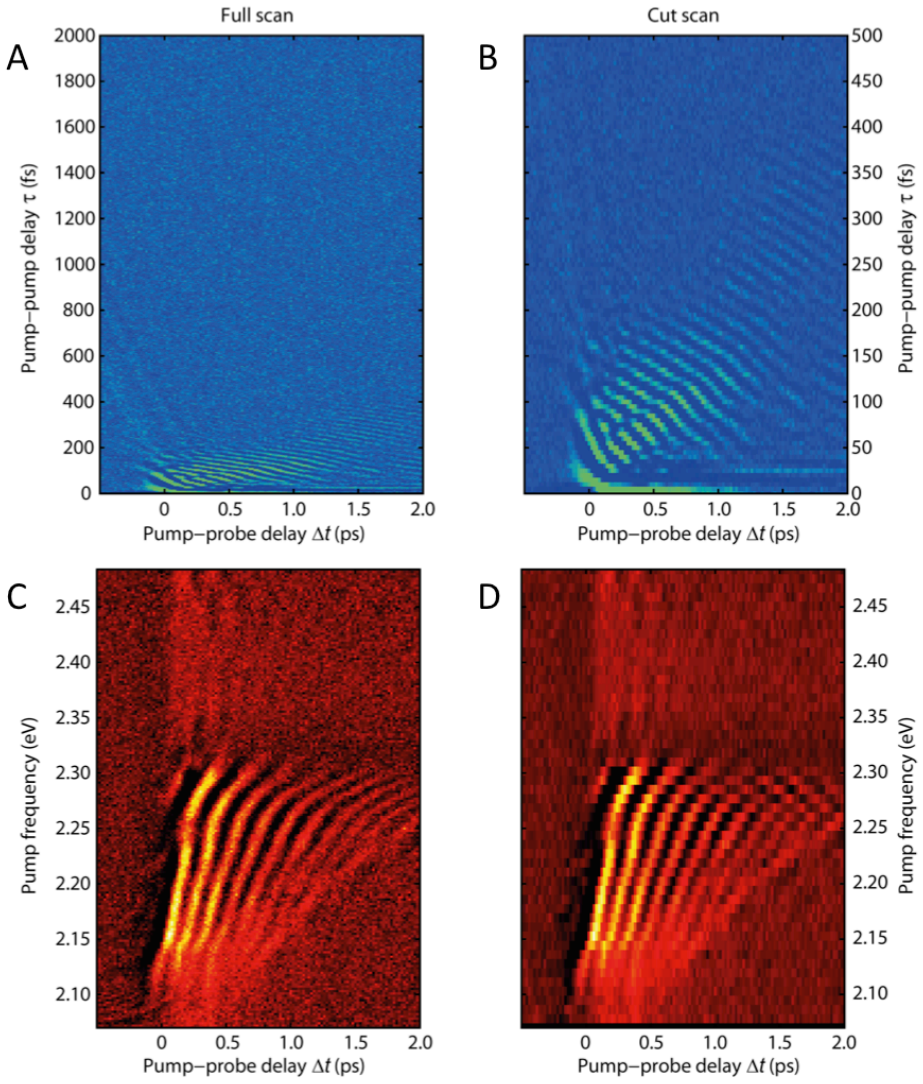

Figure 6.5 Time-time domain raw data and Fourier transform. A, Raw data of the FT-CPS shown in the main paper. Here the pump-pump steps size was 5 fs. **B**, Zoom-in of the first 500 fs where the main coherent features are found. The electronic coherence time clearly approaches 500 fs. **C**,**D**, Fourier transform with respect to the pump-pump delay for **A** and **B**, respectively. **D**, The Fourier transform of the first 500 fs of the pump-pump delay already contains the main FT-CPS features of **C**.

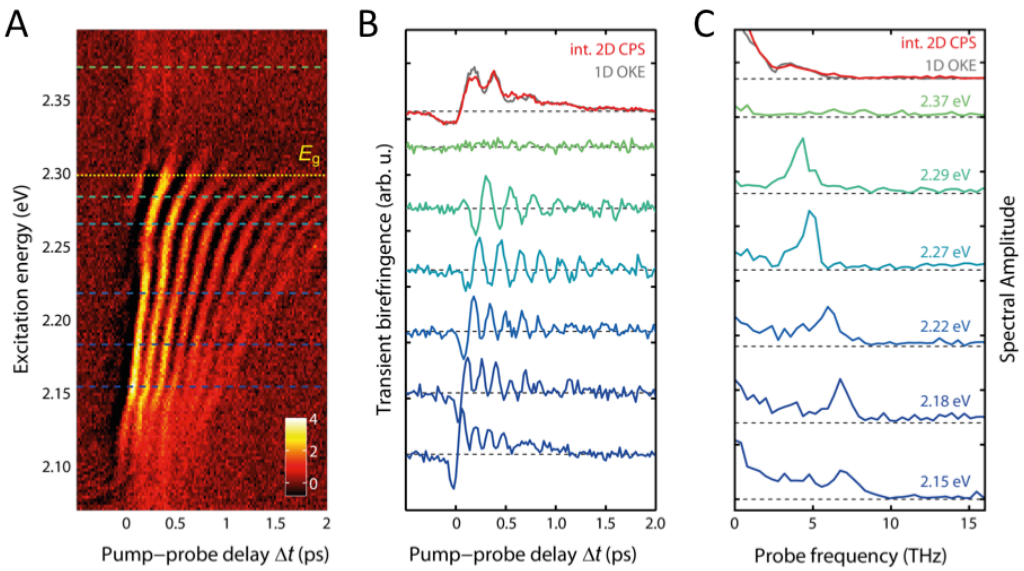

Figure 6.6 Extended line cuts for specific excitation energies. A, B, Time-frequency domain FT-CPS and the corresponding line cuts for fixed excitation energies as in **Figure 5.1A, B**, respectively. The time domain traces in B are vertically offset for clarity. The excitation energy-integrated FT-CPS (red line) agrees well with the single pulse excitation (grey line). **C**, Corresponding Fourier transforms of the line cuts in **B**. Already in these few line cuts a significant frequency shift is prominent for excitation energies ranging from 2.15 eV to 2.29 eV. The dominant high-frequency feature likely sits on top of smaller, less resolved low-frequency components, which is consistent with previously published OKE. The increased broad low frequency background for low E_{ex} originates from the displacive offset.

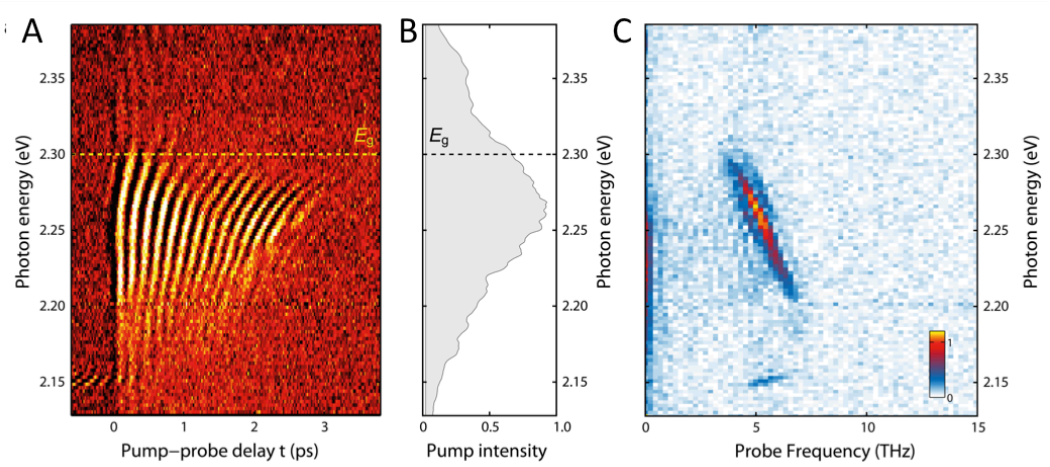

Figure 6.7 FT-CPS in a $CsPbBr_3$ samples with longer phonon coherence time. We investigated in total 3 different $CsPbBr_3$ samples, which vary in crystal quality and thickness. **A**, This sample shows the same characteristic features as **Figure 5.1A** despite the longer phonon coherence time and less pronounced oscillations at lower excitation energy (< 2.2 eV). **B** Pump photon energy spectrum. The high energy cutoff of the FT-CPS signal at 2.30 eV in **A**, is due to a drastic decrease in penetration depth and therefore decreased effective probing volume. As there are still significant photon energy components below 2.2 eV, the decline of the signal in this region is likely related to a vanishing density of highly localized electron-hole states C, The absolute frequency distribution and frequency shift is consistent with **Figure 6.2** and with the global fit of our model (see **Figure 6.9** and **Figure 6.11**).

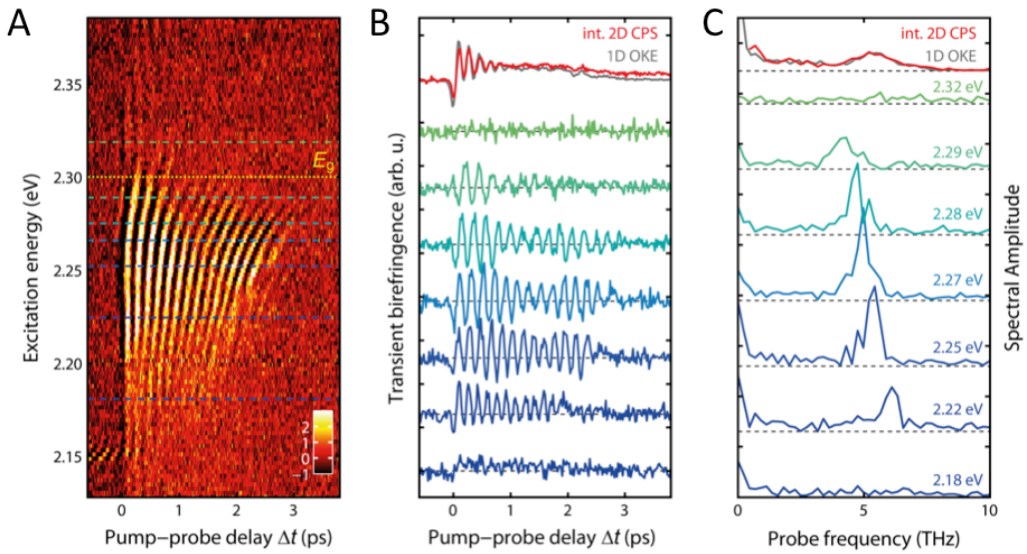

Figure 6.8 Line cuts for FT-CPS signal in Figure 6.7. **A** FT-CPS signal as shown in **Figure 6.7A**. **B** Line cuts for fixed excitation energy corresponding to the dashed lines in a. Here the longer phonon coherence time unveils low frequency beating. Interestingly, the low frequency beating nodes exhibit an opposite dependence on the excitation energy E_{ex}: For higher E_{ex} the beat frequency becomes higher. This beating might be related to coupled other modes. Also, here the integrated FT-CPS signal perfectly matches the single pulse excitation signal (1D OKE) and moreover explains the complicated nature and fast dephasing of the 1D signal. **C** Fourier transform of corresponding line cuts in **B**. Despite the more structured main frequency peak, the frequency shift agrees with **Figure 6.6**.

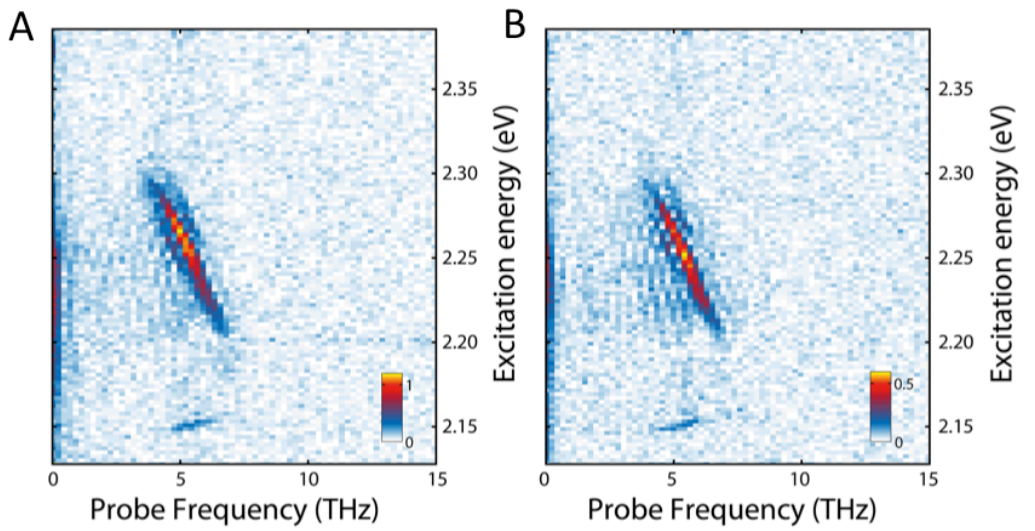

Figure 6.9 Comparison linear polarization change and change in ellipticity. A, 2D FFT of FT-CPS signal detected by a balanced detection with half-wave plate (HWP) corresponding to a transient change in linear probe polarization (same as **Figure 6.7C**). **B**, Same experimental conditions as in **A**, but detecting the transient change in probe ellipticity with a quarter-wave plate (QWP). As known from most coherent phonon studies, the phonon amplitude modulates both ellipticity and linear polarization in similar way. Only the magnitude of the QWP and HWP signal is different.

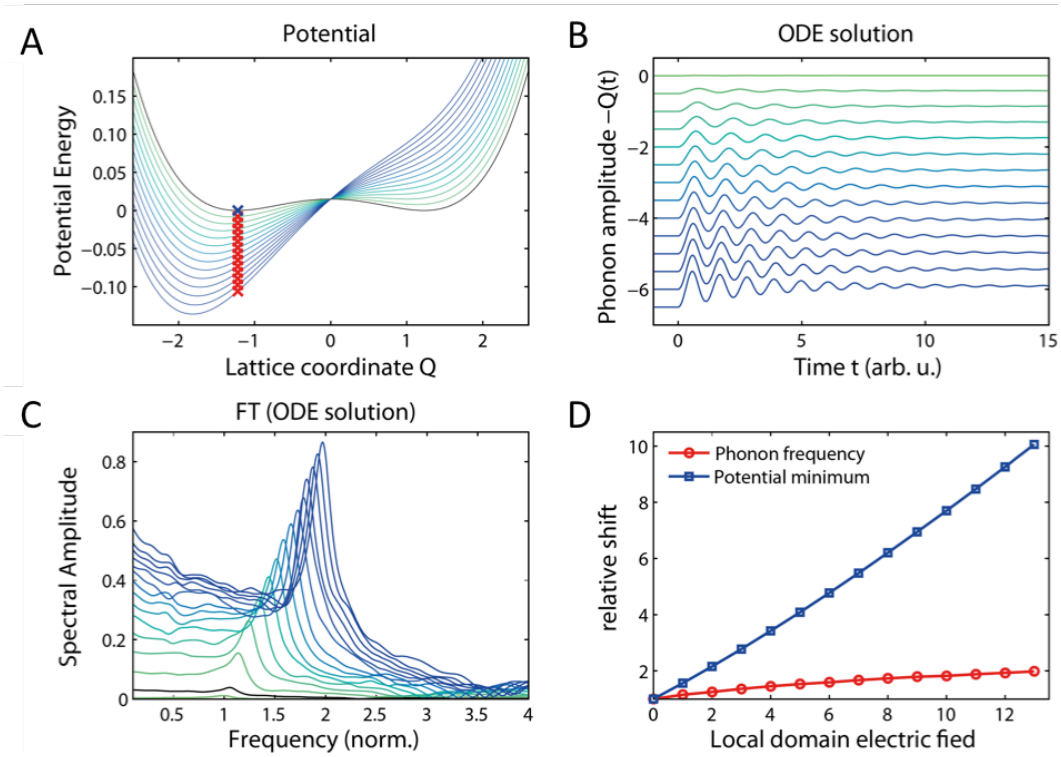

Figure 6.10 Model details for simulations in Figure 6.3. A, Lattice potentials $U(Q,0)$ (black line) and excited state potentials $U^*(Q,E_e)$ (colored lines) for linearly increasing local charge separation field E_e. To simulate a displacive excitation, the lattice coordinate Q of the unperturbed potential minimum (blue cross) is used as starting point $Q_0 = Q(t=0)$ (red crosses) for solving the equation of motion. **B**, Solutions of the equation of motion of the potentials in **A**. The phonon amplitudes $Q(t)$ are vertically offset for clearer visibility. A selection of the traces in **A**, and **B**, are shown in **Figure 6.3A** and **B**, respectively. **C**, A Fourier transform of the data in **B**, unveils the increasing frequency shift (normalized to the initial frequency of the unperturbed potential) with increasing E_e resulting from the high anharmonicity of the unperturbed potential. **D**, Phonon center frequency shift and potential minimum shift as a function of E_e. An increase of the local field E_e by one order of magnitude leads to a doubling of the phonon frequency. Plotting the potential minimum shift against the phonon frequency gives the theory curve for **Figure 6.3C** (by fitting the barrier height of the unperturbed potential as a scaling factor to U_d = 15 meV).

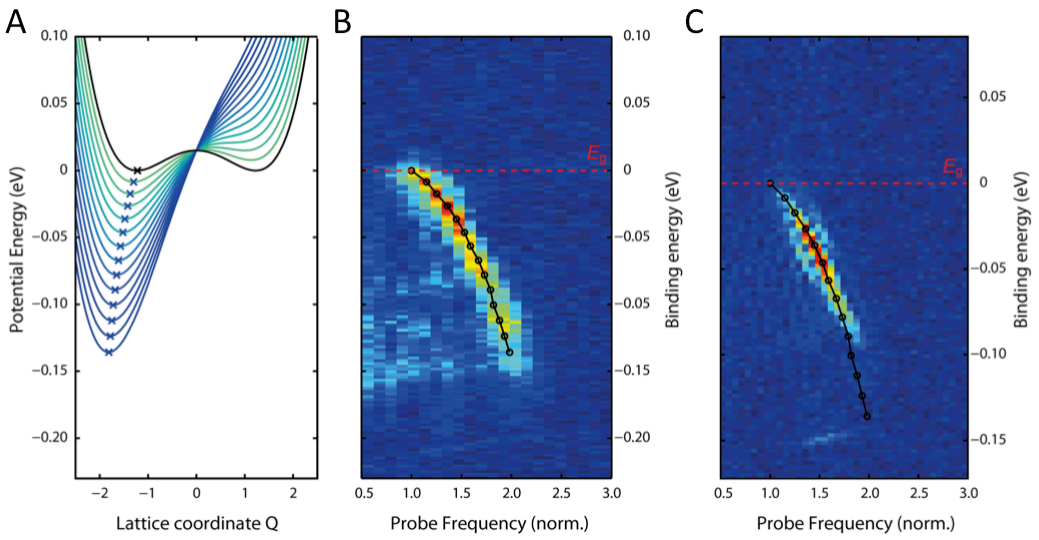

Figure 6.11 Global model fit. The anharmonicity of the potential $U(Q,0)$ with a linear increasing local field E_e in $U^*(Q,E_e)$ (both in arbitrary units) is globally fit to four experimental data sets of the phonon frequency shift as a function of the binding energy. The unperturbed double well barrier height U_d is used as a free scaling parameter. A good match to all experimental data sets is found for U_d = 15 meV. **A**, Modeled potential energy in meV after global fit and scaling to experimental data. **B**, **C**, The same model parameters agree well with the data sets shown in the main paper (**Figure 6.2**) and extended data (**Figure 6.7C**), respectively. The black line in **B** and **C** is the identical model curve.

7 Concluding Remarks

In summary, we present evidence of large polaron formation in MAPbBr3 and CsPbBr3 and highly anharmonic phonon behavior in the presence of charge carriers in a model system, $CsPbBr_3$. Using TR-OKE, we find agreement between the electronic and phonon responses of LHPs with above band-gap excitation, pointing to the formation of large polarons. In $CsPbBr_3$, using below band-gap excitation, we observe a transient localized vibrational state induced by a photoexcited electron-hole pair. The resulting lattice coherence is imposed across a broad frequency range of anharmonically-coupled phonons. These nonequilibrium phonon couplings manifest as a Γ-to-Γ point parametric down-conversion and a coherent softening of the phonon manifold. We develop FT-CPS to probe this anharmonic phonon response with respect to excitation photon energy. We find a dramatic softening from ~7.0 to ~3.5 THz as the carrier localization energy decreases from 150 meV to 0 meV. This softening is consistent with a ferroelectric double-well potential adjusted by an applied electric field, which is supplied by the photogenerated electron-hole pair. These anharmonic behaviors motivate a ferroelectric large polaron model, where charges are localized at the boundaries of fluctuating polar nanodomains[34]. In total, these experiments underscore the need for a charge-carrier screening model that incorporates phonon disorder and ferroelectric-like dielectric screening.

These observations and the ferroelectric large polaron hypothesis prompt a number of future experiments using coherent phonon spectroscopy. I have separated them into three broad categories:

(1) *Ferroelectric materials*. Because of the proposed ferroelectric screening character of LHPs, an obvious next step is to investigate the carrier-induced response of a macroscopically ferroelectric lattice. These materials bear significant similarities to LHPs, including large increases in the frequency-dependent dielectric function, ε, across the optical phonon resonances[34,111] and soft, anharmonically coupled phonon modes[250]. Notably, charge carriers localize at static, rather than dynamic, ferroelectric domain boundaries.[246,247]

(2) *Emphanitic materials*. The striking similarity of "emphanisis" or correlated dipoles in the lead chalcogenides and the polar nanodomains of LHPs suggests similar lattice anharmonicity and ferroelectric-like dielectric screening[46,47,60,87–89]. The ferroelectric polaron hypothesis can be further developed by investigations of known emphanitic materials such as PbS, PbSe, and $CsSnBr_3$[85]. Of these, $CsSnBr_3$ presents the most opportune comparison, since it is also a perovskite structure. The reported coherent displacement of Sn^{2+} is larger than that of Pb^{2+}, resulting in a static dieletric constant ε_s that exceeds that of $CsPbBr_3$[85].

(3) *Low temperature measurements.* All experiments in this thesis were conducted at room temperature. Because of the strong temperature dependence of polar fluctuations and solvation-like behavior[176,220], the spectroscopic signatures of the ferroelectric polaron – large phonon softening and anharmonically coupled phonons – should be inhibited at 77 K.

References

1. (eds.) Masson-Delmotte, V. *et al.* IPCC, 2018: Summary for Policymakers. *Glob. Warm. 1.5°C. An IPCC Spec. Rep. impacts Glob. Warm. 1.5°C above pre-industrial levels Relat. Glob. Greenh. gas Emiss. pathways, Context Strength. Glob. response to Threat Clim. Chang.*
2. Swanson, R. M. A Vision for Crystalline Silicon Photovoltaics. *Prog. Photovolt Res. Appl.* **14**, 443–453 (2006).
3. Snaith, H. J. Perovskites: The emergence of a new era for low-cost, high-efficiency solar cells. *J. Phys. Chem. Lett.* **4**, 3623–3630 (2013).
4. Kojima, A., Teshima, K., Shirai, Y. & Miyasaka, T. Organometal Halide Perovskites as Visible- Light Sensitizers for Photovoltaic Cells. *J. Am. Chem. Soc.* **131**, 6050–6051 (2009).
5. NREL. Best Research-Cell Efficiencies. (2019).
6. Fu, R., James, T. L. & Woodhouse, M. Economic measurements of polysilicon for the photovoltaic industry: Market competition and manufacturing competitiveness. *IEEE J. Photovoltaics* **5**, 515–524 (2015).
7. Haynes, J. R. & Hornbeck, J. A. Trapping of Minority Carriers in Silicon. II. n-Type Silicon. *Phys. Rev.* **100**, 606–615 (1955).
8. Hornbeck, J. A. & Haynes, J. R. Trapping of Minority Carriers in Silicon. I. P-Type Silicon. *Phys. Rev.* **97**, 311–321 (1955).
9. Duan, H. S. *et al.* The identification and characterization of defect states in hybrid organic-inorganic perovskite photovoltaics. *Phys. Chem. Chem. Phys.* **17**, 112 (2015).
10. Samiee, M. *et al.* Defect density and dielectric constant in perovskite solar cells. *Appl. Phys. Lett.* **105**, (2014).
11. Brenner, T. M., Egger, D. a., Kronik, L., Hodes, G. & Cahen, D. Hybrid organic—inorganic perovskites: low-cost semiconductors with intriguing charge-transport properties. *Nat. Rev. Mater.* **1**, 15007 (2016).
12. Bi, Y. *et al.* Charge Carrier Lifetimes Exceeding 15 μs in Methylammonium Lead Iodide Single Crystals. *J. Phys. Chem. Lett.* **7**, 923–928 (2016).
13. Wehrenfennig, C., Eperon, G. E., Johnston, M. B., Snaith, H. J. & Herz, L. M.

High charge carrier mobilities and lifetimes in organolead trihalide perovskites. *Adv. Mater.* **26**, 1584–1589 (2014).

14. Shi, D. *et al.* Low trap-state density and long carrier diffusion in organolead trihalide perovskite single crystals. *Sci.* **347**, 519–522 (2015).
15. Dong, Q. *et al.* Electron-hole diffusion lengths > 175 μm in solution-grown CH3NH3PbI3 single crystals. *Science (80-.).* **347**, 967–970 (2015).
16. Stranks, S. D. *et al.* Electron-hole diffusion lengths exceeding 1 micrometer in an organometal trihalide perovskite absorber. *Science (80-.).* **342**, 341–344 (2013).
17. Xing, G. *et al.* Long-Range Balanced Electron- and Hole-Transport Lengths in Organic-Inorganic CH3NH3PbI3. *Science (80-.).* **342**, 344–347 (2013).
18. Bretschneider, S. A., Laquai, F. & Bonn, M. Trap-Free Hot Carrier Relaxation in Lead-Halide Perovskite Films. *J. Phys. Chem. C* **121**, 11201–11206 (2017).
19. Deschler, F. *et al.* High photoluminescence efficiency and optically pumped lasing in solution-processed mixed halide perovskite semiconductors. *J. Phys. Chem. Lett.* **5**, 1421–1426 (2014).
20. Zhu, H. *et al.* Screening in crystalline liquids protects energetic carriers in hybrid perovskites. *Science (80-.).* **353**, 1409–1413 (2016).
21. Niesner, D. *et al.* Persistent Energetic Electrons in Methylammonium Lead Iodide Perovskite Thin Films. *J. Am. Chem. Soc.* **138**, 15717–15726 (2016).
22. Guo, Z. *et al.* Long-range hot-carrier transport in hybrid perovskites visualized by ultrafast microscopy. *Science (80-.).* **356**, 59–62 (2017).
23. Yang, Y. *et al.* Observation of a hot-phonon bottleneck in lead-iodide perovskites. *Nat. Photonics* **10**, 53–59 (2016).
24. Li, M. *et al.* Slow cooling and highly efficient extraction of hot carriers in colloidal perovskite nanocrystals. *Nat. Commun.* **8**, 3–12 (2017).
25. Chen, Y. *et al.* Extended carrier lifetimes and diffusion in hybrid perovskites revealed by Hall effect and photoconductivity measurements. *Nat. Commun.* **7**, 1–9 (2016).
26. Yi, H. T., Wu, X., Zhu, X. & Podzorov, V. Intrinsic Charge Transport across Phase Transitions in Hybrid Organo-Inorganic Perovskites. *Adv. Mater.* **28**, 6509–6514 (2016).

27. Milot, R. L., Eperon, G. E., Snaith, H. J., Johnston, M. B. & Herz, L. M. Temperature-Dependent Charge-Carrier Dynamics in CH3NH3PbI3 Perovskite Thin Films. *Adv. Funct. Mater.* **25**, 6218–6227 (2015).
28. Zhu, X.-Y. & Podzorov, V. Charge Carriers in Hybrid Organic − Inorganic Lead Halide Perovskites Might Be Protected as Large Polarons. *J. Phys. Chem. Lett.* **6**, 4758–4761 (2015).
29. Fröhlich, H. Electrons in lattice fields. *Adv. Phys.* **3**, 325–361 (1954).
30. Feynman, R. P. Slow electrons in a polar crystal. *Phys. Rev.* **97**, 660 (1955).
31. Emin, D. *Polarons*. (Cambridge University Press, 2013).
32. Emin, D. & Holstein, T. Adiabatic theory of an electron in a deformable continuum. *Phys. Rev. Lett.* **36**, 323–326 (1976).
33. Emin, D. Barrier to recombination of oppositely charged large polarons Barrier to recombination of oppositely charged large polarons. *J. Appl. Phys.* **123**, (2018).
34. Miyata, K. & Zhu, X.-Y. Ferroelectric large polarons. *Nat. Mater.* **17**, 379–381 (2018).
35. Lan, Y. *et al.* Ultrafast correlated charge and lattice motion in a hybrid metal halide perovskite. *Sci. Adv.* **5**, (2019).
36. Stoumpos, C. C. *et al.* Crystal Growth of the Perovskite Semiconductor CsPbBr 3 : A New Material for High-Energy Radiation Detection. *Cryst. Growth Des.* **13**, 2722–2727 (2013).
37. Brivio, F. *et al.* Lattice dynamics and vibrational spectra of the orthorhombic , tetragonal , and cubic phases of methylammonium lead iodide. *Phys. Rev. B* **92**, 1–8 (2015).
38. Stoumpos, C. C., Malliakas, C. D. & Kanatzidis, M. G. Semiconducting tin and lead iodide perovskites with organic cations: Phase transitions, high mobilities, and near-infrared photoluminescent properties. *Inorg. Chem.* **52**, 9019–9038 (2013).
39. Umebayashi, T. & Asai, K. Electronic structures of lead iodide based low-dimensional crystals. *Phys. Rev. B* **67**, 1–6 (2003).
40. Meloni, S., Palermo, G., Ashari-Astani, N., Grätzel, M. & Rothlisberger, U. Valence and conduction band tuning in halide perovskites for solar cell

applications. *J. Mater. Chem. A* **4**, 15997–16002 (2016).

41. Umari, P., Mosconi, E. & De Angelis, F. Relativistic GW calculations on CH3NH3PbI3 and CH3NH3SnI3 perovskites for solar cell applications. *Sci. Rep.* **4**, 4467 (2014).
42. Milot, R. L., Eperon, G. E., Snaith, H. J., Johnston, M. B. & Herz, L. M. Temperature-Dependent Charge-Carrier Dynamics in CH3NH3PbI3 Perovskite Thin Films. *Adv. Funct. Mater.* **25**, 6218–6227 (2015).
43. D'Innocenzo, V. *et al.* Excitons versus free charges in organo-lead tri-halide perovskites. *Nat Commun* **5**, (2014).
44. Y.P., V. Temperature dependence of the energy gap in semiconductors. *Physica* **34**, 149–154 (1967).
45. Ashcroft, N. W. & Mermin, N. D. *Solid State Physics*. (Harcourt, 1976).
46. Yu, R. *et al.* Emphanitic anharmonicity in PbSe at high temperature and anomalous electronic properties in the PbQ(Q= S, Se, Te) system. *Phys. Rev. B* **98**, 1–6 (2018).
47. Knox, K. R., Bozin, E. S., Malliakas, C. D., Kanatzidis, M. G. & Billinge, S. J. L. Local off-centering symmetry breaking in the high-temperature regime of SnTe. *Phys. Rev. B - Condens. Matter Mater. Phys.* **89**, 1–5 (2014).
48. Wang, L. *et al.* Tunable bandgap in hybrid perovskite CH3NH3Pb (Br3 − yXy) single crystals and photodetector applications. *AIP Adv.* **6**, (2016).
49. Miyata, K. *et al.* Large polarons in lead halide perovskites. *Sci. Adv.* **3**, e1701217 (2017).
50. Umari, P., Mosconi, E. & De Angelis, F. Infrared Dielectric Screening Determines the Low Exciton Binding Energy of Metal-Halide Perovskites. *J. Phys. Chem. Lett.* **9**, 620–627 (2018).
51. Comin, R. *et al.* Structural, optical, and electronic studies of wide-bandgap lead halide perovskites. *J. Mater. Chem. C* **3**, 8839–8843 (2015).
52. Herz, L. M. How Lattice Dynamics Moderate the Electronic Properties of Metal-Halide Perovskites. *J. Phys. Chem. Lett.* **9**, 6853–6863 (2018).
53. Tilchin, J. *et al.* Hydrogen-like Wannier-Mott Excitons in Single Crystal of Methylammonium Lead Bromide Perovskite. *ACS Nano* **10**, 6363–6371 (2016).

54. Ziffer, M. E., Mohammed, J. C. & Ginger, D. S. Electroabsorption Spectroscopy Measurements of the Exciton Binding Energy, Electron-Hole Reduced Effective Mass, and Band Gap in the Perovskite CH3NH3PbI3. *ACS Photonics* **3**, 1060–1068 (2016).

55. Cha, J. H. *et al.* Photoresponse of CsPbBr3 and Cs4PbBr6 Perovskite Single Crystals. *J. Phys. Chem. Lett.* **8**, 565–570 (2017).

56. Leguy, A. M. A. *et al.* The dynamics of methylammonium ions in hybrid organic–inorganic perovskite solar cells. *Nat. Commun.* **6**, 1–10 (2015).

57. Poglitsch, A. & Weber, D. Dynamic disorder in methylammoniumtrihalogenoplumbates (II) observed by millimeter-wave spectroscopy. *J. Chem. Phys.* **87**, 6373–6378 (1987).

58. Mitzi, D. B. Templating and structural engineering in organic-inorganic perovskites. *J. Chem. Soc. Dalt. Trans.* 1–12 (2001). doi:10.1039/b007070j

59. Lee, J. H., Bristowe, N. C., Bristowe, P. D. & Cheetham, A. K. Role of hydrogen-bonding and its interplay with octahedral tilting in CH3NH3PbI3. *Chem. Commun.* **51**, 6434 (2015).

60. Beecher, A. N. *et al.* Direct Observation of Dynamic Symmetry Breaking above Room Temperature in Methylammonium Lead Iodide Perovskite. *ACS Energy Lett.* **1**, 880–887 (2016).

61. Motta, C. *et al.* Revealing the role of organic cations in hybrid halide perovskite CH<inf>3</inf> NH<inf>3</inf>PbI<inf>3</inf>. *Nat. Commun.* **6**, 1–7 (2015).

62. Baikie, T. *et al.* A combined single crystal neutron/X-ray diffraction and solid-state nuclear magnetic resonance study of the hybrid perovskites CH3NH3PbX3 (X = I, Br and Cl). *J. Mater. Chem. A* **3**, 9298–9307 (2015).

63. Bakulin, A. A. *et al.* Real-Time Observation of Organic Cation Reorientation in Methylammonium Lead Iodide Perovskites. *J. Phys. Chem. Lett.* **6**, 3663–3669 (2015).

64. Mattoni, A., Filippetti, A., Saba, M. I. & Delugas, P. Methylammonium Rotational Dynamics in Lead Halide Perovskite by Classical Molecular Dynamics: The Role of Temperature. *J. Phys. Chem. C* **119**, 17421–17428 (2015).

65. Mosconi, E., Quarti, C., Ivanovska, T., Ruani, G. & De Angelis, F. Structural and electronic properties of organo-halide lead perovskites: A combined IR-spectroscopy and ab initio molecular dynamics investigation. *Phys. Chem. Chem. Phys.* **16**, 16137–16144 (2014).

66. Yaffe, O. *et al.* Local Polar Fluctuations in Lead Halide Perovskite Crystals. *Phys. Rev. Lett.* **118**, 1–6 (2017).

67. Miyata, K., Atallah, T. L. & Zhu, X. Y. Lead halide perovskites: Crystal-liquid duality, phonon glass electron crystals, and large polaron formation. *Sci. Adv.* **3**, 1–11 (2017).

68. Udagawa, M. *et al.* Guest ion motion in cage structure crystals investigated by Raman scattering. *J. Phys. Soc. Japan* **77**, 142–147 (2008).

69. Filippetti, A., Caddeo, C., Delugas, P. & Mattoni, A. Appealing Perspectives of Hybrid Lead-Iodide Perovskites as Thermoelectric Materials. *J. Phys. Chem. C* **120**, 28472–28479 (2016).

70. Takabatake, T., Suekuni, K., Nakayama, T. & Kaneshita, E. Phonon-glass electron-crystal thermoelectric clathrates: Experiments and theory. *Rev. Mod. Phys.* **86**, 669–716 (2014).

71. Leguy, A. M. A. *et al.* Dynamic disorder, phonon lifetimes, and the assignement of modes to the vibrational spectra of methylammonium lead halide perovskites. *Phys. Chem. Chem. Phys.* **18**, 27051–27066 (2016).

72. Elbaz, G. A. *et al.* Phonon Speed, Not Scattering, Differentiates Thermal Transport in Lead Halide Perovskites. *Nano Lett.* **17**, 5734–5739 (2017).

73. Pisoni, A. *et al.* Ultra-low thermal conductivity in organic–inorganic hybrid perovskite CH3NH3PbI3. *J. Phys. Chem. Lett.* **5**, 2488–2492 (2014).

74. Guo, Z., Yoon, S. J., Manser, J. S., Kamat, P. V & Luo, T. Structural phase- and degradation-dependent thermal conductivity of CH3NH3PbI3 perovskite thin films. *J. Phys. Chem. C* **120**, 6394–6401 (2016).

75. Kovalsky, A., Wang, L., Marek, G. T., Burda, C. & Dyck, J. S. Thermal Conductivity of CH3NH3PbI3 and CsPbI3: Measuring the Effect of the Methylammonium Ion on Phonon Scattering. *J. Phys. Chem. C* **121**, 3228–3233 (2017).

76. Whalley, L. D., Skelton, J. M., Frost, J. M. & Walsh, A. Phonon

anharmonicity, lifetimes, and thermal transport in CH3NH3PbI3 from many-body perturbation theory. *Phys. Rev. B* **94**, 1–5 (2016).

77. Joshi, P. P., Maehrlein, S. F. & Zhu, X. Dynamic Screening and Slow Cooling of Hot Carriers in Lead Halide Perovskites. *Adv. Mater.* 1–10 (2019). doi:10.1002/adma.201803054
78. Quarti, C. *et al.* Structural and optical properties of methylammonium lead iodide across the tetragonal to cubic phase transition: implications for perovskite solar cells. *Energy Environ. Sci.* **9**, 155–163 (2016).
79. Marronnier, A. *et al.* Structural Instabilities Related to Highly Anharmonic Phonons in Halide Perovskites. *J. Phys. Chem. Lett.* **8**, 2659–2665 (2017).
80. Beecher, A. N. *et al.* Direct Observation of Dynamic Symmetry Breaking above Room Temperature in Methylammonium Lead Iodide Perovskite. *ACS Energy Lett.* **1**, 880–887 (2016).
81. Worhatch, R. J., Kim, H. J., Swainson, I. P., Yonkeu, A. L. & Billinge, S. J. L. Study of local structure in selected organic-inorganic perovskites in the Pm3̄m phase. *Chem. Mater.* (2008). doi:10.1021/cm702668d
82. Flocken, J. W., Guenther, R. A., Hardy, J. R. & Boyer, L. L. First-principles study of structural instabilities in halide-based perovskites: Competition between ferroelectricity and ferroelasticity. *Phys. Rev. B* **31**, 7252–7260 (1985).
83. Patrick, C. E., Jacobsen, K. W. & Thygesen, K. S. Anharmonic stabilization and band gap renormalization in the perovskite CsSnI 3. *RAPID Commun. Phys. Rev. B* **92**, 1–5 (2015).
84. Stokes, H. T., Kisi, E. H., Hatch, D. M. & Howard, C. J. Structural Science Group-theoretical analysis of octahedral tilting in ferroelectric perovskites. *Acta Crystallogr. Sect. B Struct. Sci.* **B58**, 934–938 (2002).
85. Fabini, D. H. *et al.* Dynamic Stereochemical Activity of the Sn 2+ Lone Pair in Perovskite. *J. Am. Chem. Soc.* **138**, 11820–11832 (2016).
86. Weller, M. T., Weber, O. J., Henry, P. F., Di Pumpo, A. M. & Hansen, T. C. Complete structure and cation orientation in the perovskite photovoltaic methylammonium lead iodide between 100 and 352 K. *Chem. Commun.* **51**, 4180 (2015).
87. Božin, E. S. *et al.* Entropically stabilized local dipole formation in lead

chalcogenides. *Science (80-.).* **330**, 1660–1663 (2010).

88. Jensen, K. M. Ø. *et al.* Lattice dynamics reveals a local symmetry breaking in the emergent dipole phase of PbTe. *Phys. Rev. B - Condens. Matter Mater. Phys.* **86**, 1–7 (2012).
89. Sangiorgio, B. *et al.* PHYSICAL REVIEW MATERIALS 2 , 085402 (2018) Correlated local dipoles in PbTe. **085402**, (2018).
90. Dey, P. *et al.* Origin of the temperature dependence of the band gap and PbSe quantum dots of PbS. *Solid State Commun.* **165**, 49–54 (2013).
91. Katan, C., Mohite, A. D. & Even, J. Entropy in halide perovskites. *Nat. Mater.* **17**, 377–379 (2018).
92. Rabe, K. M., Ahn, C. & Triscone, J.-M. *Physics of Ferroelectrics: A Modern Perspective*. **105**, (Springer, 2007).
93. Aschauer, U. & Spaldin, N. A. Competition and cooperation between antiferrodistortive and ferroelectric instabilities in the model perovskite SrTiO3. *J. Phys. Condens. Matter* **26**, (2014).
94. Dresselhaus, G. Spon-orbit coupling effects in zinc blend structures. *Phys. Rev.* **100**, 580–586 (1955).
95. Stranks, S. D. & Plochocka, P. Riddles in perovskite research: The influence of the Rashba effect. *Nat. Mater.* **17**, 377 (2018).
96. Isarov, M. *et al.* Rashba effect in a single colloidal CsPbBr3perovskite nanocrystal detected by magneto-optical measurements. *Nano Lett.* **17**, 5020–5026 (2017).
97. Niesner, D. *et al.* Giant Rashba Splitting in CH3NH3PbBr3 Organic-Inorganic Perovskite. *Phys Rev Lett* **117**, 126401 (2016).
98. Kepenekian, M. *et al.* Rashba and Dresselhaus Effects in Hybrid Organic–Inorganic Perovskites: From Basics to Devices. (2015).
99. Etienne, T., Mosconi, E. & De Angelis, F. Dynamical Origin of the Rashba Effect in Organohalide Lead Perovskites: A Key to Suppressed Carrier Recombination in Perovskite Solar Cells? *J. Phys. Chem. Lett.* **7**, 1638–1645 (2016).
100. Zheng, F., Tan, L. Z., Liu, S. & Rappe, A. M. Rashba spin-orbit coupling enhanced carrier lifetime in CH3NH3PbI3. *Nano Lett.* **15**, 7794–7800 (2015).

101. Kittel, C. *Introduction to Solid State Physics*. (John Wiley & Sons, Inc., 2005).
102. Wilson, J. N., Frost, J. M., Wallace, S. K. & Walsh, A. Dielectric and ferroic properties of metal halide perovskites. *APL Mater.* **7**, 1–14 (2019).
103. Sendner, M. *et al.* Optical Phonons in Methylammonium Lead Halide Perovskites and Implications for Charge Transport. *Mater. Horizons* **3**, 613–620 (2016).
104. Anusca, I. *et al.* Dielectric Response: Answer to Many Questions in the Methylammonium Lead Halide Solar Cell Absorbers. *Adv. Energy Mater.* **7**, 1–12 (2017).
105. Segelstein, D. J. The Complex Refractive Index of Water. (University of Missouri - Kansas City, 1975).
106. Palik, E. D. *Handbook of Optical Constants of Solids*. (Academic Press, 1998).
107. Moore, W. J. & Holm, R. T. Infrared dielectric constant of gallium arsenide. *J. Appl. Phys.* **80**, 6939–6942 (1996).
108. Levi, A. F. J. The Lorentz oscillator model. in *Essential Classical Mechanics for Device Physics* (ed. Publishers, M. & C.) (2016). doi:10.1088/978-1-6817-4413-1ch5
109. Du, M. H. & Singh, D. J. Enhanced Born charge and proximity to ferroelectricity in thallium halides. *Phys. Rev. B - Condens. Matter Mater. Phys.* **81**, 1–5 (2010).
110. Siemons, W. *et al.* Dielectric-constant-enhanced hall mobility in complex oxides. *Adv. Mater.* **24**, 3965–3969 (2012).
111. Kamba, S. *et al.* Ferroelastic phase in SrBi2Ta2O9 and study of the ferroelectric phase-transition dynamics. *Appl. Phys. Lett.* **81**, 1056–1058 (2002).
112. Zhu, X. & Podzorov, V. Charge Carriers in Hybrid Organic-Inorganic Lead Halide Perovskites Might be Protected as Large Polarons. *J. Phys. Chem. Lett.* **6**, 4758–4761 (2015).
113. Frost, J. M., Whalley, L. D. & Walsh, A. Slow Cooling of Hot Polarons in Halide Perovskite Solar Cells. *ACS Energy Lett.* **2**, 2647–2652 (2017).
114. Ma, J. & Wang, L. W. Nanoscale charge localization induced by random orientations of organic molecules in hybrid perovskite CH3NH3PbI3. *Nano Lett.* **15**, 248–253 (2015).

115. Quarti, C., Mosconi, E. & De Angelis, F. Structural and electronic properties of organo-halide hybrid perovskites from ab initio molecular dynamics. *Phys. Chem. Chem. Phys.* **17**, 9394–9409 (2015).

116. March, S. A. *et al.* Four-Wave Mixing in Perovskite Photovoltaic Materials Reveals Long Dephasing Times and Weaker Many-Body Interactions than GaAs. *ACS Photonics* **4**, 1515–1521 (2017).

117. Shi, D. *et al.* Low trap-state density and long carrier diffusion in organolead trihalide perovskite single crystals. *Science (80-.).* **347**, 519 (2015).

118. Dastidar, S., Li, S., Smolin, S. Y., Baxter, J. B. & Fafarman, A. T. Slow Electron-Hole Recombination in Lead Iodide Perovskites Does Not Require a Molecular Dipole. *ACS Energy Lett.* (2017). doi:10.1021/acsenergylett.7b00606

119. Brennan, K. F. *The Physics of Semiconductors*. (Cambridge University Press, 1999).

120. Tisdale, W. A., Muntwiler, M., Norris, D. J., Aydil, E. S. & Zhu, X. Electron Dynamics at the ZnO (1010) Surface. *J. Phys. Chem. C* **112**, 14682–14692 (2008).

121. Price, M. B. *et al.* Hot-carrier cooling and photoinduced refractive index changes in organic-inorganic lead halide perovskites. *Nat. Commun.* **6**, 1–8 (2015).

122. Frost, J. M., Whalley, L. D. & Walsh, A. Slow Cooling of Hot Polarons in Halide Perovskite Solar Cells. (2017). doi:10.1021/acsenergylett.7b00862

123. Li, M., Fu, J., Xu, Q. & Sum, T. C. Slow Hot-Carrier Cooling in Halide Perovskites: Prospects for Hot-Carrier Solar Cells. *Adv. Mater.* 1–17 (2018). doi:10.1002/adma.201802486

124. Herz, L. M. Charge-Carrier Mobilities in Metal Halide Perovskites: Fundamental Mechanisms and Limits. *ACS Energy Lett.* **2**, 1539–1548 (2017).

125. Ponseca, C. S. *et al.* Organometal Halide Perovskite Solar Cell Materials Rationalized: Ultrafast Charge Generation, High and Microsecond-Long Balanced Mobilities, and Slow Recombination. (2014).

126. Shrestha, S. *et al.* Assessing Temperature Dependence of Drift Mobility in Methylammonium Lead Iodide Perovskite Single Crystals. *J. Phys. Chem. C*

122, 5935–5939 (2018).

127. Sze, S. M. & Ng, K. K. *Physics Of Semiconductor Devices*. (Wiley-Interscience, 2007).
128. Zhang, M., Zhang, X., Huang, L. Y., Lin, H. Q. & Lu, G. Charge transport in hybrid halide perovskites. *Phys. Rev. B* **96**, 1–7 (2017).
129. Neukirch, A. J. *et al.* Polaron stabilization by cooperative lattice distortion and cation rotations in hybrid perovskite materials. *Nano Lett.* **16**, 3809–3816 (2016).
130. Wolf, C., Cho, H., Kim, Y. H. & Lee, T. W. Polaronic Charge Carrier–Lattice Interactions in Lead Halide Perovskites. *ChemSusChem* **10**, 3705–3711 (2017).
131. Bretschneider, S. A. *et al.* Quantifying Polaron Formation and Charge Carrier Cooling in Lead-Iodide Perovskites. *Adv. Mater.* **30**, 1–8 (2018).
132. Zhu, H. *et al.* Organic Cations Might Not Be Essential to the Remarkable Properties of Band Edge Carriers in Lead Halide Perovskites. *Adv. Mater.* **29**, 1603072 (2017).
133. Guo, Y. *et al.* Dynamic emission Stokes shift and liquid-like dielectric solvation of band edge carriers in lead-halide perovskites. *Nat. Commun.* **10**, 1–8 (2019).
134. Monahan, D. M., Guo, L., Lin, J., Dou, L. & Yang, P. Room-Temperature Coherent Optical Phonon in 2D Electronic Spectra of CH 3 NH 3 PbI 3 Perovskite as a Possible Cooling Bottleneck. *J. Phys. Chem. Lett.* **8**, 3211–3215 (2017).
135. Wu, X. *et al.* Light-induced picosecond rotational disordering of the inorganic sublattice in hybrid perovskites. *Sci. Adv.* **3**, 1–7 (2017).
136. Zheng, K. *et al.* Direct Experimental Evidence for Photoinduced Strong-Coupling Polarons in Organolead Halide Perovskite Nanoparticles. *J. Phys. Chem. Lett.* **7**, 4535–4539 (2016).
137. Zhou, Y. *et al.* Giant photostriction in organic-inorganic lead halide perovskites. *Nat. Commun.* **7**, 1–8 (2016).
138. Tsai, H. *et al.* Light-induced lattice expansion leads to high-efficiency perovskite solar cells. *Science (80-.).* **360**, 67–80 (2018).
139. Joshi, P. P., Maehrlein, S. F. & Zhu, X. Dynamic Screening and Slow Cooling

of Hot Carriers in Lead Halide Perovskites. *Adv. Mater.* **1803054**, 1–10 (2019).

140. Nasu, K. Photogeneration of superparaelectric large polarons in dielectrics with soft anharmonic (formula presented) phonons. *Phys. Rev. B - Condens. Matter Mater. Phys.* **67**, 1–8 (2003).

141. Yu, Q. & Nasu, K. Theory of super-para-electric large polaron for gigantic photo-enhancements of dielectric constant and electronic conductivity in SrTiO3. *J. Phys. Conf. Ser.* **21**, 1–6 (2005).

142. Munson, K. T., Eric, R., Doucette, G. S. & Asbury, J. B. Dynamic Disorder Dominates Delocalization , Transport , and Recombination in Halide Perovskites. *Chem* **4**, 1–18 (2018).

143. Li, X. *et al.* Terahertz field–induced ferroelectricity in quantum paraelectric SrTiO 3. *Science (80-.).* **364**, 1079–1082 (2019).

144. Strickland, D. & Mourou, G. Compression Of Amplified Chirped Optical Pulses. *Opt. Commun.* **56**, 219–221 (1985).

145. Backus, S., Durfee III, C. G., Murnane, M. M. & Kapteyn, H. C. High power ultrafast lasers. *Rev. Sci. Instrum.* **69**, 1207–1223 (1998).

146. Svelto, O. *Principles of Lasers.* (Springer, 1976).

147. Boyd, R. W. *Nonlinear Optics.* (Elsevier Inc., 2008).

148. Wilhelm, T., Piel, J. & Riedle, E. Sub-20-fs pulses tunable across the visible from a blue-pumped single-pass noncollinear parametric converter. *Opt. Lett.* **22**, 1494–1496 (1997).

149. McMorrow, D. & Lotshaw, W. T. Intermolecular Dynamics in Acetonitrile Probed with Femtosecond Fourier Transform Raman Spectroscopy. *J. Phys. Chem.* **95**, 10395–10406 (1991).

150. Palese, S., Schilling, L., Miller, R. J. D., Staver, P. R. & Lotshaw, W. T. Femtosecond Optical Kerr Effect Studies of Water. 6308–6316 (1994). doi:10.1021/j100076a013

151. Mcmorrow, D., Lotshaw, W. T. & Kenney-Wallace, G. A. Femtosecond Optical Kerr Studies on the Origin of the Nonlinear Responses in Simple Liquids. *IEEE J. Quantum Electron.* **24**, 443–454 (1988).

152. Mcmorrow, D. & Lotshaw, W. T. Intermolecular Dynamics in Acetonitrile Probed with Femtosecond Fourier Transform Raman Spectroscopy. *J. Phys.*

Chem. **95**, 10395–10406 (1991).

153. Righini, R. Ultrafast optical Kerr effect in liquids and solids. *Science (80-.).* **262**, 1386–1390 (1993).

154. Eesley, G. L. *Coherent Raman Spectroscopy*. (Pergamon Press, 1981).

155. Levenson, M. D. & Eesley, G. L. Applied Physics Polarization Selective Optical Heterodyne Detection for Dramatically Improved Sensitivity in Laser Spectroscopy *. *Appl. Phys.* **19**, 1–17 (1979).

156. De Silvestri, S., Cerullo, G. & Lanzani, G. *Coherent Vibrational Dynamics*. *Coherent Vibrational Dynamics* (CRC Press, 2008).

157. Mährlein, S. F. Nonlinear Terahertz Phononics: A Novel Route to Controlling Matter. *Nonlinear Terahertz Phononics: A Novel Route to Controlling Matter* (Freie Universität Berlin, 2016).

158. Shim, S.-H. & Zanni, M. T. How to turn your pump – probe instrument into a multidimensional spectrometer : 2D IR and Vis spectroscopies via pulse shaping. *Phys. Chem. Chem. Phys.* **11**, 748–761 (2009).

159. Albrecht, A. W., Hybl, J. D., Faeder, S. M. G. & Jonas, D. M. Experimental distinction between phase shifts and time delays : Implications for femtosecond spectroscopy and coherent control of chemical reactions. *J. Chem. Phys.* **111**, 10934 (1999).

160. Miyano, K., Tripathi, N., Yanagida, M. & Shirai, Y. Lead Halide Perovskite Photovoltaic as a Model p − i − n Diode. *Acc. Chem. Res.* **49**, 303–310 (2016).

161. Walsh, A., Scanlon, D. O., Chen, S., Gong, X. G. & Wei, S. H. Self-regulation mechanism for charged point defects in hybrid halide perovskites. *Angew. Chemie - Int. Ed.* **54**, 1791–1794 (2015).

162. Yin, W. J., Shi, T. & Yan, Y. Unusual defect physics in CH3NH3PbI3 perovskite solar cell absorber. *Appl. Phys. Lett.* (2014). doi:10.1063/1.4864778

163. Xing, G. *et al.* Long-range balanced electron- and hole-transport lengths in organic-inorganic CH3NH3PbI3. *Science* **342**, 344–347 (2013).

164. Herz, L. M. Charge-Carrier Dynamics in Organic-Inorganic Metal Halide Perovskites. *Annu. Rev. Phys. Chem.* **67**, 65–89 (2016).

165. Manser, J. S., Christians, J. A. & Kamat, P. V. Intriguing Optoelectronic Properties of Metal Halide Perovskites. *Chem. Rev.* **116**, 12956–13008 (2016).

166. Zhang, W., Eperon, G. E. & Snaith, H. J. Metal halide perovskites for energy applications. *Nat. Energy* **1**, (2016).

167. Filippetti, A. & Mattoni, A. Hybrid perovskites for photovoltaics: Insights from first principles. *Phys. Rev. B - Condens. Matter Mater. Phys.* **89**, 1–8 (2014).

168. Even, J., Carignano, M. & Katan, C. Molecular disorder and translation/rotation coupling in the plastic crystal phase of hybrid perovskites. *Nanoscale* **8**, 6222–6236 (2016).

169. Amat, A. *et al.* Cation-induced band-gap tuning in organohalide perovskites: Interplay of spin-orbit coupling and octahedra tilting. *Nano Lett.* **14**, 3608–3616 (2014).

170. Walsh, A. Principles of Chemical Bonding and Band Gap Engineering in Hybrid Organic-Inorganic Halide Perovskites. *J. Phys. Chem. C* **119**, 5755–5760 (2015).

171. Quarti, C. *et al.* The Raman Spectrum of the CH3NH3PbI3 Hybrid Perovskite: Interplay of Theory and Experiment. *J. Phys. Chem. Lett.* **5**, 279–284 (2014).

172. Kulbak, M., Cahen, D. & Hodes, G. How Important Is the Organic Part of Lead Halide Perovskite Photovoltaic Cells? Efficient CsPbBr3 Cells. *J. Phys. Chem. Lett.* **6**, 2452–2456 (2015).

173. Frolova, L. A. *et al.* Highly efficient all-inorganic planar heterojunction perovskite solar cells produced by thermal coevaporation of CsI and PbI2. *J. Phys. Chem. Lett.* **8**, 67–72 (2017).

174. Berdiyorov, G. R., Kachmar, A., El-Mellouhi, F., Carignano, M. A. & El-Amine Madjet, M. Role of Cations on the Electronic Transport and Optical Properties of Lead-Iodide Perovskites. *J. Phys. Chem. C* **120**, 16259–16270 (2016).

175. Polok, K., Ratajska-Gadomska, B., Konarska, J. & Gadomski, W. Coherent optical phonons in pure and Pr3+ doped YAG crystal studied by Optical Kerr Effect spectroscopy: Temperature and concentration dependence. *Chem. Phys.* **442**, 119–127 (2014).

176. Yaffe, O. *et al.* Local Polar Fluctuations in Lead Halide Perovskite Crystals. *Phys. Rev. Lett.* **118**, 136001 (2017).

177. Ivanovska, T. *et al.* Vibrational Response of Methylammonium Lead Iodide: From Cation Dynamics to Phonon–Phonon Interactions. *ChemSusChem* **9**, 2994–3004 (2016).

178. Loudon, R. Theory of the first-order Raman effect in crystals. *Proc. R. Soc. Lond.* **275**, 218–232 (1963).

179. Motta, C., El-Mellouhi, F. & Sanvito, S. Exploring the cation dynamics in lead-bromide hybrid perovskites. *Phys. Rev. B* **93**, 1–7 (2016).

180. Rakita, Y., Cohen, S. R., Kedem, N. K., Hodes, G. & Cahen, D. Mechanical Properties of APbX3 (A=Cs or CH3NH3; X=I or Br) Perovskite Single Crystals. *MRS Commun.* **5**, 623–629 (2015).

181. Bennett, B. R., Soref, R. A. & Del Alamo, J. A. Carrier-Induced Change in Refractive Index of InP, GaAs, and InGaAsP. *IEEE J. Quantum Electron.* **26**, 113–122 (1990).

182. Shah, J. *Ultrafast spectroscopy of semiconductors and semiconductor nanostructures*. **115**, (Springer Science & Business Media, 2013).

183. Perdew, J. P., Ernzerhof, M. & Burke, K. Rationale for mixing exact exchange with density functional approximations. *J. Chem. Phys.* **105**, 9982 (1996).

184. Cortecchia, D. *et al.* Broadband emission in two-dimensional hybrid perovskites: The role of structural deformation. *J. Am. Chem. Soc.* **139**, 39–42 (2017).

185. Akkerman, Q. A. *et al.* Solution Synthesis Approach to Colloidal Cesium Lead Halide Perovskite Nanoplatelets with Monolayer-Level Thickness Control. *J. Am. Chem. Soc.* **138**, 1010–1016 (2016).

186. Savenije, T. J. *et al.* Thermally activated exciton dissociation and recombination control the carrier dynamics in organometal halide perovskite. *J. Phys. Chem. Lett.* **5**, 2189–2194 (2014).

187. Ōsaka, Y. Polaron state at a finite temperature. *Prog. Theor. Phys.* **22**, 437–446 (1959).

188. Van Mechelen, J. L. M. *et al.* Electron-phonon interaction and charge carrier mass enhancement in SrTiO3. *Phys. Rev. Lett.* **100**, 226403 (2008).

189. Frost, J. M. Calculating polaron mobility in halide perovskites. *Phys. Rev. B* **96**, 195202 (2017).

190. Saidaminov, M. I. *et al.* High-quality bulk hybrid perovskite single crystals within minutes by inverse temperature crystallization. *Nat. Commun.* (2015). doi:10.1038/ncomms8586

191. Karakus, M. *et al.* Phonon-Electron Scattering Limits Free Charge Mobility in Methylammonium Lead Iodide Perovskites. *J. Phys. Chem. Lett.* (2015). doi:10.1021/acs.jpclett.5b02485

192. Bardeen, J. & Shockley, W. Deformation potentials and mobilities in non-polar crystals. *Phys. Rev.* **80**, 72–80 (1950).

193. He, Y. & Galli, G. Perovskites for solar thermoelectric applications: A first principle study of CH3NH3AI3 (A = Pb and Sn). *Chem. Mater.* (2014). doi:10.1021/cm5026766

194. Zhao, T., Shi, W., Xi, J., Wang, D. & Shuai, Z. Intrinsic and Extrinsic Charge Transport in CH3NH3PbI3 Perovskites Predicted from First-Principles. *Sci. Rep.* **7**, (2016).

195. Wang, Y., Zhang, Y., Zhang, P. & Zhang, W. High intrinsic carrier mobility and photon absorption in the perovskite CH3NH3PbI3. *Phys. Chem. Chem. Phys.* **17**, 11516–11520 (2015).

196. Mante, P.-A., Stoumpos, C. C., Kanatzidis, M. G. & Yartsev, A. Electron–acoustic phonon coupling in single crystal CH3NH3PbI3 perovskites revealed by coherent acoustic phonons. *Nat. Commun.* **8**, 14398 (2017).

197. McMeekin, D. P. *et al.* A mixed-cation lead mixed-halide perovskite absorber for tandem solar cells. *Science* **351**, 151–155 (2016).

198. Rakita, Y. *et al.* Low-Temperature Solution-Grown CsPbBr 3 Single Crystals and Their Characterization. *Cryst. Growth Des.* **16**, 5717–5725 (2016).

199. Hanusch, F. C. *et al.* Efficient planar heterojunction perovskite solar cells based on formamidiniumlead bromide. *J. Phys. Chem. Lett.* **5**, 2791–2795 (2014).

200. Rodová, M., Brožek, J., Knížek, K. & Nitsch, K. Phase transitions in ternary caesium lead bromide. *J. Therm. Anal. Calorim.* **71**, 667–673 (2003).

201. Perdew, J. P., Burke, K. & Ernzerhof, M. Generalized Gradient Approximation Made Simple. *Phys. Rev. Lett.* **77**, 3865–3868 (1996).

202. Giannozzi, P. *et al.* QUANTUM ESPRESSO: A modular and open-source

software project for quantum simulations of materials. *J. Phys. Condens. Matter* (2009). doi:10.1088/0953-8984/21/39/395502

203. Yang, Y. *et al.* Low surface recombination velocity in solution-grown CH3NH3PbBr3 perovskite single crystal. *Nat Commun* **6**, 7961 (2015).
204. Osaka, Y. Polaron State at a Finite Temperature. *Prog. Theor. Phys.* **22**, 437–446 (1959).
205. Scholtz, T. Polar Crystals: Self-Energy, Mass, and Mobility. *Phys. Rev.* **116**, 526 (1959).
206. Hellwarth, R. W. & Biaggio, I. Mobility of an electron in a multimode polar lattice. *Phys. Rev. B* **60**, 299 (1999).
207. Feynman, R. P., Hellwarth, R. W., Iddings, C. K. & Platzman, P. M. Mobility of slow electrons in a polar crystal. *Phys. Rev.* **127**, 1004–1017 (1962).
208. Zheng, F. & Wang, L. Large polaron formation and its effect on electron transport in hybrid perovskites. *Energy Environ. Sci.* **12**, 1219–1230 (2019).
209. Frost, J. M. *et al.* Atomistic Origins of High-Performance in Hybrid Halide Perovskite Solar Cells. *Nano Lett.* **14**, 2584–2590 (2014).
210. Liu, S. *et al.* Ferroelectric Domain Wall Induced Band-Gap Reduction and Charge Separation in Organometal Halide Perovskites. *J. Phys. Chem. Lett.* 150122172636002 (2015). doi:10.1021/jz502666j
211. Pecchia, A., Gentilini, D., Rossi, D., Auf der Maur, M. & Di Carlo, A. The Role of Ferroelectric Nanodomains in the Transport Properties of Perovskite Solar Cells. *Nano Lett.* **16**, 988–992 (2016).
212. Maehrlein, S. F., Joshi, P. P., Wang, F. & Zhu, X.-Y. Extreme Lattice Response to Ferroelectric Charge Localization in Lead Halide Perovskites. *Submitted* 1–12
213. Fritz, D. M. *et al.* Ultrafast bond softening in bismuth: mapping a solid's interatomic potential with X-rays. *Science (80-.).* **315**, 633–636 (2007).
214. Hase, M., Kitajima, M., Nakashima, S. & Mizoguchi, K. Dynamics of coherent anharmonic phonons in bismuth using high density photoexcitation. *Phys. Rev. Lett.* **88**, 67401 (2002).
215. Cheng, T. K. *et al.* Modulation of a semicondutor-to-semimetal transition at 7 THz via coherent lattice vibrations. *Appl. Phys. Lett.* **62**, 1901–1903 (1993).

216. Hunsche, S., Wienecke, K., Dekorsy, T. & Kurz, H. Impulsive softening of coherent phonons in tellurium. *Phys. Rev. Lett.* **75**, 1815 (1995).

217. Franssen, W. M. J., van Es, S. G. D., Dervisoglu, R., de Wijs, G. A. & Kentgens, A. P. M. Symmetry, Dynamics, and Defects in Methylammonium Lead Halide Perovskites. *J. Phys. Chem. Lett.* **8**, 61–66 (2017).

218. Fabini, D. H. *et al.* Universal Dynamics of Molecular Reorientation in Hybrid Lead Iodide Perovskites. *J. Am. Chem. Soc.* **139**, 16875–16884 (2017).

219. Guo, Y. *et al.* Interplay between organic cations and inorganic framework and incommensurability in hybrid lead-halide perovskite CH3NH3PbBr3. *Phys. Rev. Mater.* **1**, 1–6 (2017).

220. Guo, Y. *et al.* Dynamic emission Stokes shift and liquid-like dielectric solvation of band edge carriers in lead-halide perovskites. *Nat. Commun.* **10**, 1175 (2019).

221. Teitelbaum, S. W. *et al.* Direct Measurement of Anharmonic Decay Channels of a Coherent Phonon. *Phys. Rev. Lett.* **121**, 125901 (2018).

222. Subedi, A., Cavalleri, A. & Georges, A. Theory of nonlinear phononics for coherent light control of solids. *Phys. Rev. B* **89**, 1–5 (2014).

223. Juraschek, D. M. & Maehrlein, S. F. Sum-frequency ionic Raman scattering. *Phys. Rev. B* **97**, 1–8 (2018).

224. Schafer, R. W. & Rabiner, L. R. Design and Simulation of a Speech Analysis-Synthesis System Based on Short-Time Fourier Analysis. *IEEE Trans. Audio Electroacoust.* **AU-21**, 165–174 (1973).

225. Sejdic, E., Djurovic, I. & Jiang, J. Time – frequency feature representation using energy concentration : An overview of recent advances. *Digit. Signal Process.* **19**, 153–183 (2009).

226. Först, M. *et al.* Nonlinear phononics as an ultrafast route to lattice control. *Nat. Phys.* **7**, 854–856 (2011).

227. Juraschek, D. M., Fechner, M. & Spaldin, N. A. Ultrafast Structure Switching through Nonlinear Phononics. *Phys. Rev. Lett.* **118**, 1–5 (2017).

228. Bischak, C. G. *et al.* Tunable Polaron Distortions Control the Extent of Halide Demixing in Lead Halide Perovskites. *J. Phys. Chem. Lett.* **9**, 3998–4005 (2018).

229. Stroppa, A., Quarti, C., De Angelis, F. & Picozzi, S. Ferroelectric Polarization of CH3NH3PbI3: A Detailed Study Based on Density Functional Theory and Symmetry Mode Analysis. *J. Phys. Chem. Lett.* 2223–2231 (2015). doi:10.1021/acs.jpclett.5b00542

230. Wu, B. *et al.* Indirect tail states formation by thermal-induced polar fluctuations in halide perovskites. *Nat. Commun.* **10**, 484 (2019).

231. Dong, H., Lewis, N. H. C., Oliver, T. A. A. & Fleming, G. R. Determining the static electronic and vibrational energy correlations via two-dimensional electronic-vibrational spectroscopy. *J. Chem. Phys.* **142**, 174201 (2015).

232. Cheng, Y.-H., Gao, F. Y., Teitelbaum, S. W. & Nelson, K. A. Coherent control of optical phonons in bismuth. *Phys. Rev. B* **96**, 134302 (2017).

233. Cho, G. C., Kütt, W. & Kurz, H. Subpicosecond time-resolved coherent-phonon oscillations in GaAs. *Phys. Rev. Lett.* **65**, 764 (1990).

234. Zeiger, H. J. *et al.* Theory for displacive excitation of coherent phonons. *Phys. Rev. B* **45**, 768 (1992).

235. Lanzani, G., Cerullo, G. & De Silvestri, S. *Coherent Vibrational Dynamics*. (CRC Press, 2007).

236. Wright, A. D. *et al.* Electron–phonon coupling in hybrid lead halide perovskites. *Nat. Commun.* **7**, 11755 (2016).

237. Iaru, C. M., Geuchies, J. J., Koenraad, P. M., Vanmaekelbergh, D. & Silov, A. Y. Strong carrier–phonon coupling in lead halide perovskite nanocrystals. *ACS Nano* **11**, 11024–11030 (2017).

238. Kang, J. & Wang, L.-W. High defect tolerance in lead halide perovskite CsPbBr3. *J. Phys. Chem. Lett.* **8**, 489–493 (2017).

239. Ambrosio, F., Wiktor, J., De Angelis, F. & Pasquarello, A. Origin of low electron–hole recombination rate in metal halide perovskites. *Energy Environ. Sci.* **11**, 101–105 (2018).

240. Hsu, H.-C. *et al.* Photodriven Dipole Reordering: Key to Carrier Separation in Metalorganic Halide Perovskites. *ACS Nano* (2019). doi:10.1021/acsnano.8b09645

241. Wu, X. *et al.* Trap States in Lead Iodide Perovskites. *J. Am. Chem. Soc.* 150202132606001 (2015). doi:10.1021/ja512833n

242. Thouin, F. *et al.* Amendments Author Correction : Phonon coherences reveal the polaronic character of excitons in two-dimensional lead halide perovskites. *Nat. Mater.* **18**, 41563 (2019).

243. Blinc, R. & Zeks, B. *Soft modes in ferroelectrics and antiferroelectrics*. (North-Holland, 1974).

244. Merlin, R. Generating coherent THz phonons with light pulses. *Solid State Commun.* **102**, 207–220 (1997).

245. Schlipf, M., Poncé, S. & Giustino, F. Carrier Lifetimes and Polaronic Mass Enhancement in the Hybrid Halide Perovskite CH3NH3PbI3 from Multiphonon Fröhlich Coupling. *Phys. Rev. Lett.* **121**, 86402 (2018).

246. Sluka, T., Tagantsev, A. K., Bednyakov, P. & Setter, N. Free-electron gas at charged domain walls in insulating BaTiO3. *Nat. Commun.* **4**, 1808 (2013).

247. Schröder, M. *et al.* Conducting domain walls in lithium niobate single crystals. *Adv. Funct. Mater.* **22**, 3936–3944 (2012).

248. Venkataraman, G. Soft modes and structural phase transitions. *Bull. Mater. Sci.* **1**, 129–170 (1979).

249. Hsu, H. C. *et al.* Photodriven Dipole Reordering: Key to Carrier Separation in Metalorganic Halide Perovskites. *ACS Nano* **13**, 4402–4409 (2019).

250. Kohmoto, T., Tada, K., Moriyasu, T. & Fukuda, Y. Observation of coherent phonons in strontium titanate: Structural phase transition and ultrafast dynamics of the soft modes. *Phys. Rev. B - Condens. Matter Mater. Phys.* **74**, 2–6 (2006).

251. Conte, G., Somma, F. & Nikl, M. Nanocrystalline CsPbBr3 thin films: a grain boundary opto-electronic study. *Phys. Status Solidi* **2**, 306–309 (2005).

252. DeQuillettes, D. W. *et al.* Impact of microstructure on local carrier lifetime in perovskite solar cells. **348**, 683–686 (2015).

253. Grancini, G. *et al.* Role of microstructure in the electron–hole interaction of hybrid lead halide perovskites. *Nat. Photonics* (2015). doi:10.1038/nphoton.2015.151

Appendix: Single Crystal Synthesis and Characterization

The morphology of lead halide perovskites contribute significantly to their apparent optoelectronic properties[251–253]. Because of this behavior, LHP single crystals are the most suitable samples for studying their intrinsic properties. The synthesis of LHP single crystals is accomplished by vapor diffusion. The synthesis method for $CH_3NH_3PbBr_3$ described here is based on the method developed by Shi and coworkers.[14] The synthesis procedure for $CsPbBr_3$ is based on that of Rakita and coworkers[198].

For $CH_3NH_3PbBr_3$, a saturated solution (1 M) of precursors, $PbBr_2$ and CH_3NH_3Br, is prepared in *N,N*-dimethylformamide (DMF). The precursor solution is placed in an open container, which is subsequently placed in a larger closed container. The outer container is filled with an antisolvent in which the precursors are insoluble, typically isopropanol (IPA) or dichloromethane (DCM). The vapor pressure of the antisolvent must exceed that of the solvent. The antisolvent slowly diffuses into the solvent, reducing the solubility of the precursor solution and initiating crystallization. The diffusion rate can be controlled by the vapor pressure of the antisolvent or by the size of the opening in the inner container.[14]

The synthesis procedure of $CsPbBr_3$ has an extra titration step. A saturated solution (0.45 M) of $PbBr_2$ and CsBr is prepared in dimethyl sulfoxide (DMSO) at 50° C. Because CsBr is relatively insoluble in DMSO compared to $PbBr_2$, other products can form during vapor diffusion, particularly Cs_4PbBr_6. In order to isolate the correct compound, the precursor solution is titrated with methanol (MeOH)

until the orange-yellow precipitate no longer redissolves. The solution is sealed and stirred at 50° C for 24 hours, until the precipitate has turned yellow-green. This precipitate is Cs_4PbBr_6. The supernatant is removed and filtered and placed in an open inner container. MeOH is used as the antisolvent in the outer container. For thin, crack-free, optically-flat single crystals (**Figure 0.1**A and C), the crystallization is stopped within 48 hours. The single crystals are characterized by single crystal x-ray diffraction (SCXRD), as shown in **Figure 0.1**B and D. Data was collected on an Agilent SuperNova single crystal X-ray diffractometer at room temperature. The lattice constants for cubic $MAPbBr_3$ and orthorhombic $CsPbBr_3$ are given in **Table 0.1**

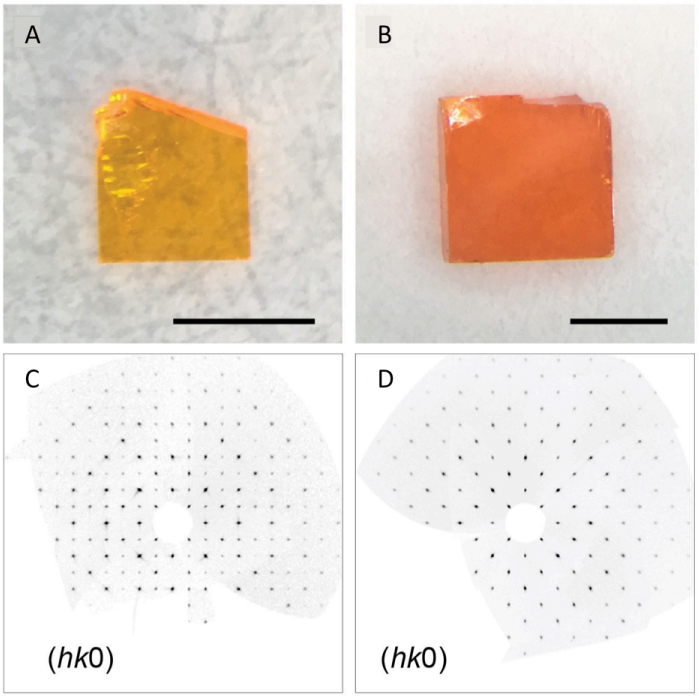

Figure 0.1 Optical Images and Diffraction of $CsPbBr_3$ and $MAPbBr_3$. A, C Optical image and SCXRD of $CsPbBr_3$ and, **B**, **D**, of $MAPbBr_3$.

Table 0.1. Lattice constants for cubic $MAPbBr_3$ (space group $Pm\bar{3}m$) and orthorhombic $CsPbBr_3$ (space group Pbnm).

	a	b	c
$MAPbBr_3$	5.924 Å		
$CsPbBr_3$	8.223 Å	8.243 Å	11.761 Å